

AD-A243 756



AFIT/GE/ENG/91D-10

DTIC
S
C

RADAR SCATTERING FROM FOAMED
PLASTIC TARGET SUPPORTS

THESIS

Michael W. Chambers, Captain, USAF

AFIT/GE/ENG/91D-10

Approved for Public release: distribution unlimited

91-19002



91 12 24 016

| REPORT DOCUMENTATION PAGE | | | Form Approved OMB No. 0704-0188 | |
|---|---|---|--------------------------------------|--|
| <small>Public reporting burden for this collection of information is estimated to average 1 hour per response, including the time for reviewing instructions, searching existing data sources, gathering and maintaining the data needed, and completing and reviewing the collection of information. Send comments regarding this burden estimate or any other aspect of this collection of information, including suggestions for reducing this burden, to Washington Headquarters Services, Directorate for Information Operations and Reports, 1215 Jefferson Davis Highway, Suite 1204 Arlington, VA 22202-4302 and to the Office of Management and Budget, Paperwork Reduction Project (0704-0188), Washington, DC 20503.</small> | | | | |
| 1. AGENCY USE ONLY (Leave blank) | 2. REPORT DATE December 1991 | 3. REPORT TYPE AND DATES COVERED Master's Thesis | | |
| 4. TITLE AND SUBTITLE RADAR SCATTERING FROM FOAMED PLASTIC TARGET SUPPORTS | | 5. FUNDING NUMBERS | | |
| 6. AUTHOR(S) Michael W. Chambers, Captain, USAF | | | | |
| 7. PERFORMING ORGANIZATION NAME(S) AND ADDRESS(ES) Air Force Institute of Technology, WPAFB OH 45433-6583 | | 8. PERFORMING ORGANIZATION REPORT NUMBER AFIT/GE/ENG/91D-10 | | |
| 9. SPONSORING / MONITORING AGENCY NAME(S) AND ADDRESS(ES) 6585 Test Group, RATSCAT, Holloman AFB, NM | | 10. SPONSORING / MONITORING AGENCY REPORT NUMBER | | |
| 11. SUPPLEMENTARY NOTES | | | | |
| 12a. DISTRIBUTION / AVAILABILITY STATEMENT Approved for public release; distribution unlimited | | | 12b. DISTRIBUTION CODE | |
| 13. ABSTRACT (Maximum 200 words) This study investigates the scattering from foamed plastic target supports. This material is often used in both indoor and outdoor ranges to support all sizes of targets for radar cross section (RCS) measurements. Two common foamed plastics, styrofoam and expanded bead polystyrene (EPS), are discussed. Two types of scattering are associated with foamed plastic, coherent and incoherent. The incoherent is normally the lowest, but has not been satisfactorily quantified. Coherent scattering is related to the shape of the target, and the emphasis of this study is on the coherent return. One goal was to predict the coherent RCS of an EPS column using the Uniform Theory of Diffraction (UTD). It was found that UTD can accurately predict the backscatter of an EPS column consisting of flat and curved surfaces. The second goal was to experimentally study the effects of shaping on coherent RCS. The benefits of adding a vertical slope to circular cylindrical columns was studied. RCS reductions of approximately 20 dB were achieved. Some low RCS column shapes were also measured; sloping did not produce a measurable RCS reduction in these cases. | | | | |
| 14. SUBJECT TERMS Radar, Radar Cross Section, Electromagnetic Scattering, Measurements, Plastics | | | 15. NUMBER OF PAGES 128 | |
| | | | 16. PRICE CODE | |
| 17. SECURITY CLASSIFICATION OF REPORT Unclassified | 18. SECURITY CLASSIFICATION OF THIS PAGE Unclassified | 19. SECURITY CLASSIFICATION OF ABSTRACT Unclassified | 20. LIMITATION OF ABSTRACT UL | |

RADAR SCATTERING FROM FOAMED
PLASTIC TARGET SUPPORTS

THESIS

Presented to the Faculty of the School of Engineering
of the Air Force Institute of Technology

Air University

In Partial Fulfillment of the
Requirement for the Degree of
Master of Science in Electrical Engineering

Michael W. Chambers, B.S.
Captain, USAF

December 1991

Approved for Public release: distribution unlimited

| | |
|--------------------|-------------------------------------|
| Accession For | |
| DTIC Serial | <input checked="" type="checkbox"/> |
| DTIC Tab | <input type="checkbox"/> |
| Unannounced | <input type="checkbox"/> |
| Justification | |
| By | |
| Distribution | |
| Availability Codes | |
| Dist | Special |
| A-1 | |

Acknowledgements

I would like to express my thanks to Captain Phil Joseph for his help and guidance throughout this thesis project, from start-up to completion. His open door policy kept me going during several rough times when things weren't coming together as I thought they should.

I also appreciate the help of other AFIT staff, including Captain Welsh and Dr. Pyati who served on my thesis committee. Captain Mullinix and Mr. Lindsay from the RCS Chamber provided expertise during numerous RCS measurements.

I offer my most sincere gratitude to my wife, JoAnn, who encouraged me throughout this entire effort. Her support reminded me of the importance of reaching one's goals, even when they seem out of reach. Also, a special thanks to my son Timothy, who made even the stressful days seem a little more fun.

Table of Contents

| | |
|--|------|
| Acknowledgements | ii |
| List of Figures | v |
| List of Tables | vii |
| Abstract | viii |
| I. Introduction | 1.1 |
| Background | 1.1 |
| Foamed Plastics | 1.3 |
| Problem Statement | 1.4 |
| Sequence of Presentation | 1.4 |
| II. Scattering From Foamed Plastic | 2.1 |
| Introduction | 2.1 |
| Literature Review | 2.1 |
| Incoherent Scattering | 2.7 |
| Coherent Scattering | 2.10 |
| III. Diffraction Analysis of Coherent Scattering | 3.1 |
| Introduction | 3.1 |
| Uniform Theory of Diffraction | 3.1 |
| UTD for a Dielectric Strip | 3.8 |
| Fresnel Reflection and Transmission Coefficients | 3.9 |
| Radar Cross Section | 3.11 |
| RCS of Partial Cylinder | 3.12 |
| IV. Experimental Study of Column Design | 4.1 |
| Introduction | 4.1 |
| Measurement Set-Up | 4.1 |
| Low RCS Support Columns | 4.3 |
| Full Azimuth Scans | 4.4 |
| Front Sector Azimuth Scans | 4.14 |
| Incoherent Scattering | 4.29 |
| Prediction Model | 4.30 |
| V. Conclusions and Recommendations | 5.1 |
| Summary | 5.1 |
| Conclusions | 5.2 |
| Recommendations | 5.3 |

| | |
|--|--------|
| Appendix A: Fortran Prediction Code | A.1 |
| Appendix B: Noise Floor Measurements of the AFIT RCS Chamber . . . | B.1 |
| Appendix C: RCS Measurements of the Sloped Cylinders | C.1 |
| Appendix D: RCS Measurements of the Shaped Columns | D.1 |
| Appendix E: RCS Measurements of the Sloped Diamond | E.1 |
| Appendix F: Impulse Response Plots of the Partial Cylinder | F.1 |
| Bibliography | Bibl.1 |

List of Figures

| | | |
|--------------|--|------|
| Figure 2.1. | Physical Model of Styrofoam Structure | 2.1 |
| Figure 2.2. | Shaped Blocks used by Knott and Senior | 2.5 |
| Figure 2.3. | Measured and Calculated RCS for Truncated Cones | 2.8 |
| Figure 2.4. | RCS versus Frequency of a 12" EPS Cube | 2.11 |
| Figure 2.5. | Reflections from the Front and Rear of a Cube | 2.12 |
| Figure 2.6. | Time Domain Plot of EPS Cube, Normal Incidence | 2.13 |
| Figure 3.1. | GO Fields Near the Edge of a Semi-Infinite Half Plane | 3.2 |
| Figure 3.2. | Diffractions from the Edge of a Semi-Infinite Half Plane | 3.2 |
| Figure 3.3. | UTD Variable Definitions | 3.3 |
| Figure 3.4. | GO Fields Near a Curved (Concave and Convex) Surface Edge | 3.6 |
| Figure 3.5. | GO Fields from a Dielectric Half Plane | 3.8 |
| Figure 3.6. | Reflection and Transmission from a Dielectric Interface | 3.9 |
| Figure 3.7. | Target Support Column used for Prediction Model. | 3.12 |
| Figure 3.8. | Physical Dimensions of the Target | 3.13 |
| Figure 3.9. | Regions Surrounding the Partial Cylinder | 3.14 |
| Figure 3.10. | Shadow Boundaries Formed by Corner 1 | 3.16 |
| Figure 3.11. | Example of Shadow Boundaries for Region 1 | 3.18 |
| Figure 3.12. | Shadow Boundaries for Region 2 | 3.20 |
| Figure 3.13. | Shadow Boundaries for Region 4 | 3.22 |
| Figure 3.14. | Curved Face RSB and Reflection in Region 6 | 3.23 |
| Figure 3.15. | Measured Versus Theoretical RCS of the Partial Cylinder, Vertical Polarization, F=10 Ghz. | 3.25 |
| Figure 3.16. | Measured Versus Theoretical RCS of the Partial Cylinder, Horizontal Polarization, F=10 GHz. | 3.26 |
| Figure 3.17. | Measured Versus Theoretical RCS of the Half Cylinder, Vertical Polarization, F=10 GHz | 3.27 |
| Figure 3.18. | Measured Versus Theoretical RCS of the Half Cylinder, Horizontal Polarization, F=10 GHz. | 3.28 |
| Figure 4.1. | RCS Measurement Hardware | 4.2 |
| Figure 4.2. | Cylindrical Columns | 4.5 |
| Figure 4.3. | Azimuth Scan of Right Circular Cylinder, Vertical Polarization, F = 7 GHz. | 4.6 |
| Figure 4.4. | Impulse Response and Frequency Response for RCC, V-Pol | 4.7 |
| Figure 4.5. | Azimuth Scan of 10 Degree Sloped Cylinder, Vertical Polarization, F = 7 Ghz. | 4.8 |
| Figure 4.6. | Noise Floor Measurement | 4.9 |
| Figure 4.7. | Frequency/Impulse Response of the 10 Degree Cylinder, Vertical Polarization. | 4.10 |
| Figure 4.8. | Frequency/Impulse Response of the 20 Degree Cylinder, Vertical Polarization. | 4.12 |
| Figure 4.9. | Frequency/Impulse Response of the 30 Degree Cylinder, Vertical Polarization. | 4.13 |

| | | |
|--------------|--|------|
| Figure 4.10. | Top View of the Three Shaped Columns | 4.14 |
| Figure 4.11. | Azimuth Scan of Wedge-Ogive, Taken Different Days, Horizontal Polarization, F = 10 GHz. | 4.16 |
| Figure 4.12. | Azimuth Scan of Ogive, Taken Different Days, Horizontal Polarization, F = 10 GHz. | 4.18 |
| Figure 4.13. | Azimuth Scan of Diamond, Horizontal Pol, F=10 GHz. | 4.19 |
| Figure 4.14. | Frequency/Impulse Response of the Wedge-Ogive, Tip-On, Horizontal Polarization. | 4.21 |
| Figure 4.15. | Frequency/Impulse Response of Wedge-Ogive, 45° off Tip, Horizontal Polarization | 4.22 |
| Figure 4.16. | Frequency/Impulse Response of the Ogive, Tip-On, Horizontal Polarization. | 4.23 |
| Figure 4.17. | Frequency/Impulse Response of the Ogive, 45° off Tip, Horizontal Polarization | 4.24 |
| Figure 4.18. | Frequency/Impulse Response of the Diamond, Tip-On, Horizontal Polarization. | 4.25 |
| Figure 4.19. | Frequency/Impulse Response of the Diamond, 45° off Tip, Horizontal Polarization | 4.26 |
| Figure 4.20. | Frequency Response of the 20 Degree Sloped Cylinder, Horizontal Polarization. | 4.27 |
| Figure 4.21. | Azimuth Scan of Sloped Diamond, V-Pol, F=10 GHz. | 4.28 |
| Figure 4.22. | Frequency Response of the Sloped Diamond, H-Pol. | 4.29 |
| Figure 4.23. | Impulse Response of the Partial Cylinder, H-Pol. | 4.31 |
| Figure B.1. | Noise Floor Measurement, Azimuth Scan | B.2 |
| Figure B.2. | Noise Floor Measurement, Azimuth Scan | B.3 |
| Figure B.3. | Noise Floor Measurement, Frequency Scan | B.4 |
| Figure C.1. | Azimuth Scan of the 20° and 30° Sloped Cylinders. | C.2 |
| Figure C.2. | Azimuth Scans of the RCC and the 10° Sloped Cylinder. | C.3 |
| Figure C.3. | Azimuth Scans of the 20° and 30° Sloped Cylinders | C.4 |
| Figure C.4. | Frequency/Time Domain Plot of the RCC | C.5 |
| Figure C.5. | Frequency/Time Domain Plot of the 10° Sloped Cylinder | C.6 |
| Figure C.6. | Frequency/Time Domain Plot of the 20° Sloped Cylinder | C.7 |
| Figure C.7. | Frequency/Time Domain Plot of the 30° Sloped Cylinder | C.8 |
| Figure D.1. | Azimuth Scans of the Diamond | D.2 |
| Figure D.2. | Azimuth Scans of the Wedge-Ogive. | D.3 |
| Figure D.3. | Azimuth Scans of the Ogive | D.4 |
| Figure E.1. | Comparison of Diamond and Sloped Diamond at F=10 GHz. | E.2 |
| Figure E.2. | Comparison of Tip-On Frequency Response | E.3 |
| Figure E.3. | Impulse Response of the Diamond at 0° and 15° | E.4 |
| Figure F.1. | Impulse Response at $\theta = 0^\circ$ and $\theta = 5^\circ$ | F.2 |
| Figure F.2. | Impulse Response at $\theta = 15^\circ$ and $\theta = 35^\circ$ | F.3 |
| Figure F.3. | Impulse Response at $\theta = 55^\circ$ and $\theta = 60^\circ$ | F.4 |
| Figure F.4. | Impulse Response at $\theta = 70^\circ$ and $\theta = 90^\circ$ | F.5 |
| Figure F.5. | Impulse Response at $\theta = 120^\circ$ and $\theta = 135^\circ$ | F.6 |
| Figure F.6. | Impulse Response at $\theta = 165^\circ$ and $\theta = 180^\circ$ | F.7 |

List of Tables

| | |
|---|------|
| Table 2.1. Average RCS of the Six Foam Ogives | 2.6 |
| Table 3.1. Regions of Interest | 3.15 |

Abstract

This study investigates the scattering from foamed plastic target supports. This material is often used in both indoor and outdoor ranges to support all sizes of targets for radar cross section (RCS) measurements. Two common foamed plastics, styrofoam and expanded bead polystyrene (EPS), are discussed. These materials have very low reflection coefficients; thus, the scattered energy from supports constructed of foamed plastics is minimal.

Two types of scattering are associated with foamed plastic, coherent and incoherent, and both are discussed. The incoherent is normally the lowest, but has not been satisfactorily quantified. Coherent scattering is related to the shape of the target, and the emphasis of this study is on the coherent return.

One goal of this study was to predict the coherent RCS of an EPS column using the Uniform Theory of Diffraction (UTD). It was found that UTD can accurately predict the backscatter of an EPS column consisting of flat and curved surfaces.

The second goal of this study was to experimentally study the effects of shaping on coherent RCS. The benefits of adding a vertical slope to circular cylindrical columns was studied. RCS reductions of approximately 20 dB were achieved. Some low RCS column shapes were also measured; sloping did not produce a measurable RCS reduction in these cases.

RADAR SCATTERING FROM FOAMED PLASTIC TARGET SUPPORTS

I. Introduction

Background

One important parameter of a modern military aircraft is its radar cross section (RCS). RCS is a measure of the radar power scattered in a given direction, normalized with respect to the power density of the incident field [1:47]. The RCS of small targets, including scale model aircraft, can be measured in anechoic chambers designed for this purpose. One example of such a facility is the Air Force Institute of Technology (AFIT) RCS Measurement Chamber. Not all targets can be measured in the laboratory environment. The Radar Target Scattering Facility (RATSCAT), part of the 6585th Test Group, Holloman AFB, New Mexico has been tasked with the responsibility of measuring the RCS of several classes of targets, including full scale aircraft.

A radar cross section measurement may be made by placing the target upon a target support, which in turn may rest on a turntable. This is commonly done at RATSCAT. A radar transmitter of known frequency illuminates the target. The target support should place the target in the center of the transmitter's beamwidth. A receiver is used to measure the amount of electromagnetic energy scattered from the target in a given direction. The primary consideration when choosing the target support is that the scattered energy from it must be significantly lower than that of the target. Normally, the transmit and receive antennas are collocated, in which case the radar cross section measurement is known as monostatic. The RCS of the target is calculated

by comparing the received amplitude and phase to the received signal of a calibrated reference target, usually a conducting sphere.

Since the target support structure also scatters the incident radar energy, it is one of the largest measurement errors. As mentioned, the target supports are designed to scatter as little energy as possible in the direction of the receiver. When the target's RCS is large, the error introduced by the support is usually minimal. However, in the case where the target has a low RCS, the target support could possibly produce a radar return stronger than that of the target.

The RCS of the target support column is reduced by shaping and by use of low reflective materials. For example, the AFIT RCS Chamber uses a metal column in the shape of a tilted ogive, a very low RCS shape, as a target support pedestal. The target is typically rested atop a much smaller column, which is mounted into the top of the pedestal. These smaller supports are most often constructed from foamed plastics, such as styrofoam or beaded polystyrene. This type of material has very low reflectivity and allows most of the incident radar energy to pass through the support without scattering. The RCS of these columns is typically several orders of magnitude below that of a conducting target.

At an outdoor range, the support structure may need to handle targets from several hundred pounds to over fifty tons for a full scale aircraft. It is still desirable to use material such as foamed plastics for these heavy targets. However, the structure needed to support a heavy target must be physically large. As the size of the target support increases, its RCS also tends to increase. Consequently, a poorly designed support column may be insufficient. The scattering from the supports must be accounted for before making an RCS measurement.

Various types of expanded or foamed plastics have been used in the construction of target support columns. The engineers at RATSCAT now use particular material known as expanded polystyrene (EPS). EPS is manufactured from polystyrene particles which are expanded into small spheres, called beads. The manufacturing process tightly packs the beads together to form a block of EPS [3]. EPS is relatively easy to shape by cutting the block with a heated wire.

EPS weighs from one to two pounds per cubic foot. The relative dielectric constant of the actual polystyrene making up the beads is 2.55. After the beads are expanded, the average dielectric constant of the material as a whole is less than 1.05, with the actual value depending on the density [3]. Since the dielectric constant of air is 1.00 the calculated reflection coefficient from EPS is very low, on the order of .005 for normal incidence. Most of the radar's energy which strikes the polystyrene passes through it. Very little energy is actually scattered back to the radar.

The scattering from foamed plastics falls into two categories, coherent and incoherent. Coherent scattering comes from the overall shape of the targets. Incoherent scattering is due to the nature of the material, consisting of tightly packed individual scatterers. Since the total number of individual particles in a target is related to its volume, incoherent scattering is also referred to as volume scattering.

Foamed Plastics

This thesis concentrates on target supports constructed of the various types of foamed plastics. Commonly used foamed plastics are styrofoam, expanded bead polystyrene, beadboard and Ecofoam. Since

most of this work discusses styrofoam and a particular expanded bead polystyrene called EPS, a brief description of each is presented.

Styrofoam is a registered trade name of the Dow Chemical Company [2] for a particular blue foamed plastic. It is manufactured by dissolving polystyrene in a solvent and the resulting gel is subjected to pressure and heat. When released from the pressure, bubbles of air are formed in the gel, which is then molded and dried [3]. Although Dow produced the first Styrofoam, many companies now produce very similar materials. The term styrofoam is now accepted as a generic name for any of these similar products, and will be used as such in this thesis.

Expanded bead polystyrene is manufactured by expanding pinhole sized beads of polystyrene through application of heat. After cooling, the beads are steamed in a pressurized mold to bind them together, and then dried at room temperature [3]. The experimental portion of this project examines targets made of EPS, which is the material used by RATSCAT.

Problem Statement

The goal of this thesis is twofold. The first goal is to develop an RCS prediction model for the coherent scattering from two dimensional beaded polystyrene target supports. The second is to experimentally investigate improved designs for EPS target supports.

Sequence of Presentation

Section II of this thesis is a review of the literature and a discussion of coherent and incoherent scattering. Section III develops the RCS prediction model. This section includes a review of the Uniform Theory of Diffraction (UTD), followed by an explanation of how the basic

UTD theory is modified to account for a dielectric target. Then the equations used to model an EPS target support are derived. Finally, a comparison of predictions versus measurements is given to assess the accuracy of the prediction model.

Section IV presents the experimental portion of the thesis. This section describes the equipment used, some of the experimental limitations, and a description of the targets measured. A summary of the results concludes this section.

Finally, Section V offers conclusions and recommendations found in the process of this thesis.

II. Scattering From Foamed Plastics

Introduction

This section discusses the two types of scattering associated with foamed plastics, coherent and incoherent. It starts with a review of the pertinent literature, then a discussion of each scattering type.

Literature Review

Scattering From Plastic Foams In [2] and [3], Plonus describes a means to calculate the electromagnetic scattering from styrofoam. Styrofoam is made of small air pockets surrounded by polystyrene. He models the cells or particles of the foam as "an aggregate of spherical shells (ping-pong balls)" [2:20] as shown in figure 2.1.

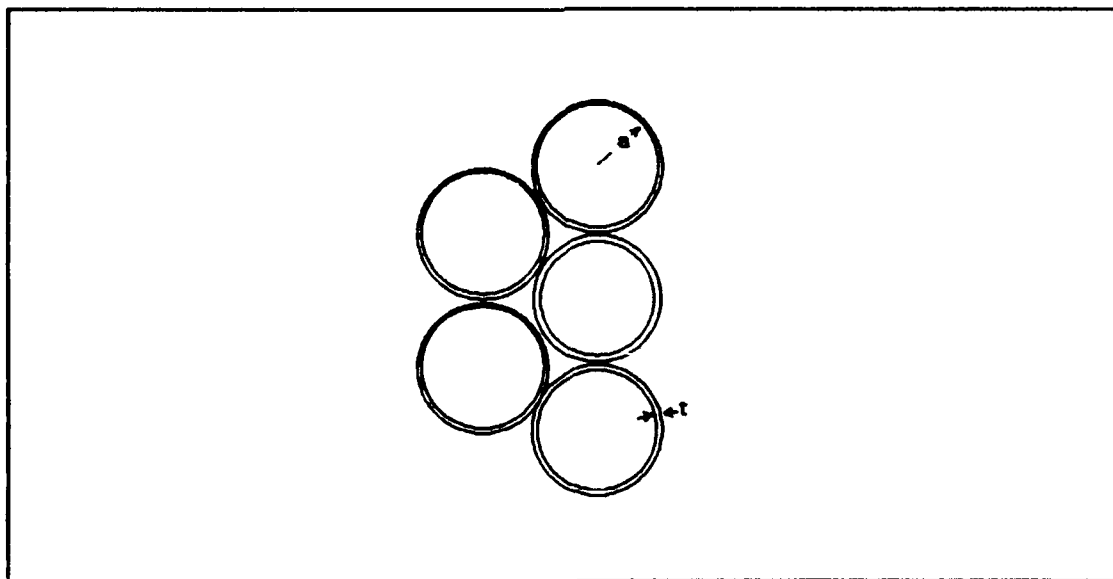


Figure 2.1. Physical Model of Styrofoam Structure [2]

Each of the cells scatters the incident energy. Plonus was the first to note that styrofoam and other polystyrene materials have two scattering mechanisms:

The total back scatter from an aggregate of N particles will in general be composed of a coherent and an incoherent contribution. Coherent scattering results when a systematic relation between the phases of the scatterers exists, or when the particle density changes within a distance of a wavelength. This type of scattering is proportional to N^2 since amplitudes rather than intensities (power) add. Incoherent scattering is the usual contribution from an aggregate of randomly distributed particles which act independently of each other, implying that no systematic relation between the phases of the scatterer exists; hence it is proportional to N . This type of scattering will then be strictly a consequence of the random arrangements of the particles. This is due either to the random motion or fluctuation in time about some average distribution when the aggregate is illuminated with a steady signal, or to the random fluctuations about some average when many samples of a material consisting of a random distribution of particles are examined. [3:89]

Plonus states that these two averages, the time average and ensemble average, will usually give identical results in steady-state scattering problems. He chooses to consider the time average; that is, he assumes the distribution function of particles per unit length to depend on position and time (rather than position and ensemble member). This distribution function is denoted by $n(r,t)$. The time averaged RCS of a distribution of scatterers described by $n(r,t)$ is given by [4:700] as

$$\sigma = \sigma_1 \int_0^{\infty} \int_0^{\infty} \overline{n(r,t) n(r',t)} e^{-2ik(r-r')} dr dr' \quad (2.1)$$

where σ_1 is the RCS of one scatterer.

Performing the time average and simplifying, Plonus finds the total RCS to be

$$\sigma = \sigma_1 \left| \int_0^{\infty} \bar{n}(r) e^{-2ikr} dr \right|^2 + \sigma_1 \int_0^{\infty} \bar{n}(r) dr \quad (2.2)$$

where $\bar{n}(r)$ is the time average of the distribution function (which represents the time average particle density at location r), and k is the wave number.

The first term in Eq. (2.2) is the coherent RCS. If $\bar{n}(r)$ varies slowly relative to the oscillatory exponential term, the result will average to zero. Thus, coherent scattering arises from "some inhomogeneity in the distribution, some deviations from uniformity" [2:8]. Within styrofoam targets, changes in density of the material are small, so that $\bar{n}(r)$ is nearly constant and the coherent scattering remains small. The most significant inhomogeneity is the boundary of the air and the styrofoam, that is, the surface of the target. Here the density $\bar{n}(r)$ jumps from zero to its normal value, making the integral non-zero. Therefore the largest contribution to coherent scattering for styrofoam targets is the surface of the target.

The second term in Eq. (2.2), which can be written as $N\sigma_1$ (where N is the total number of particles), is the incoherent RCS. In general, this second integral is not reducible to zero. Incoherent scattering represents the sum of the scattering from each of the cells within the structure. The total number of scatterers is directly related to the volume of the target, hence the term volume scattering is often used in place of incoherent scattering.

Recall that coherent scattering is proportional to N^2 , while incoherent scattering is proportional to N . Thus, according to Plonus, "Coherent scattering will usually be the dominant part of a radar echo

when a particle system scatters both coherently and incoherently" [2:9]. However, the coherent return can be reduced by shaping the target so that the scattered energy is directed away from the receiver. The incoherent is not reducible for a given polystyrene material, thus it can be thought of as a minimum return from a target. Plonus derives an equation for the incoherent scattering from styrofoam. Assuming the spherical shells are touching,

$$\sigma_{ic} = \frac{\pi}{2} V k^4 t^2 a (\epsilon_p - 1)^2 \quad (m^2) \quad (2.3)$$

where σ_{ic} is the RCS due to incoherent scattering, t is the thickness of the cell wall, a is the cell radius, and ϵ_p is the relative permittivity of polystyrene (2.55). For a commonly used styrofoam, $a = .05$ cm and $t = .0092a$. Replacing these in Eq. (2.3) gives

$$\sigma_{ic} = 6.225 \times 10^{-11} \frac{V}{\lambda^4} \quad (m^2) \quad (2.4)$$

The cell radius greatly affects the RCS, so materials with smaller cells lead to lower incoherent scattering. However, materials with smaller cells can support less weight, so a compromise must be made by the column designer.

Support Structures

In [5], Knott and Senior reported on the use of polystyrenes for target support structures. They performed measurements on six types of foams. To further examine the coherent versus incoherent scattering, they measured various shaped blocks (high coherent return) and ogives (low coherent return). They assumed that by lowering the coherent

return through shaping, the measurements would show only the incoherent return.

Starting with a flat metal plate, they found that tilting the plate at 23 degrees led to the lowest RCS. They shaped blocks of various polystyrenes so that the surfaces facing and opposite to the receiver had the 23 degree slope, as seen in figure 2.2. They

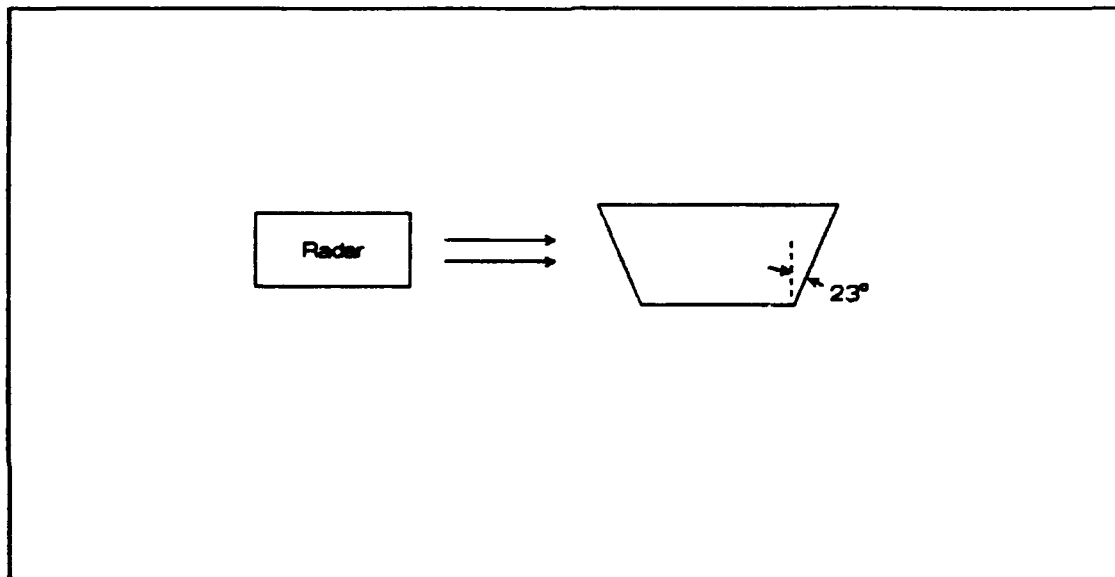


Figure 2.2. Shaped Blocks Used by Knott and Senior

measured two blocks at various frequencies between 8.7 and 9.9 Ghz. Their results are presented in units of $10 \log (\sigma^2)$ and range from -70 to -85 dB referenced to meter⁴. They say "Certainly the source(s) of the return cannot be identified with certainty and though it was originally hoped that the incoherent contributions would be dominant, it is apparent that this is not true for blocks of the shape used here."

They then measured ogives made of each of the six types of materials at the same frequencies noted above. Each ogive was about 18.75 inches long and 3.625 inches in diameter. The volume ranged

between 100 and 107 cubic inches. The RCS data does not show a λ^{-4} dependence as predicted for incoherent scattering. The 15 measured values for each ogive were averaged and are presented in Table 2.1.

Table 2.1. Average RCS of the Six Foam Ogives

| Material | RCS (dBsm) |
|--------------|------------|
| Tyrlfoam | -58.7 |
| Pelaspam | -70.2 |
| Styrofoam FB | -68.9 |
| Styrofoam DB | -69.6 |
| Styrofoam FR | -72.3 |
| Thurane | -72.4 |

They conclude that the RCS measured is not the incoherent return, but a mixture of coherent return and surface wave effects. The data presented can only be said to be an upper bound on the incoherent scattering.

The above results were combined with a determination of the weight bearing capacity of the different foams. A recommendation was made to use expanded bead polystyrenes, such as Pelaspam for best overall performance. The EPS used by RATSCAT is an expanded bead polystyrene.

Designing Foamed Plastic Target Supports

In [6], Senior, Plonus, and Knott describe several factors which should be considered in designing target support structures. This work continues that done in [5]. They note that the predicted incoherent return differs from measured values. They discuss the fact that

Pelaspaspan is made from expanded beads of polystyrene, and the equations using the spherical shell model do not apply. However, they do not derive the equations associated with spherical particles.

They discuss a progression used to reduce the RCS of a foamed plastic right circular cylinder. The first step is to tilt the cylinder, thus reducing reflections, then to slope the entire cylinder, then add serrations to the outer surface of the sloped cylinder.

Truncated Cones

In [7], Plonus, Knott, and Kuo determined that a support structure shaped as a truncated cone was superior, in terms of low RCS, than a right cylindrical column. The authors "suggest that it is better to use a fat tapered column than a slender cylindrical one", and that the RCS is improved by up to 20 dB. Using equations from Plonus [2] to model the scattering from the surface, they derive an expression for the coherent RCS from a polystyrene truncated cone. Figure 2.3 shows the results of the predictions versus experimental data for several truncated cones. In one experiment, the slope was very slight, and the calculations were within 2 dB of the measured values. They claim that for the larger slopes, the poor match is most likely due to the noise floor of the equipment.

Incoherent Scattering

Incoherent Model for EPS As noted in the literature review, a model for incoherent scattering for styrofoam is $\sigma_{ic} = 6.225 \times 10^{-11} \lambda^{-4} \text{ (m}^2\text{)}$. This equation is often used to estimate the level of the incoherent scattering. However, this model assumes that the styrofoam

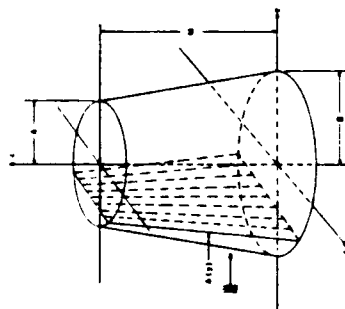


Fig. 1. Geometry of the truncated cone.

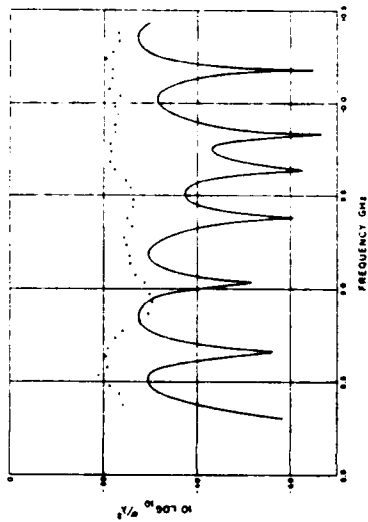


Fig. 3. Theoretical and experimental backscattering from a truncated cone ($d = 15.32$ cm, $B = 24.53$ cm, $M = 40.00$ cm).

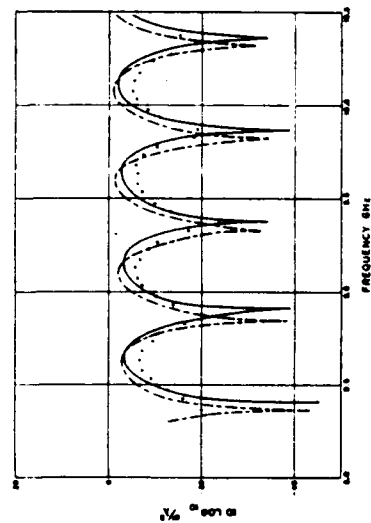


Fig. 2. Theoretical and experimental backscattering from a truncated cone ($d = 15.16$ cm, $B = 15.32$ cm, $M = 19.85$ cm). Theoretical backscattering from a cylinder ($d = B = 15.32$ cm, $M = 19.85$ cm).

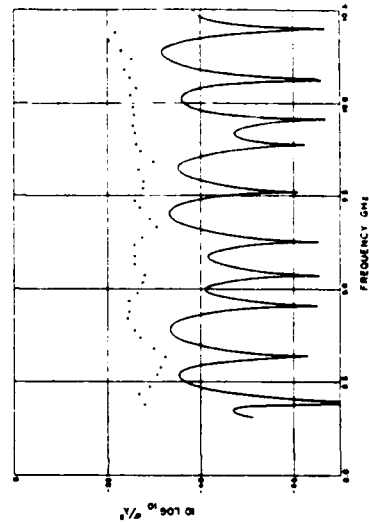


Fig. 4. Theoretical and experimental backscattering from a truncated cone ($d = 15.32$ cm, $B = 14.92$ cm, $M = 19.85$ cm).

Figure 2.3. Measured and Calculated RCS for Truncated Cones [7]

consists of tightly packed spherical shells whose scattering is independent of each other [2].

EPS more closely resembles tightly packed spheres. A more realistic model for EPS can be derived, starting with Eq. (2.2).

$$\sigma_{ic} = \sigma_i \int_0^{\infty} \bar{n}(r) dr = \sigma_i N \quad (2.2)$$

The scattering from the individual spheres can be represented using a Rayleigh equation, as found in [2],

$$\sigma_i = 4\pi a^2 (ka)^4 \left| \frac{\epsilon_r - 1}{\epsilon_r - 2} \right|^2 \quad (2.5)$$

where a is the sphere radius and ϵ_r is the average relative permittivity of the material.

Assuming the spheres are tightly packed, then

$$N = \frac{V}{(2a)^3} \quad (2.6)$$

For one pound per cubic foot density EPS, $\epsilon_r = 1.021$. The RCS due to the incoherent scattering is

$$\sigma_{ic} = \sigma_i N = .118 \frac{a^3}{\lambda^4} V \quad (2.7)$$

The measured bead radius for this density is approximately 2 millimeters. For this value,

$$\sigma_{ic} = 9.44 \times 10^{-10} \frac{V}{\lambda^4} \quad (2.8)$$

which is about 15 times (12 dB) higher than Plonus's estimates for styrofoam.

The inherent problem with both of these models is that they assume that each particle scatters independently of all others. No equations have been published that account for the interactions among particles that must surely exist.

Measured Data Figure 2.4 shows the results of a frequency scan measurement taken at the AFIT RCS Chamber of a one cubic foot cube, of one pound density EPS. From Eq. (2.8), the incoherent return is expected to be -54 dBsm at 6 GHz, -45 dBsm at 10 GHz, and -37 dBsm at 15 GHz. The measurement was made with one corner of the cube facing the antennas, to decrease the large coherent scattering from the faces of the cube. Note that the levels of the return are far below the predictions.

The measurement of the cube typifies the results found when looking for incoherent scattering, both as part of this work and the previous studies. The incoherent scattering is seldom seen at the levels expected. This will be further noted in the experimental section as measurements on low coherent scattering shapes are discussed. The incoherent scattering should determine a minimum return from a polystyrene target, but this was not noticed in any of the experimental data.

Coherent Scattering

In [2], Plonus used Physical Optics (PO) to determine the coherent RCS of styrofoam targets. He scaled the PO scattered field solution for a perfectly conducting target by the normal incidence reflection coefficient of the styrofoam to obtain the scattered field of the styrofoam target.

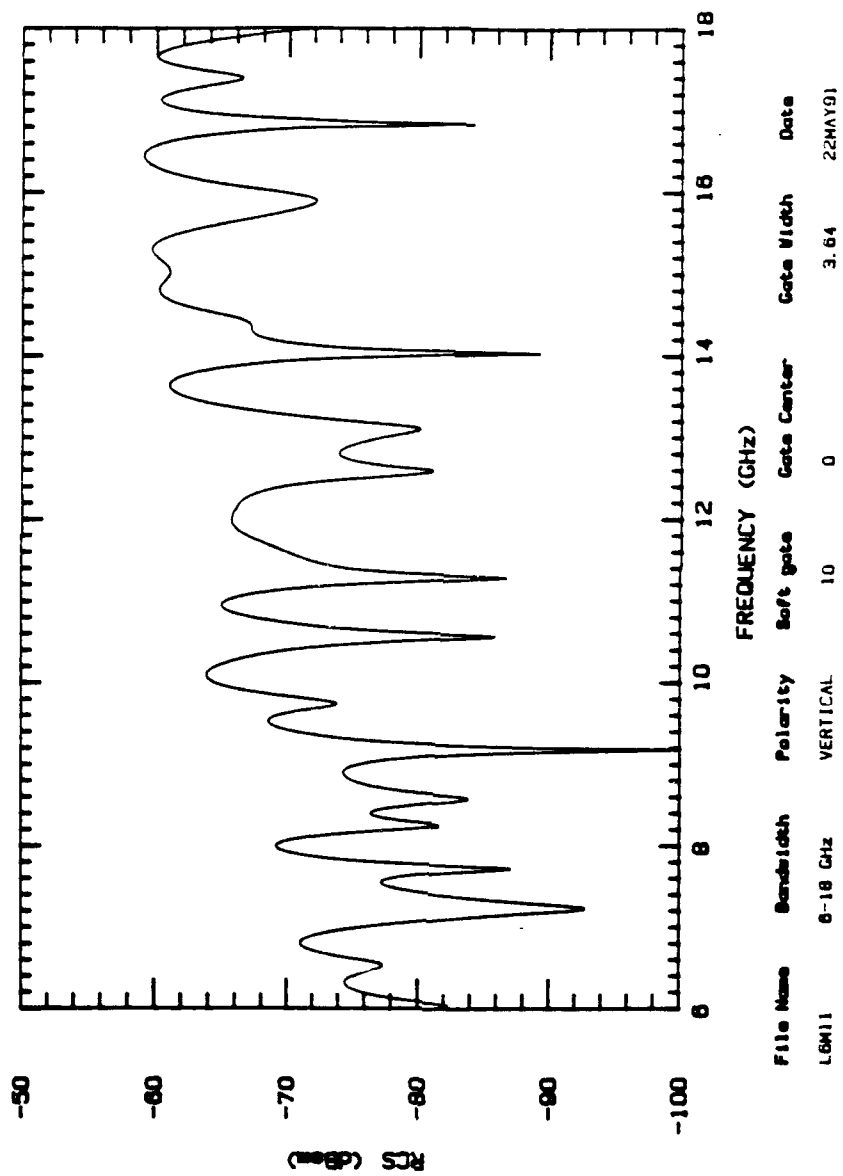


Figure 2.4. RCS Versus Frequency of a 12" EPS Cube

An important additional consideration when calculating the coherent scattering is that radar energy penetrates the target. As an example, consider the EPS cube as shown in figure 2.5.

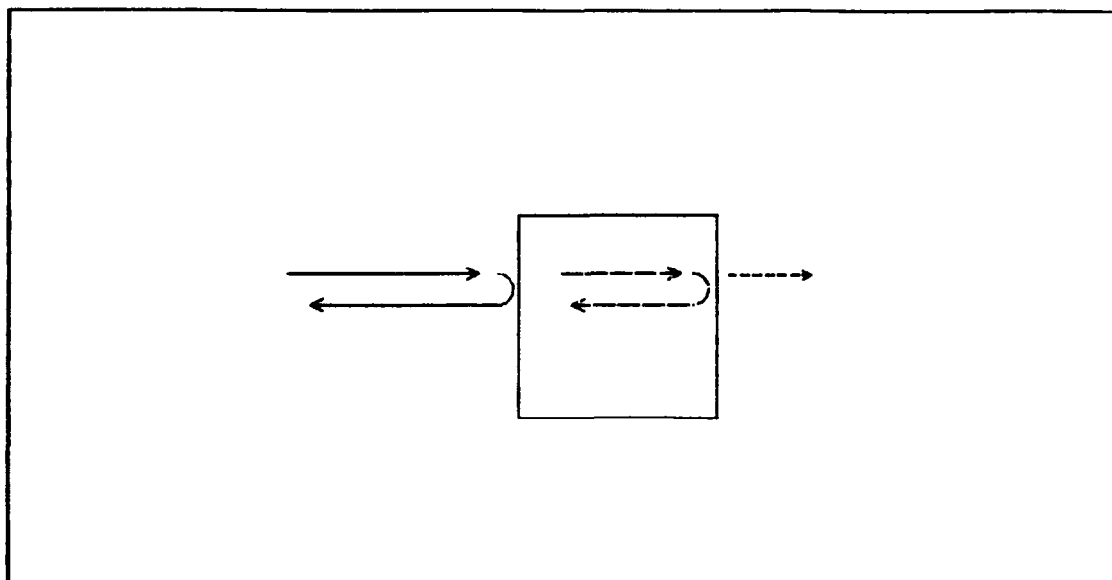


Figure 2.5. Reflections From the Front and Rear of a Cube

The radar receives a return not only from the front face of the cube, but also one that is nearly as strong from the rear face. A typical reflection coefficient for EPS is about .005, so that each reflection contains .005 times the amplitude of the incident field. In Figure 2.5, the ray that exits the rear of the cube contains about 99% of the incident field strength. This factor is why polystyrene supports are so often used; very little energy is scattered from the support.

Figure 2.6 shows another measurement made of the EPS cube. This measurement is a time-domain plot of the cube, viewed at normal incidence to a face. Note the large reflections that occur from the front and rear faces, and the absence of any return (incoherent) between the faces.

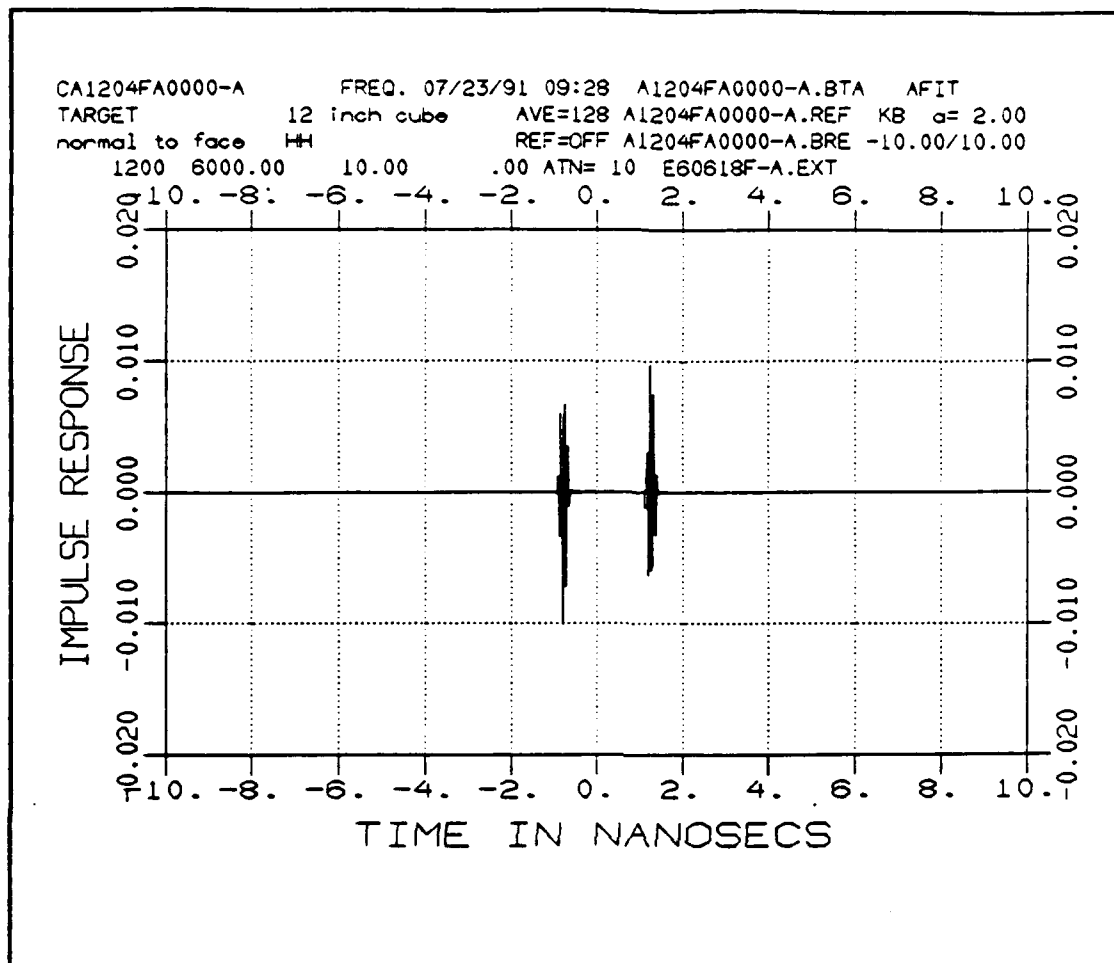


Figure 2.6. Time Domain Plot of EPS Cube, Normal Incidence

Coherent Return Reduction The fact that the front and rear returns from the cube are equal suggests a way to reduce the coherent return. A frequency can be chosen so that the two reflections add destructively, that is, the two reflected signals are 180 degrees out of phase and cancel each other. This method has been proven, however the cancellation works well only when the frequency is tightly controlled.

A simpler approach to lowering the coherent return is by shaping. Polystyrene target shaping uses the same principles as any other low observable target. An obvious technique is to eliminate or redirect

reflections from large flat surfaces, such as the face of the cube, as suggested by Knott and Senior [5]. By sloping the front and rear faces of their blocks (Figure 2.2) they drastically reduced the RCS.

Another possible shaping technique is the rounding of corners and edges. The success of this method depends on the observation angle. This subject will be discussed further in Section IV.

Finally, the coherent RCS can be reduced by proper choice of the material used. The relative permittivity of a material determines its reflection coefficient. Two pound density EPS has smaller beads than one pound density, meaning that each bead contains a higher concentration of polystyrene. This in turn means that the permittivity is higher and so the reflection coefficient is higher. Therefore, a cube made of two pound EPS has a larger RCS than a same-size cube of one pound EPS.

III. Diffraction Analysis of Coherent Scattering

Introduction

This section develops an RCS prediction for a two dimensional foamed plastic column. Three main topics will be discussed. The first is a review of the theory used in the development of the RCS prediction model. The second topic is the actual development of the model, and the third is a summary of results. The review covers the Uniform Theory of Diffraction (UTD) for conductors and dielectrics, and Fresnel reflection and transmission coefficients. The model development details the ray mechanisms considered for a specific column. Finally, predicted RCS is compared to measurements of actual targets.

Uniform Theory of Diffraction

One of the simpler methods for examining the scattered field from the edge of a conducting strip is Geometrical Optics (GO). At typical radar frequencies, GO fails because it does not account for diffraction from the edge. Figure 3.1 shows the Geometrical Optics (GO) fields. The source is assumed to be in the far-field so that all incoming rays are parallel. The set of rays associated with the incident field and the set of rays associated with the field reflected from the strip are the GO fields. As shown, the edge creates two boundaries, the reflection shadow boundary (RSB) and the incident shadow boundary (ISB). These shadow boundaries mark a physical discontinuity in the field strength of the GO fields. Thus, GO predicts discontinuous fields at the shadow boundaries and also a complete shadow (zero fields) below the conductor.

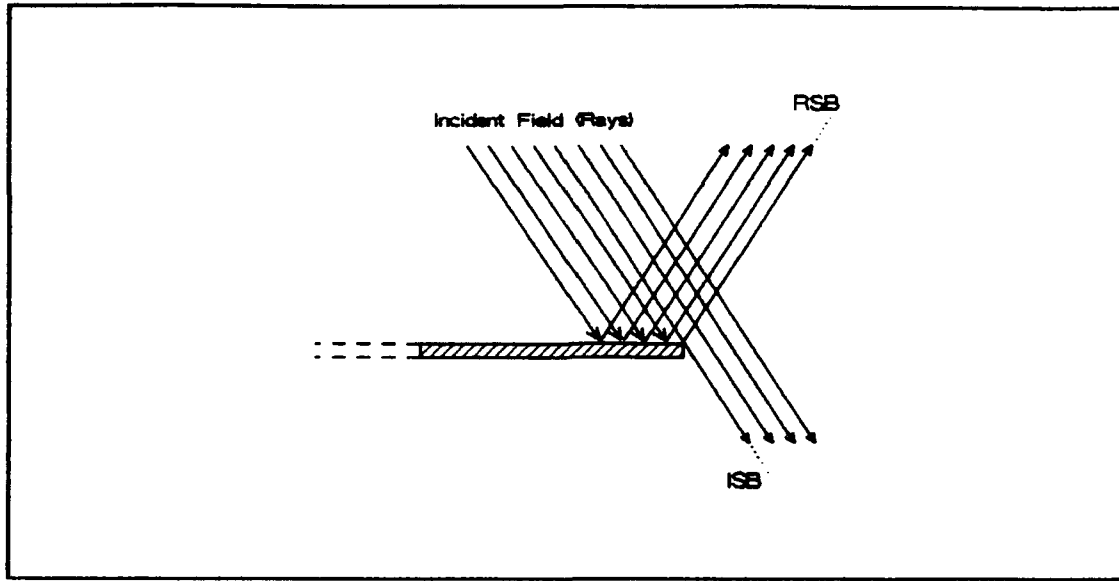


Figure 3.1. GO Fields Near the Edge of a Semi-Infinite Half Plane

To amend these shortcomings, Keller devised a theory, called the Geometrical Theory of Diffraction (GTD) [8], to predict the diffractions from the edge of a conducting half-plane, as shown is Figure 3.2.

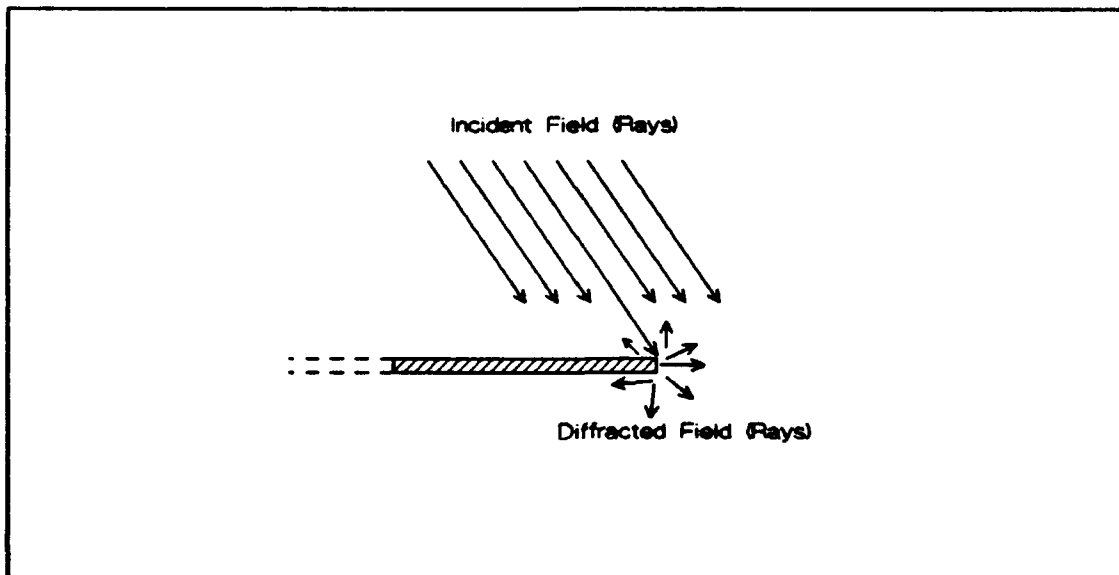


Figure 3.2. Diffractions from the Edge of a Semi-Infinite Half Plane

The total field at an arbitrary observer location is the sum of the GO and GTD fields. GTD was an improvement over GO, however, GTD predictions fail when the observer is near a GO shadow boundary (the solution becomes unbounded).

In [9], Kouyoumjian and Pathak developed a rigorous high frequency solution for edge diffraction, known as the Uniform Theory of Diffraction (UTD). Their diffracted field term yields a total field that is continuous at the shadow boundaries and non-zero below the conductor.

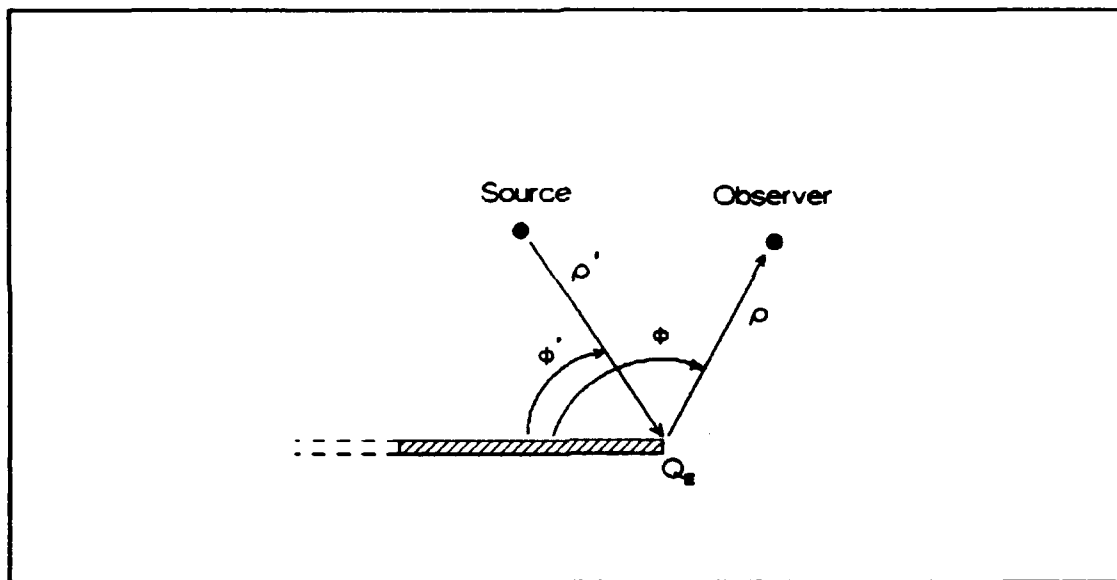


Figure 3.3. UTD Variable Definitions

Figure 3.3 displays some of the variables needed to define the diffracted field of the UTD. The edge is assumed to be part of a two dimensional semi-infinite half plane. The observer is located at polar coordinates (ϕ, ρ) while the source is located at (ϕ', ρ') . For the special case of backscatter, the source and observer are in the same location.

According to the UTD, the diffracted field from the edge of a conducting half plane is [9:1456]

$$U^d = U^i(Q_E) D_{s,h} \frac{\exp(-jk\rho)}{\sqrt{\rho}} \quad (3.1)$$

where U represents an electric (magnetic) field for the case of an electric (magnetic) line source. $U^i(Q_E)$ is the incident field at the edge, k is the free space wavenumber, and $D_{s,h}$ is the diffraction coefficient. The subscripts s and h on the diffraction coefficient correspond to the cases of the electric and magnetic line sources, respectively (these are the soft or hard boundary conditions) [10:9]. The diffraction coefficient is given in [9] as

$$D_{s,h} = \frac{-\exp(-j\frac{\pi}{4})}{2\sqrt{2\pi k}} \cdot \left[\frac{F(kLa(\phi-\phi'))}{\cos\left(\frac{\phi-\phi'}{2}\right)} \mp \frac{F(kLa(\phi+\phi'))}{\cos\left(\frac{\phi+\phi'}{2}\right)} \right] \quad (3.2)$$

where the (-) term is associated with soft polarization and the (+) term is used for hard polarization. In the diffraction coefficient,

$$L = \frac{\rho\rho'}{\rho+\rho'} \quad (3.3)$$

$$a(x) = 2\cos^2\left(\frac{x}{2}\right) \quad (3.4)$$

$$F(x) = 2j\sqrt{x} \exp(jx) \int_{\sqrt{x}}^{\infty} \exp(-jt^2) dt \quad (3.5)$$

The transition function $F(x)$ is a fresnel integral which approaches zero at the shadow boundaries, thus keeping the diffraction coefficient finite at these angles.

The uniform theory of diffraction is used to obtain the scattered field from a conducting edge. The actual surface of the conductor need not actually be a semi-infinite plane, as long as the frequency of the incident field is large enough that the surface is electrically large. As an example, UTD is often used to calculate the scattered field from a flat plate. In this case, the total diffracted field is the complex sum of the two edge diffractions.

Note that in Eq. (3.2), the diffraction coefficient is the sum of two components. The first term, the function of $(\phi - \phi')$, is related to the incident shadow boundary. The second term, the function of $(\phi + \phi')$, is related to the reflection shadow boundary. To ease the notation, the diffraction coefficient will be abbreviated as

$$D_{\theta, h} = D_I + D_R \quad (3.6)$$

where

$$D_I = \frac{-\exp(-j\frac{\pi}{4})}{2\sqrt{2\pi k}} \cdot \frac{F(kLa(\phi - \phi'))}{\cos\left(\frac{\phi - \phi'}{2}\right)} \quad (3.7)$$

and

$$D_R = \frac{-\exp(-j\frac{\pi}{4})}{2\sqrt{2\pi k}} \cdot \frac{F(kLa(\phi + \phi'))}{\cos\left(\frac{\phi + \phi'}{2}\right)} \quad (3.8)$$

UTD for Curved Surface Edges UTD can also be used to calculate the diffracted field from the edge of a conducting curved surface. The reflected rays are no longer parallel as in the case of a flat surface. However, the shadow boundaries are still formed as seen in Figure 3.4.

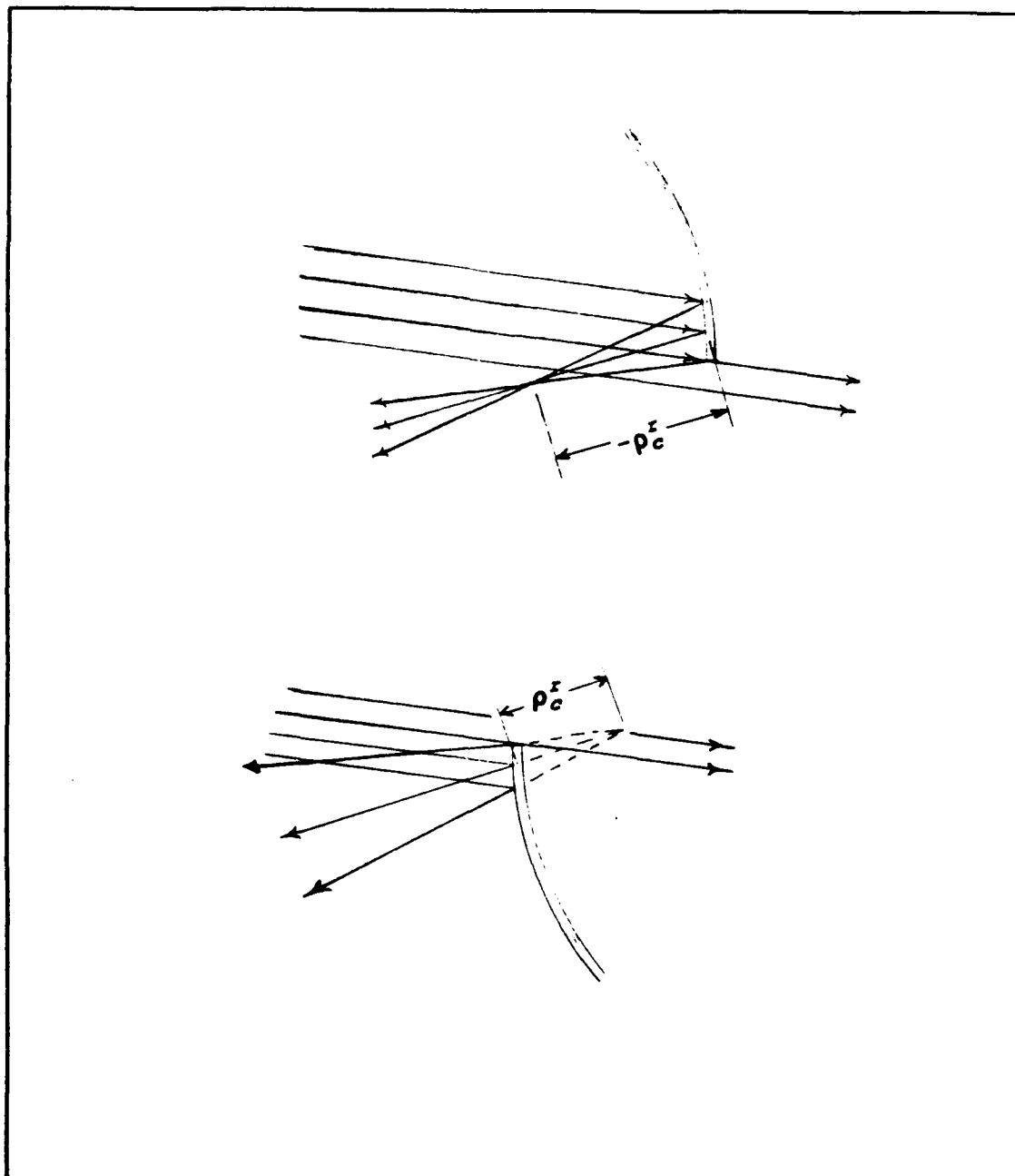


Figure 3.4. GO Fields Near a Curved (Concave and Convex) Surface Edge

The equation for the diffraction coefficient from a curved surface is nearly identical to Eq. (3.6), the difference being that the distance parameter L in D_R must be replaced by L^R , which is given by

$$L^R = \frac{\rho \rho_c^r}{\rho + \rho_c^r} \quad (3.9)$$

where ρ_c^r is the reflected field caustic distance. Note that ρ_c^r is negative for reflection from a concave surface and positive for a convex surface (as in Figure 3.4) [9:1457]. For far field calculations $\rho \rightarrow \infty$, therefore $L^R \rightarrow \rho_c^r$. For a surface with a constant radius of curvature, the caustic distance is simply one-half the radius of curvature of the edge. For example, if the radius of curvature is a constant 'a', then $L^R = \rho_c^r = \pm a/2$.

Reflection from a Curved Surface Other mechanisms that must be considered are the reflections themselves that arise from curved surfaces. Reflections from both concave and convex surfaces were shown in Figure 3.4.

If the source is located in the far zone, the reflected field at a distance ρ from the point can be represented by [9:1450]

$$U_{s,h}^r = \mp U^i(Q_R) \sqrt{\left| \frac{\rho_c}{\rho + \rho_c} \right|} \exp(j s \frac{\pi}{2} - j k \rho) \quad (3.10)$$

where $U^i(Q_R)$ is the incident field at the point of reflection (Q_R), and s is the number of caustics the rays pass through.

UTD for a Dielectric Strip

If the half-plane under consideration is made of a dielectric rather than a conductor, the UTD equations can be heuristically

modified. Each of the two terms in the diffraction coefficient must now be scaled by the amount of the discontinuity present along each shadow boundary. This method was first used by Burnside and Burgener [11] for a dielectric half-plane. As seen in Figure 3.5, the amount of the discontinuity along the reflection shadow boundary is Γ , the total reflection coefficient of the air-dielectric interface.

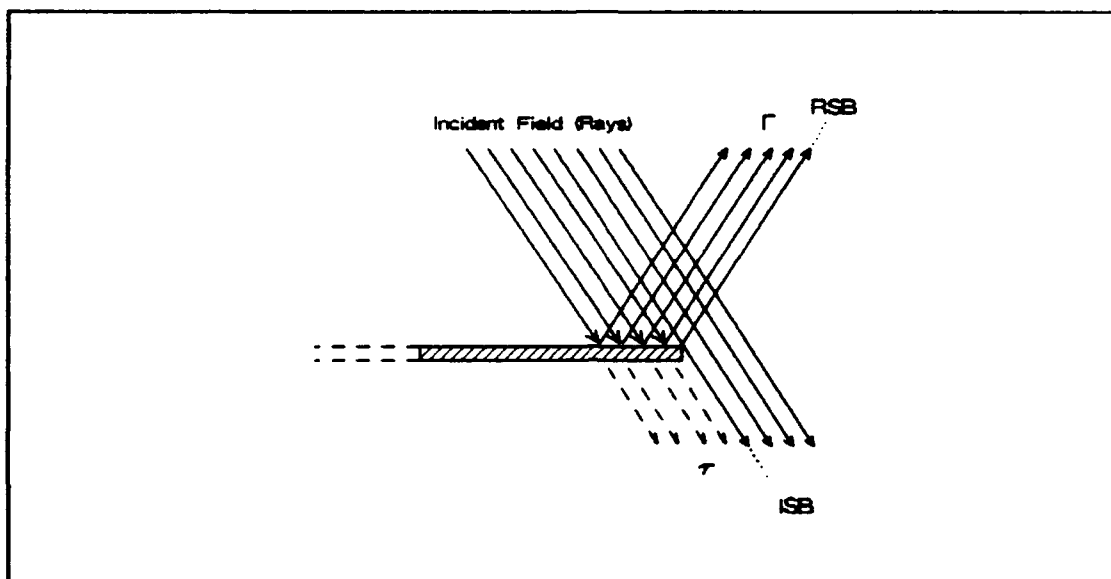


Figure 3.5. GO Fields from a Dielectric Half-Plane

The discontinuity along the incident shadow boundary is $(1-\tau)$, where τ is the total transmission coefficient of the interface (assuming the field strength of U^i is 1). With this approach, the diffraction coefficient for a dielectric material is

$$D_{s,h} = (1-\tau) D_I + \Gamma D_R \quad (3.11)$$

Note that the case of a conducting strip is actually a special case of the above formula, where Γ equals either ± 1 , depending on the polarization, and τ equals 0.

Reflection from Dielectric Curved Surfaces The field reflected from a dielectric curved surface is the same as in Eq. (3.10) with the exception that the right side of the equation is scaled by the appropriate reflection coefficient Γ .

Fresnel Reflection and Transmission Coefficients

When a plane wave strikes a dielectric/dielectric interface, a certain amount of the field is transmitted into the media while another portion is reflected away. Electromagnetic boundary conditions must be satisfied to determine the reflection and transmission coefficients for each polarization.

Figure 3.6 shows the two polarizations as described by Weeks [12:234-235], where the s and h subscripts in the following equations refer to soft and hard polarizations, respectively.

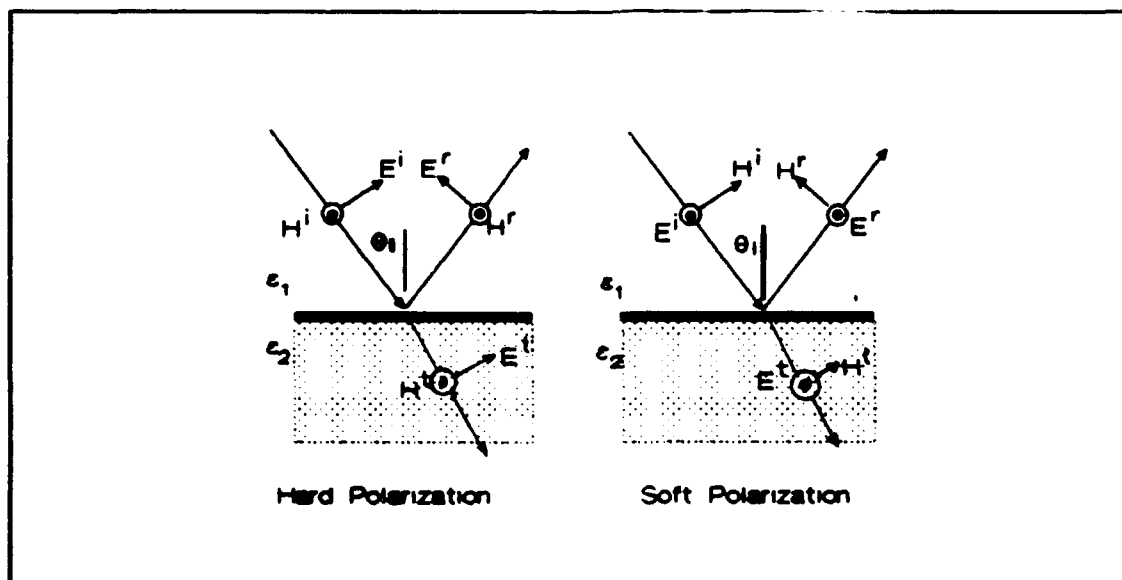


Figure 3.7. Reflection and Transmission from a Dielectric Interface

The coefficients for soft polarization are

$$\Gamma_s = \frac{|\bar{E}^r|}{|\bar{E}^i|} = \frac{\cos\theta_i - \sqrt{\frac{\epsilon_2}{\epsilon_1} - \sin^2\theta_i}}{\cos\theta_i + \sqrt{\frac{\epsilon_2}{\epsilon_1} - \sin^2\theta_i}} \quad (3.12)$$

$$\tau_s = \frac{|\bar{E}^t|}{|\bar{E}^i|} = 1 + \Gamma_s \quad (3.13)$$

which assumes that neither material is magnetic (the relative permeability of both materials equals one).

For the case of hard polarization

$$\Gamma_h = \frac{|\bar{H}^r|}{|\bar{H}^i|} = \frac{\frac{\epsilon_2}{\epsilon_1} \cos\theta_i - \sqrt{\frac{\epsilon_2}{\epsilon_1} - \sin^2\theta_i}}{\frac{\epsilon_2}{\epsilon_1} \cos\theta_i + \sqrt{\frac{\epsilon_2}{\epsilon_1} - \sin^2\theta_i}} \quad (3.14)$$

$$\tau_h = \frac{|\bar{H}^t|}{|\bar{H}^i|} = 1 + \Gamma_h \quad (3.15)$$

Radar Cross Section

The term radar cross section is an indicator of the amount of backscattered energy from a target relative to the incident energy. It is defined as [13:578]

$$\sigma = \lim_{R \rightarrow \infty} 4\pi R^2 \left| \frac{U^{scat}}{U^{inc}} \right|^2 \quad (3.16)$$

where the units of σ are in square meters.

As mentioned, UTD is a means of determining the diffracted field from a two-dimensional surface. For two dimensional targets, the backscatter is characterized by its echo length, symbolized as σ_{2D} , defined by

$$\sigma_{2D} = \lim_{\rho \rightarrow \infty} 2\pi\rho \left| \frac{U^{scat}}{U^{inc}} \right|^2 \quad (3.17)$$

with the units of meters. An approximate formula to convert the echo length of a 2-D object to the RCS of a 3-D object (uniform length L in the third dimension) is given by

$$\sigma = \sigma_{2D} \frac{2L^2}{\lambda} \quad (3.18)$$

where λ is the illuminating wavelength. Most of the following work expresses RCS in dBsm. This is computed as

$$\sigma_{dBsm} = 10 \log \sigma (m^2) \quad (3.19)$$

Often the dBsm subscript will not be used, but in either case the units will be clearly presented.

RCS of Partial Cylinder

UTD is generally considered as a technique for conducting targets. Until now, most predictions for foamed plastic target supports used either a modified form of Physical Optics or surface integrals to determine the scattered field. This section uses the UTD theory to calculate the RCS of a two dimensional target support column.

The selected column is shown in Figure 3.7. This shape was chosen because it contains all of the mechanisms described previously, the diffraction from a straight and a curved edge and also convex and concave reflections.

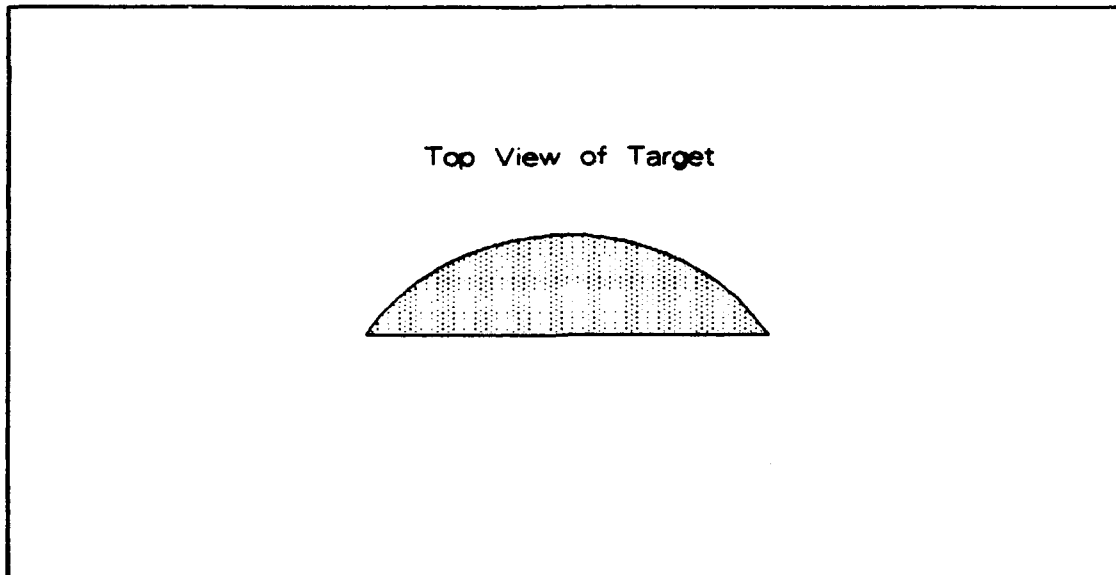


Figure 3.7. Target Support Column used for Prediction Model

The target is constructed from one pound per cubic foot expanded bead polystyrene (EPS), relative permittivity of 1.021. Several variables are needed to describe the physical dimensions of the selected target, which will be referred to as a partial cylinder. These are left as variables so that this prediction model will work for all targets of this shape, regardless of the actual size.

Figure 3.8 shows the pertinent variables. The origin is the cross, which is the center of curvature of the curved surface. The angle θ and the distance R locates the source and receiver. Theta varies from 0 to 180 degrees since the RCS is symmetric from 180 to 360 degrees. Distance d is the length of the flat surface, while a is the radius of the curved surface. For this model $d \leq 2a$; that is the

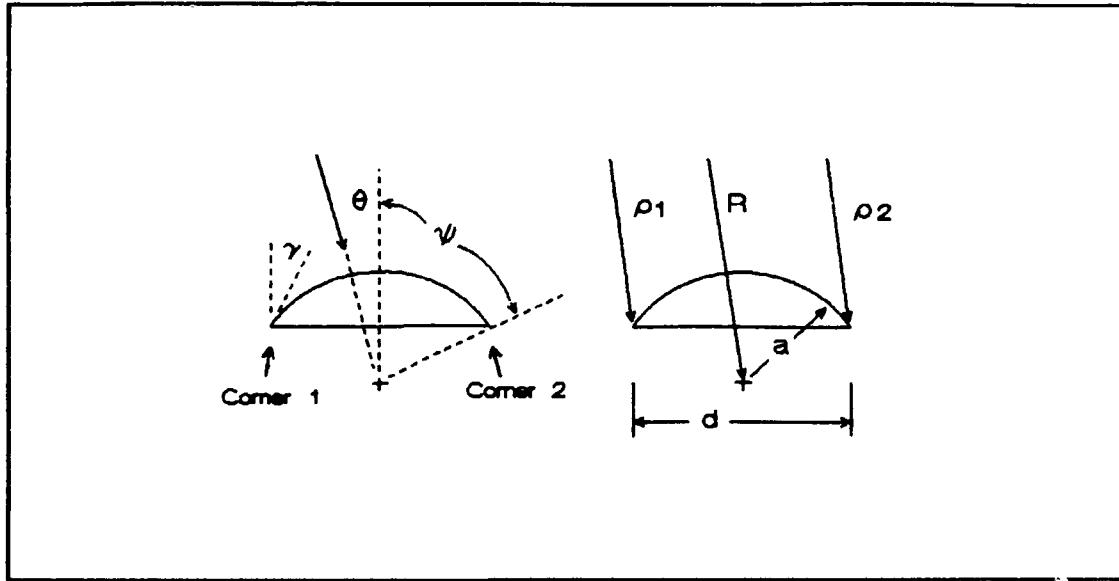


Figure 3.8. Physical Dimensions of the Target

cylinder is a half cylinder or less. The distance from the source to corner 1 is ρ_1 , and from source to corner 2 is ρ_2 .

Initial Definitions This section defines the variables from Figure 3.8. It assumes that the quantities a and d are given. The variables are defined in terms of θ , R , a and d .

$$\psi = \sin^{-1}\left(\frac{a}{2d}\right) \quad (3.20)$$

$$\gamma = \frac{\pi}{2} - \psi \quad (3.21)$$

$$\rho_1 = R - a \cos(\psi - \theta) \quad (3.22)$$

$$\rho_2 = R - a \sin(\gamma - \theta) \quad (3.23)$$

$$\begin{aligned} \rho &= R - a & \text{if } \theta < \frac{\pi}{2} \\ \rho &= R + a & \text{if } \theta > \frac{\pi}{2} \end{aligned} \quad (3.24)$$

where ρ is the distance along the path of R to the curved face of the column, where a reflection takes place.

Regions of Interest The plot of the cylinder RCS versus θ is symmetric about $\theta = 180^\circ$, therefore only this area is studied. For any given incidence angle, there are seven possible scattering mechanisms that will be considered. The equations for these mechanisms change with θ . For example, when $\theta < \psi$ there is a ray which reflects from the convex surface back to the receiver. This reflection term does not exist for $\theta > \theta$.

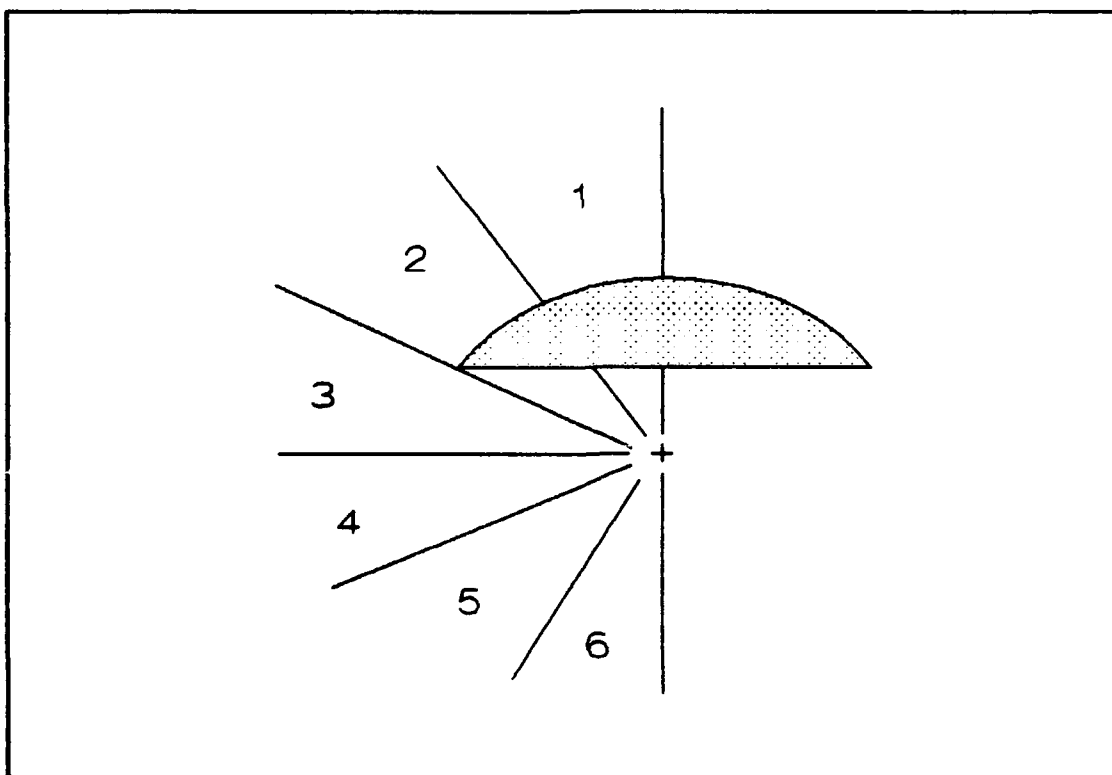


Figure 3.9. Regions Surrounding the Partial Cylinder

Figure 3.9 and Table 3.1 define the boundaries of the regions of interest. At the boundaries of these regions, the scattering mechanisms change, and the total scattering must be reevaluated.

Table 3.1. Regions of Interest

| | |
|----------|---|
| Region 1 | $0 \leq \theta \leq \gamma$ |
| Region 2 | $\gamma < \theta \leq \psi$ |
| Region 3 | $\psi < \theta \leq \pi/2$ |
| Region 4 | $\pi/2 < \theta \leq \pi/2 + \gamma$ |
| Region 5 | $\pi/2 + \gamma < \theta \leq \pi - \gamma$ |
| Region 6 | $\pi - \gamma < \theta \leq \pi$ |

Since a and d are the physical parameters of the cylinder, changing them changes the relative size of the regions. For example, if $d = 2a$, then the column is a half cylinder, and regions 3 and 4 do not exist. The RCS model must account for the variability of the regions.

Scattering Mechanisms Overview The total scattered field is the complex sum of the seven individual scattering mechanisms. Both corner 1 and corner 2 each have three diffracted fields, since two reflection shadow boundaries (RSBs) and one incident shadow boundary (ISB) are produced at either corner for any angle of incidence (as shown in Figure 3.10 for corner 1). The c and f subscripts indicates if the RSB was caused by a curved or flat surface. The additional mechanism results from a direct reflection from either the convex surface when in regions 1 and 2, or from the concave surface when in regions 5 and 6.

In region 1, the incident rays reach corner 2 through free space. In region 2, incident rays must penetrate the target to reach corner 2, hence the distinction in the regions. This same distinction is needed for regions 5 and 6 because of rays near corner 1.

The diffraction coefficient presented in Eq. (3.11) must be further modified to describe a penetrable two dimensional target. As an

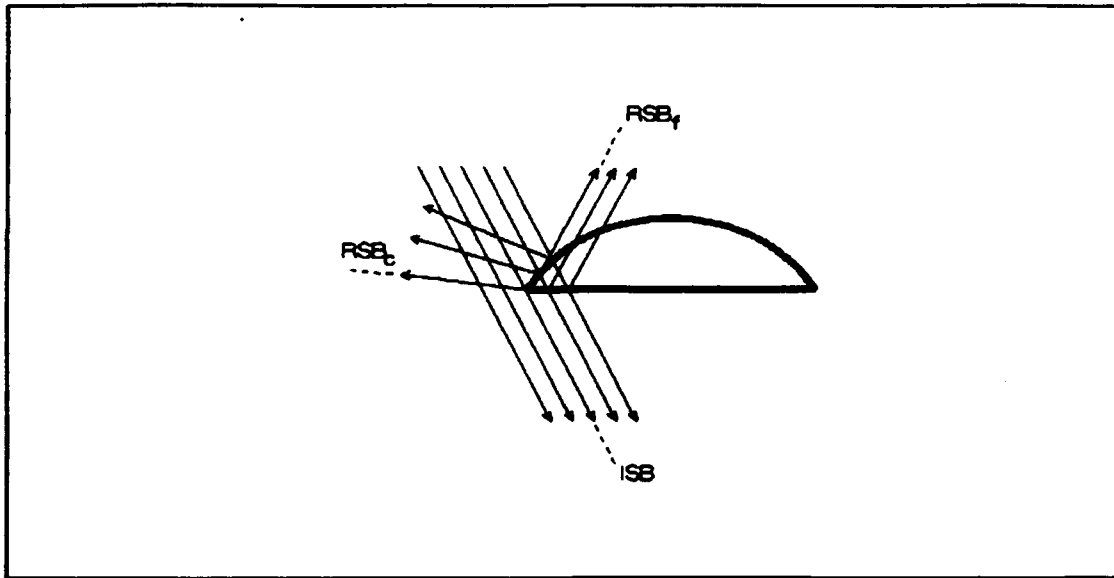


Figure 3.10. Shadow Boundaries Formed by Corner 1

example, the diffraction coefficient of RSB_t in Figure 3.11 must be scaled by the discontinuity on either side of the boundary. To the left of the boundary, there are no reflected rays, so the field is zero. To the right of the boundary, each ray has been transmitted through the convex surface, then reflected from the flat surface, and transmitted through the concave surface. The total diffracted field associated with this RSB is

$$U^d = U^i(Q_E) \exp \frac{-jk\rho l}{\sqrt{\rho l}} [\tau_{s,h} \Gamma_{s,h} \tau_{s,h}] D_R \quad (3.25)$$

The term in the square brackets of Eq. (3.25) will be called the scaling factor, and as noted by the subscripts, each coefficient depends on the polarization. Reflection and transmission coefficients for dielectric interfaces are normally expressed in terms of their angle of incidence. The Fresnel reflection and transmission coefficients are subject to conditions on the incidence angle known as critical angle and Brewster angle. At these extremes, the reflection coefficient equals one

or zero, respectively [12:235]. Allowing either case produced large errors in the scaling factors, and so in the RCS prediction. For example, if the reflection coefficient were allowed to equal one ($\Gamma = 1$) the reflected field would equal that of a conductor. Because of these artifacts from the Fresnel coefficients, the scaling factors were based on the reflection and transmission coefficients for normal incidence.

Measurements have confirmed that this model predicts the scattering better than using the angle dependent coefficients. Therefore, the terms $\tau_{s,h}$ and $\Gamma_{s,h}$ will be used in the rest of this thesis to represent the reflection and transmission coefficient for normal incidence. The subscripts will be maintained, as the polarization partially determines the sign of the coefficient.

Incident Field Expressions used for the scattered field have all used terms such as $U^i(Q_r)$ to mean the incident field at the reflection or diffraction point. This term was used for simplicity, but the definitions are presented here. For corner 1, the incident field is

$$U^i(c1) = \frac{e^{-j k \rho_1}}{\sqrt{\rho_1}} \quad (3.26)$$

For corner 2,

$$U^i(c2) = \frac{e^{-j k \rho_2}}{\sqrt{\rho_2}} \quad (3.27)$$

and to the reflection point

$$U^i(\rho) = \frac{e^{-j k \rho}}{\sqrt{\rho}} \quad (3.28)$$

where the distances ρ_1 , ρ_2 , and ρ are defined in Eqs. (3.22) through (3.24), relative to R. The amplitude and phase reference is the source, so the source field is assumed to be $1\angle 0^\circ$ (magnitude of one, phase angle zero). Note that in Eq. (3.2) a term similar to these is given for the

diffraction coefficient. This accounts for the propagation from the scattering point back to the receiver. The exponential term describes the phase change over the distance, and the square root term describes how the field attenuates with distance.

Scattered Field by Region

Region 1 In this region, the incident rays reach both corner 1 and 2 without penetrating the cylinder. The total scattered field is the sum of 7 mechanisms, three from each corner and a reflection from the convex surface. The shadow boundaries and reflection point are shown in Figure 3.12.

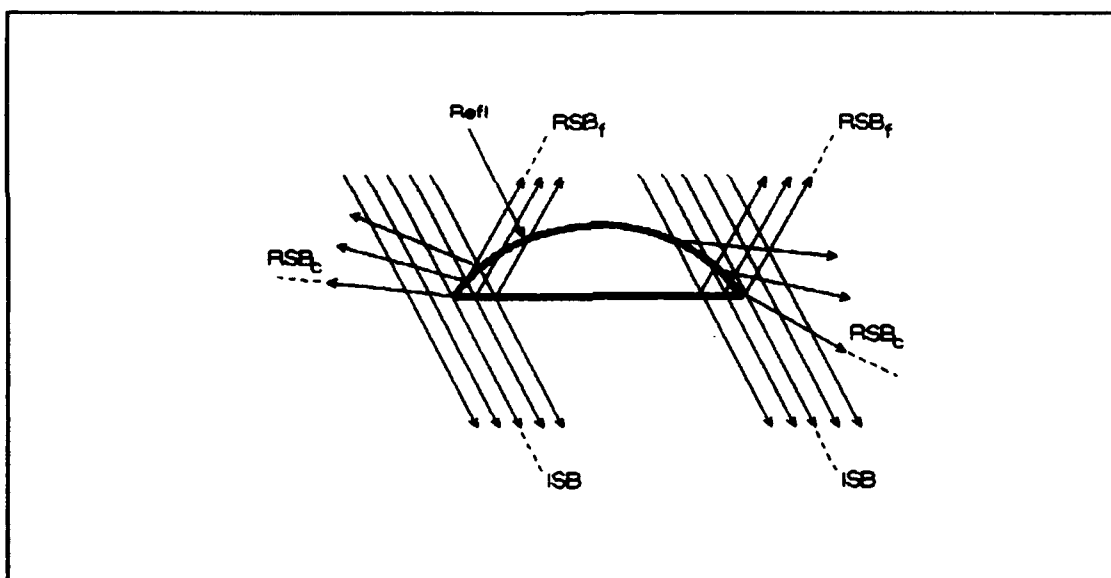


Figure 3.12. Example of Shadow Boundaries for Corner 1

The scattered field at the receiver can be written as

$$\begin{aligned}
 U^{scat} &= U_1^{dif} + U_2^{dif} + U^{ref} \\
 &= U_1^{rsbf} + U_1^{rsbc} + U_1^{isb} + U_2^{rsbf} + U_2^{rsbc} + U_2^{isb} + U^{ref}
 \end{aligned}
 \tag{3.29}$$

where

$$U_1^{rsbf} = \frac{e^{-2jkp_1}}{\rho_1} [\tau_{s,h} \Gamma'_{s,h} \tau'_{s,h}] D_R(\frac{\pi}{2} + \theta, \rho_1) \quad (3.30)$$

$$U_1^{rsbf} = \frac{e^{-2jkp_1}}{\rho_1} [\Gamma_{s,h}] D_R(\theta + \gamma, \frac{a}{2}) \quad (3.31)$$

$$U_1^{isb} = \frac{e^{-2jkp_1}}{\rho_1} [1 - \tau_{s,h} \tau'_{s,h}] D_I(\frac{\pi}{2} + \theta, \rho_1) \quad (3.32)$$

$$U_2^{rsbf} = \frac{e^{-2jkp_2}}{\rho_2} [\tau_{s,h} \Gamma'_{s,h} \tau'_{s,h}] D_R(\frac{\pi}{2} - \theta, \rho_2) \quad (3.33)$$

$$U_2^{rsbf} = \frac{e^{-2jkp_2}}{\rho_2} [\Gamma_{s,h}] D_R(\gamma - \theta, \frac{a}{2}) \quad (3.34)$$

$$U_2^{isb} = \frac{e^{-2jkp_2}}{\rho_2} [1 - \tau_{s,h} \tau'_{s,h}] D_I(\frac{\pi}{2} - \theta, \rho_2) \quad (3.35)$$

and

$$U^{ref} = \frac{e^{-2jk(R-a)}}{\sqrt{R-a}} \sqrt{\frac{\frac{a}{2}}{R - \frac{a}{2}}} \Gamma_{s,h} \quad (3.36)$$

which can be further simplified for far field (R large) as

$$U^{ref} = \frac{e^{-2jk(R-a)}}{R} \sqrt{\frac{a}{2}} \Gamma_{s,h} \quad (3.37)$$

In these equations, the prime (') notation on the reflection and transmission coefficients indicates that the rays move from the EPS into the air, the unprimed indicates that the rays goes from air to EPS. In some equations, L^R has been replaced by $a/2$.

Because of the large number of mechanisms used, predictions were made on each to determine its relative magnitude throughout the entire 180 degrees. It was found that the terms associated with the incident

shadow boundaries were negligible compared to the other terms. The reason is that the discontinuity here is not as abrupt as that of the RSB, and so the scattering is weaker. Measurements confirmed this fact, as will be discussed in Section IV. In the other regions, the diffracted term associated with the ISB has been dropped.

Region 2 The scattering terms in this region are very similar to region 1. The differences can be seen in Figure 3.12.

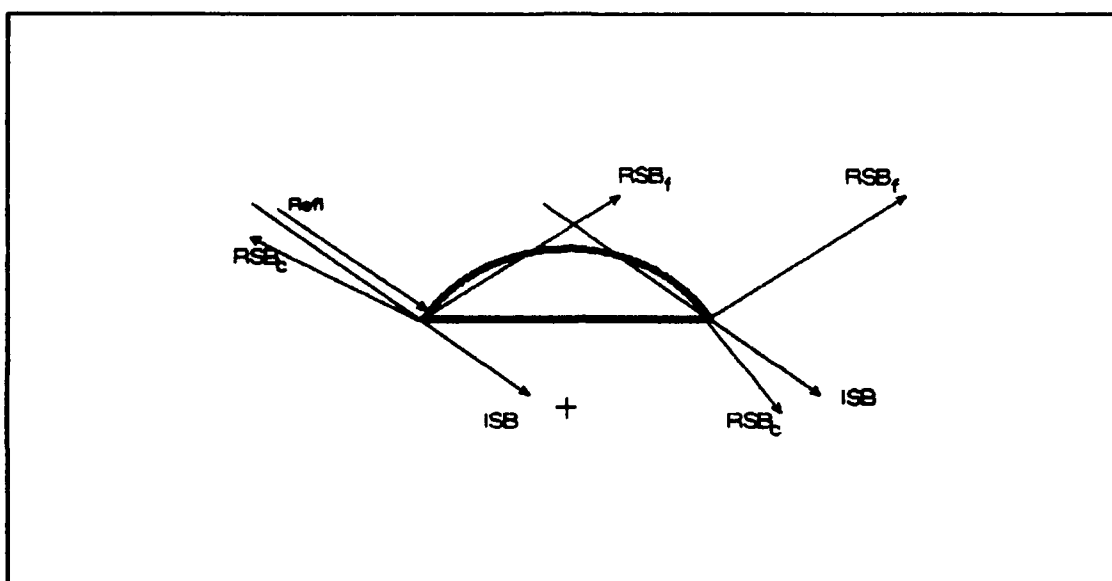


Figure 3.12 Shadow Boundaries for Region 2

All of the terms associated with corner 1 and the reflection term remain the same. The incident rays near corner 2 now reflect from the concave side of the curved face, moving the RSB to the opposite side of the ISB. The RSB term (U^{rsbc}) is modified by changing the scale factor and the distance term, thus

$$U_2^{rsbc} = \frac{e^{-2j\kappa p^2}}{\rho^2} [\tau_{s,h} \Gamma'_{s,h} \tau'_{s,h}] D_R(\theta - \gamma, \frac{-a}{2}) \quad (3.38)$$

Note that the scale factor for the ISB of corner 2 equals zero in this region. The rays on both sides of the ISB penetrate the target, and no discontinuity exists.

Region 3 The diffraction terms do not change from region 2 to region 3. However, the direct reflection stops when $\theta > \phi$. The diffraction term U_1^{rsbf} is strong enough to smooth out the loss of this term, however it decreases rapidly. Without the reflection term, the backscattered field in this region is small.

Region 4 This region begins when $\theta > 90$ degrees. Incident rays now strike the curved face of corner 1 and the bottom of the cylinder, as shown in Figure 3.14. There are no normal curved surfaces, so there are no direct reflection terms. In region 4, the total backscattered field is

$$U^{scat} = U_1^{rsbf} + U_1^{rsbc} + U_2^{rsbf} + U_2^{rsbc} \quad (3.39)$$

The angle ϕ used in the diffraction coefficient is now measured from the bottom face of the flat surface as shown in Figure 3.13. This change is for convenience only.

The individual diffracted fields are expressed as

$$U_1^{rsbf} = \frac{e^{-2j\kappa\rho_1}}{\rho_1} [\Gamma_{s,h}] D_R\left(\frac{3\pi}{2} - \theta, \rho_1\right) \quad (3.40)$$

$$U_1^{rsbc} = \frac{e^{-2j\kappa\rho_1}}{\rho_1} [\Gamma_{s,h}] D_R\left(\gamma + \theta, \frac{a}{2}\right) \quad (3.41)$$

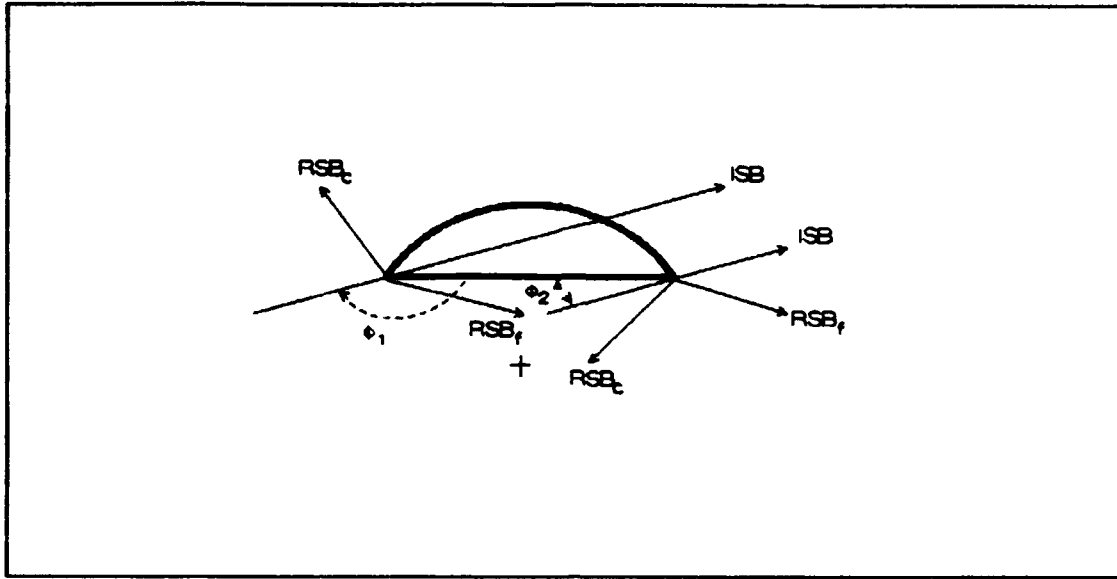


Figure 3.13. Shadow Boundaries for Region 4

$$U_2^{rsbf} = \frac{e^{-2jk\rho_2}}{\rho_2} [\Gamma_{s,h}] D_R(\theta - \frac{\pi}{2}, \rho_2) \quad (3.42)$$

$$U_2^{rsbc} = \frac{e^{-2jk\rho_2}}{\rho_2} [\tau_{s,h} \Gamma'_{s,h} \tau'_{s,h}] D_R(\theta - \gamma, \frac{-a}{2}) \quad (3.43)$$

When the incident field enters region 5, a direct reflection will occur from the concave inner surface. This is a strong mechanism, so U_2^{rsbc} increases near the region boundary to smooth out the total field.

Region 5 The diffracted fields in this region are identical to those of region 4. However, the term for the concave reflection must be added to the total field expressed in Eq. (3.39), so that

$$U^{scat} = U_1^{rsbf} + U_1^{rsbc} + U_2^{rsbf} + U_1^{rsbc} + U^{ref} \quad (3.44)$$

The reflection term is

$$U^{ref} = \frac{e^{\frac{\pi}{2} - 2jk(R+a)}}{R} \sqrt{\frac{a}{2}} \Gamma_{s,h} \quad (3.45)$$

where the far field approximation has been used as in Eq. (3.37). The $\pi/2$ phase shift is used since the reflected rays pass through a caustic. This can be seen in Figure 3.14 (region 6).

Region 6 The scattered field of Eq. (3.44) also applies in this region. However, the term U_1^{rsdc} must be modified. As shown in Figure 3.14, the incident rays reflect from the inside of the curved face of corner 1.

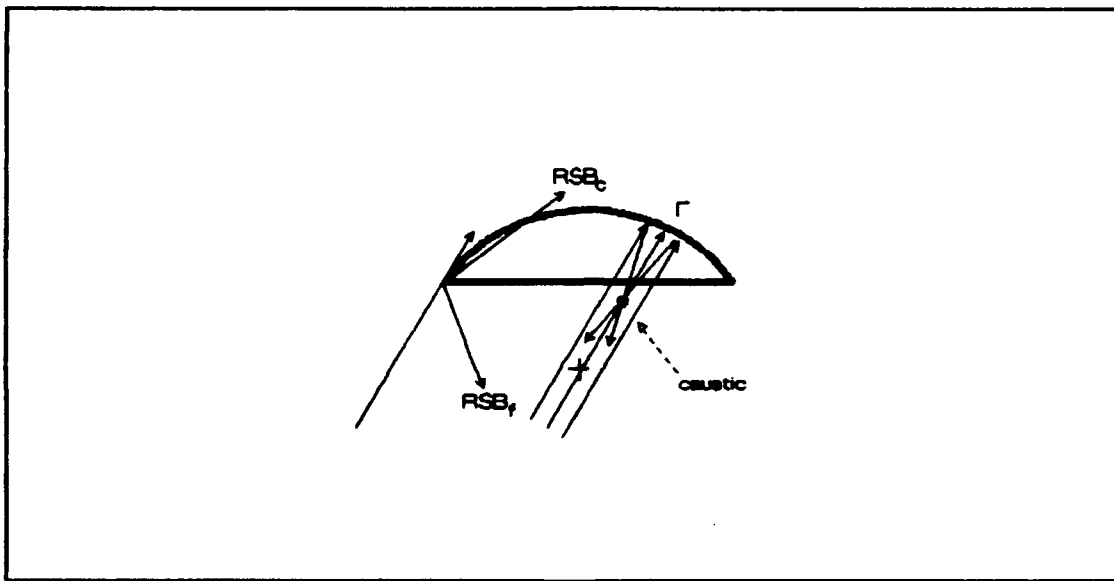


Figure 3.14. Curved Face RSB and Reflection in Region 6

The scaling factor, the distance parameter, and ϕ are affected, and

$$U_1^{rsbf} = \frac{e^{-2j\kappa\rho_1}}{\rho_1} [\tau_{s,h} \Gamma'_{s,h} \tau'_{s,h}] D_R\left(\frac{3\pi}{2} - \theta + \psi, \frac{-a}{2}\right) \quad (3.46)$$

Radar Cross Section of the Target The total scattered field in any region can be converted to an RCS value using Eqs. (3.17) through (3.19). The RCS is a function of the incidence angle θ , and the pattern

is symmetric about $\theta = 180$ degrees. In the calculations, the distance $R = 10,000\lambda$; to ensure the far zone behavior.

Two columns were constructed so that the prediction could be compared to measured data. One was a partial cylinder and the other a half cylinder. Both columns were 10 inches in height, and the radius of curvature 'a' was 5 inches. For the partial cylinder, the distance across the flat side 'd' was 8.625 inches, and for the half cylinder, $d=10$ inches.

The RCS was computed with a Fortran program which used all the parameters and equations given in this section (the prediction code is listed in Appendix A). Figures 3.15 through 3.18 show the comparisons of measured versus predicted RCS for both horizontal and vertical polarization, at a frequency of 10 GHz.

The predicted data matches the measured data very closely for the partial cylinder. For the half cylinder, the predicted values are about 2 dB higher than the measured, but still a very good match.

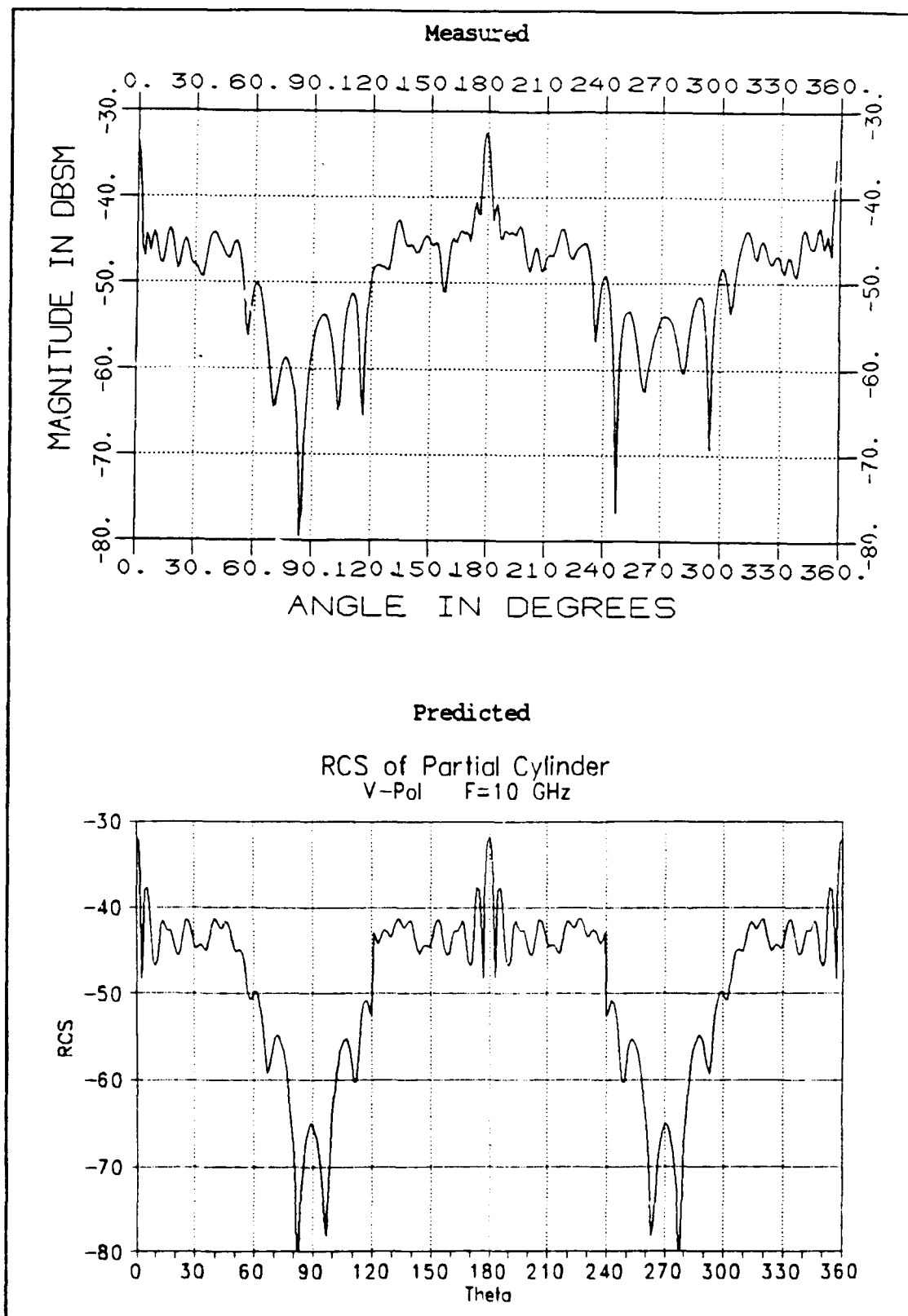


Figure 3.15. Measured Versus Theoretical RCS of the Partial Cylinder, Vertical Polarization, F=10 GHz

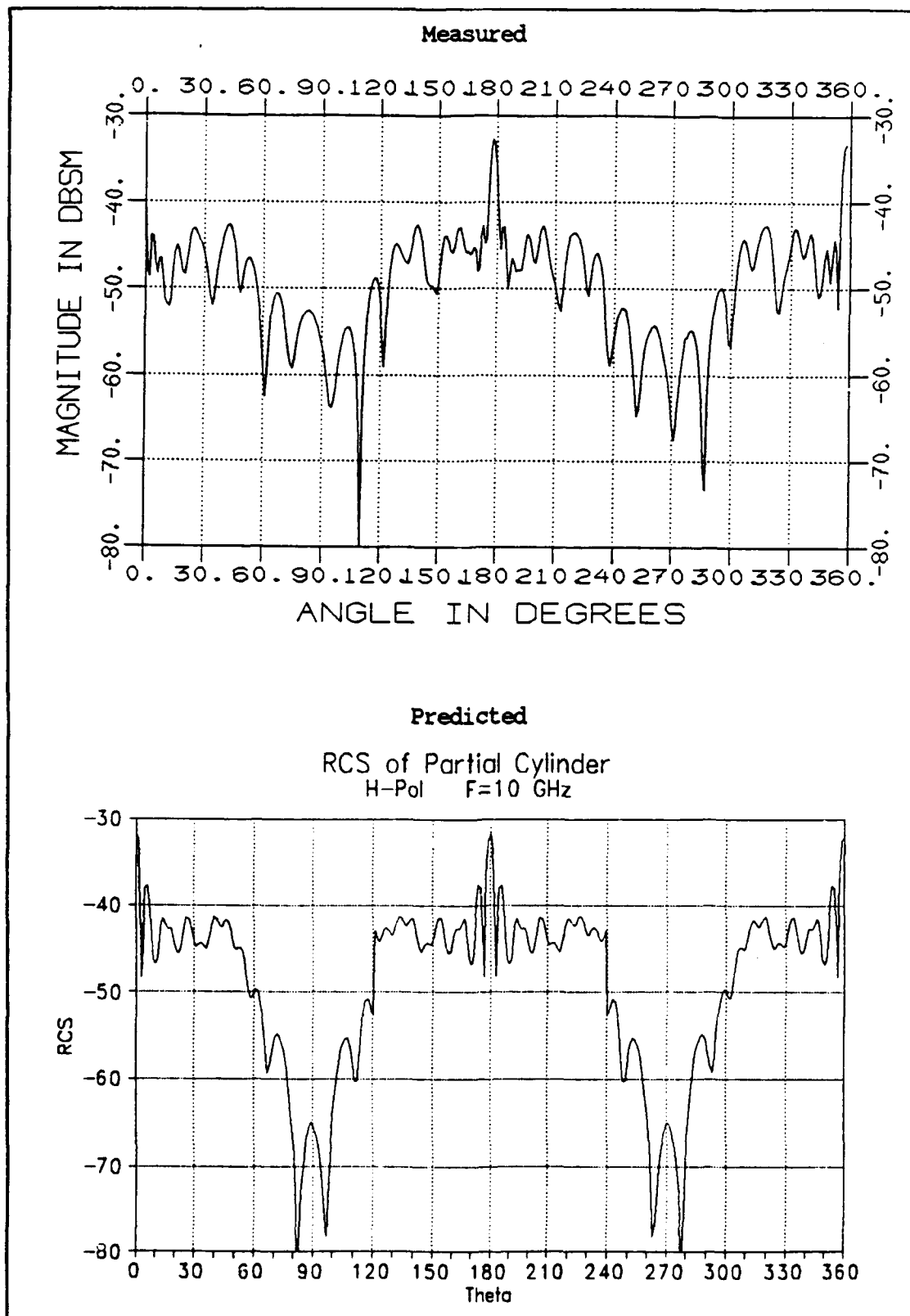


Figure 3.16. Measured Versus Theoretical RCS of the Partial Cylinder, Horizontal Polarization, F=10 GHz

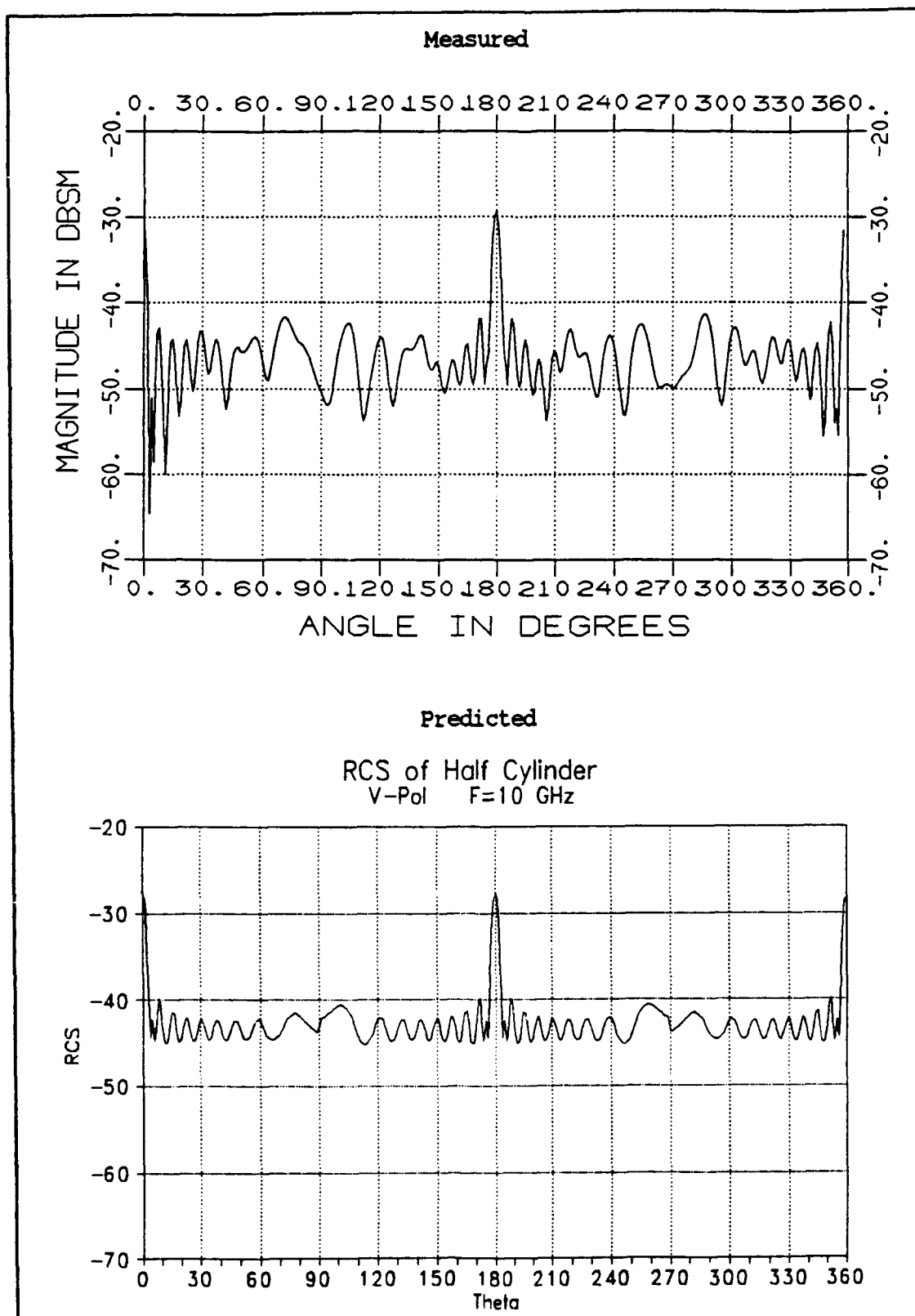


Figure 3.17. Measured Versus Theoretical RCS of the Half Cylinder, Vertical Polarization, F=10 GHz

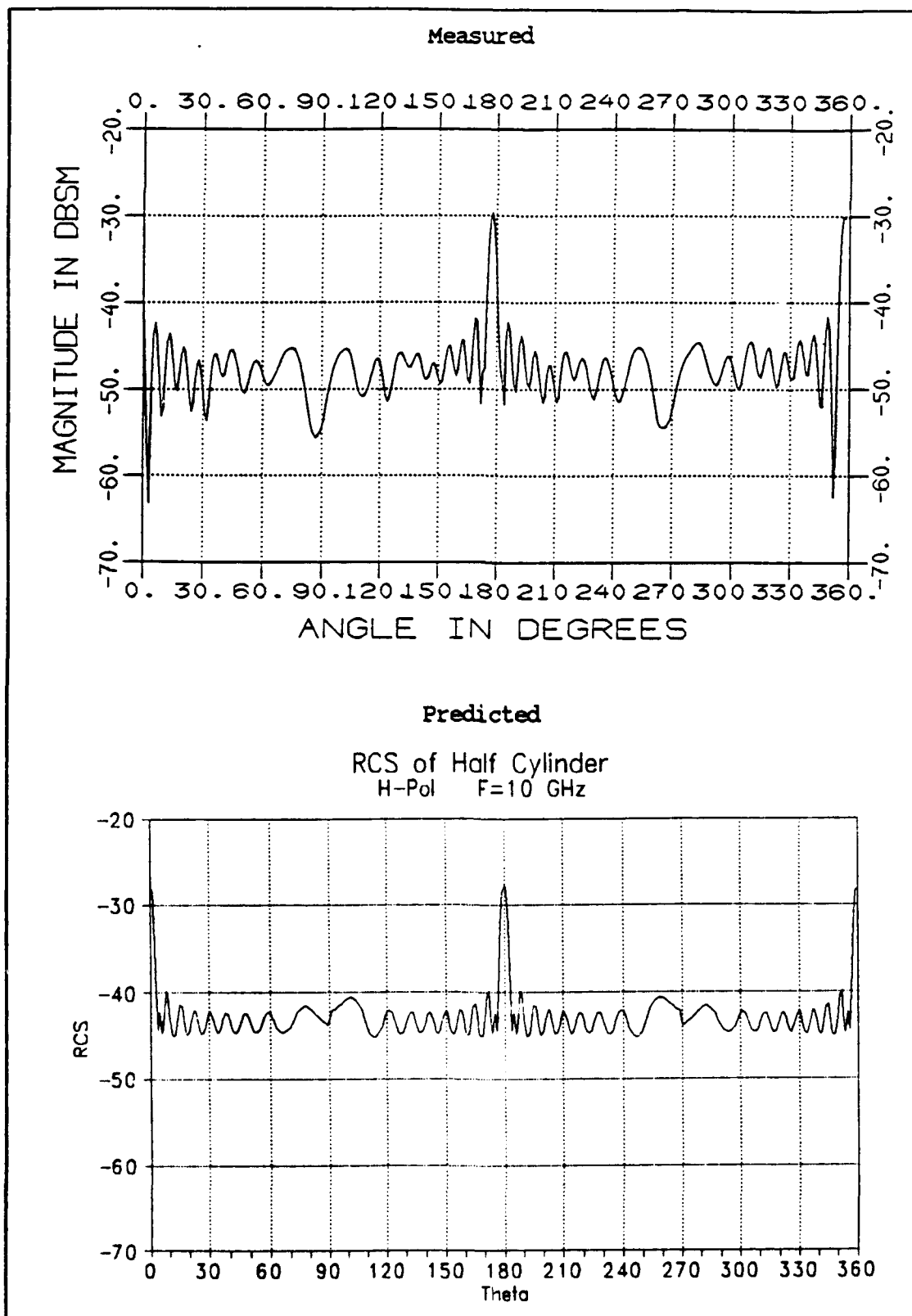


Figure 3.18. Measured Versus Theoretical RCS of the Half Cylinder, Horizontal Polarization, F=10 GHz

IV. Experimental Study of Column Design

Introduction

This chapter describes the experimental portion of this thesis. The goal was to study low RCS column shapes for 360 degree azimuth scans and from nose-on to ± 45 degree azimuth scans. A brief overview of the measurement equipment is presented, followed by the steps taken in the experimental study.

Measurement Set-Up

All experimental data was collected at the AFIT RCS Measurement Chamber. This laboratory uses the hardware shown in Figure 4.1. The measurement process is controlled by the 80386 computer and data processing is performed with the aid of the VAX.

Limitations The RCS Chamber is a far field system, meaning that the amplitude and phase of the signal are kept relatively constant throughout the quiet zone. Assuming that deviations of 1 dB in downrange amplitude and $\pi/8$ in crossrange phase shift are acceptable implies that targets on the order of one foot or less can be measured. Larger targets can be measured, but accuracy is reduced.

Columns made of EPS have much lower RCS than typical metal targets. The noise floor of the measurement system is the limiting factor in the minimum measurable RCS. Measurements of the noise floor taken at various times are included in Appendix B. During the discussions of the column measurements, the effect of the noise floor on the measurements will be addressed.

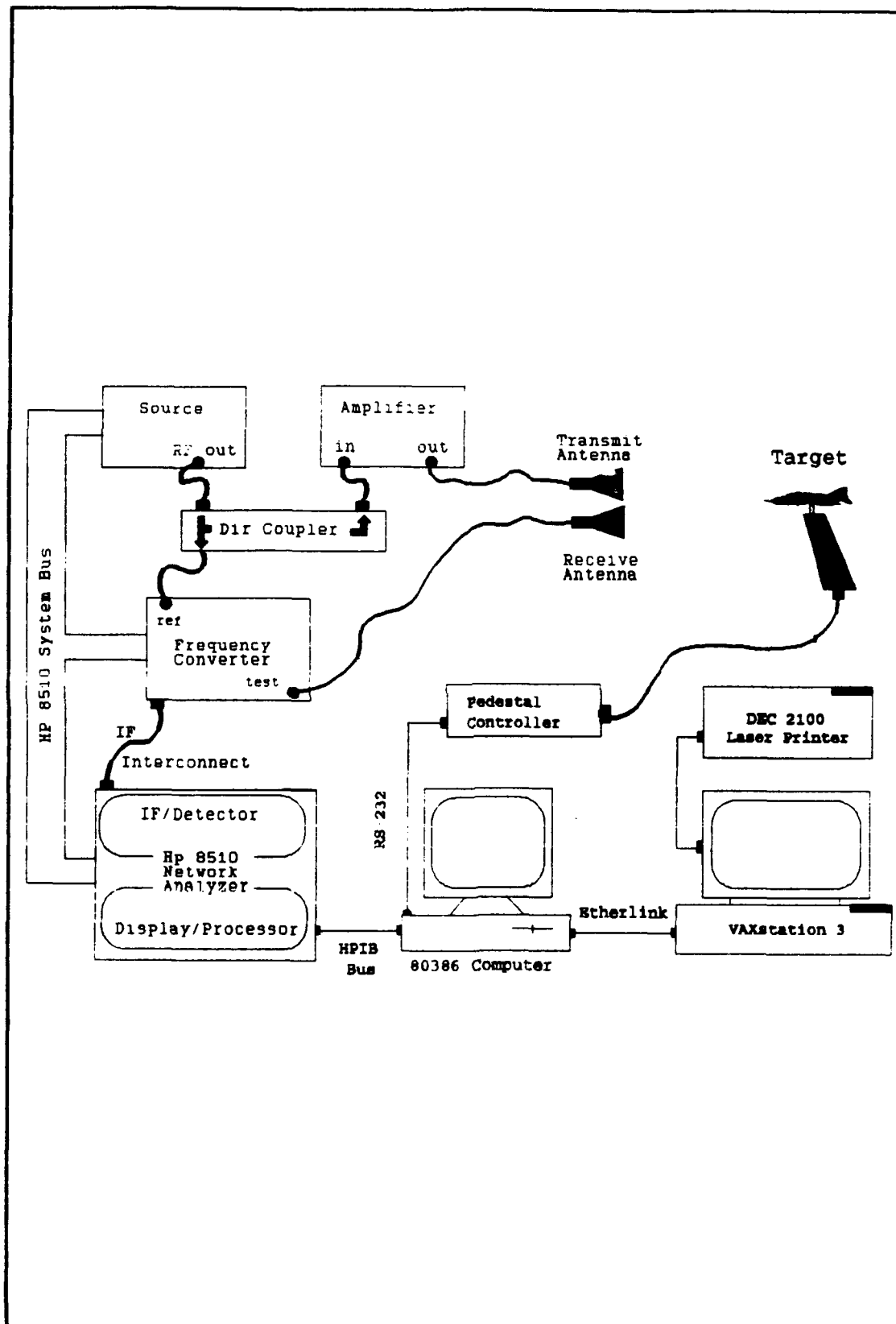


Figure 4.1. RCS Measurement Hardware [14]

Capabilities The RCS range can be used in one of two modes, azimuth scan and frequency scan. Azimuth scans measure the RCS of the target (at fixed frequency) versus azimuth angle from 0 to 360 degrees. This measurement is for one polarization and one frequency.

Frequency scans are made with the target at a fixed azimuth angle, which is selectable. The transmitter steps the frequency over a selected range at selected intervals. For this experiment, all frequency scans were from 6 - 18 GHz at .01 GHz intervals.

Frequency data can also be transformed (in software) to the time domain. This results in an impulse response of the target, which can be plotted as relative amplitude versus time. This type of plot is useful to identify specific scattering centers on a target. Once in the time domain, the operator can apply time gates to remove signals not due to the target, such as the return from the walls of the chamber, or from undesired features of the target. This and other software capabilities are known as post-processing. After gating, the data can be transformed back to the frequency domain. Because gating eliminates noise signals, the noise floor is seen to be reduced when transforming back to the frequency domain. All data presented in the form of frequency scans has been gated in the time domain.

Low RCS Support Columns

The most important consideration when designing support columns is the RCS of the support. It must be much lower than the target, so that the return from the column does not interfere with the target return. Ideally the target support would have negligible backscatter for all azimuth angles at all frequencies. Shapes such as an ogive can provide

minimal backscatter for most frequencies, but only over a limited sector of angles. Cylinders can be selected so that the return is zero for a particular frequency, however the bandwidth is exceptionally narrow. A compromise must be made between frequency and angle.

Two types of columns will be examined. Both assume that the frequency is arbitrary, so that single frequency cancellation is not a factor. The first type of column is used when the target's RCS must be measured for a full 360 degrees. The second type of column is used when the RCS will be measured for a limited sector of angles. For example, this type of measurement is used to determine the RCS of an aircraft around the nose, where the RCS is critical to survivability.

Full Azimuth Scans

The most common way to design support columns for full azimuth scans is to make them circularly symmetric. In [6] and [7], the RCS of a right circular cylinder was reduced by sloping the sides. For this experiment, the AFIT Fabrication Shop constructed four sloped cylindrical columns. The cross section of each is shown in Figure 4.2. Each was eight inches in height, and made from one pound per cubic foot density EPS.

The first column, labeled 'A', was a right circular cylinder (RCC), four inches in diameter. This is not a low RCS shape, but was used as a reference for the other columns. Each of the next three columns maintained the four inch diameter at the top to simulate columns with the same minimum weight bearing capacity. The second column, labeled 'B', had 10 degree sloped sides. Column 'C' had 20 degree sloped sides, while column 'D' had 30 degrees of slope.

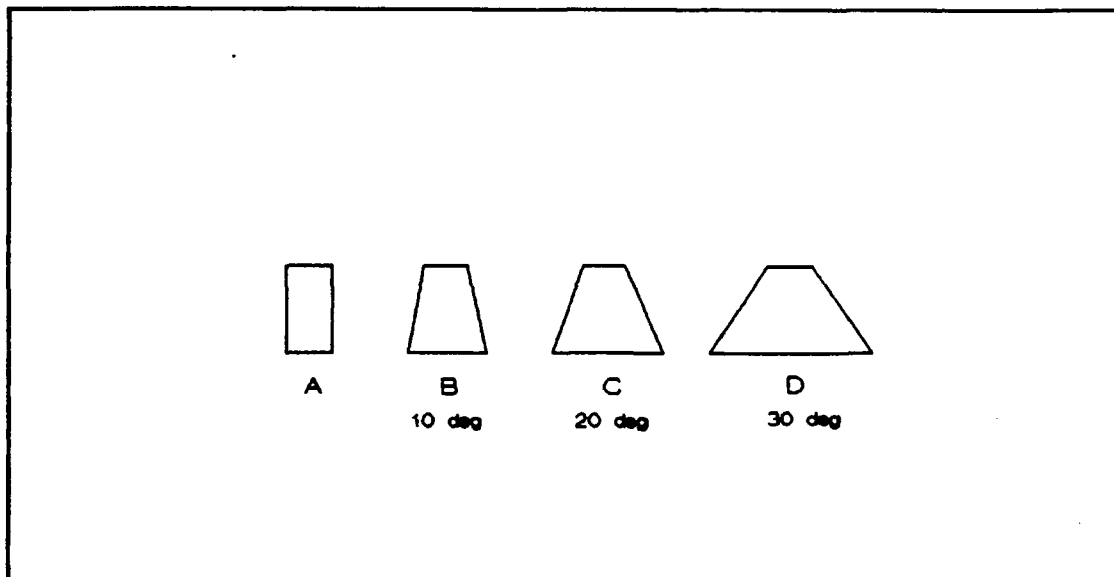


Figure 4.2. Cylindrical Columns

The purpose of this experiment was to determine what type of slope leads to lowest overall RCS across the frequency band of interest. Since the targets were symmetric, azimuth scans should have produced a flat line. Figure 4.3 shows the azimuth scan of the right circular cylinder with vertical polarization at 7 GHz. The plot is fairly flat as expected. Figure 4.4 contains the impulse and frequency response of this cylinder. A top view of the target is superimposed over the time domain plot. The time = 0 nanoseconds on the plot corresponds to the center of the range quiet zone. Since the time domain considers round trip time, 1 nanosecond can be scaled to approximately 6 inches.

Note that in the impulse response, the main scattering is due to reflections from the front and back surfaces. This can also be observed in the frequency domain plot. Here the overall shape is that of the sum of two scattering mechanisms adding in or out of phase due to frequency. Sloping the sides of the RCC should make the incident field reflect at an angle away from the receiver.

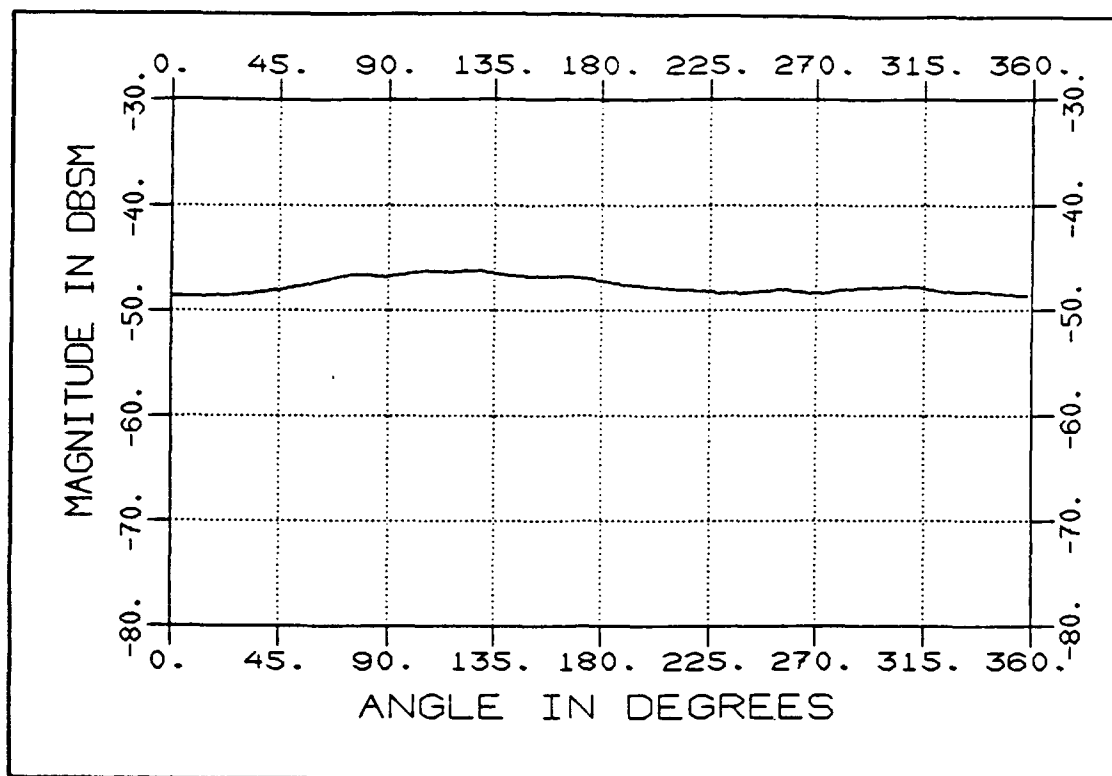


Figure 4.3. Azimuth Scan of Right Circular Cylinder,
Vertical Polarization, $F = 7$ GHz

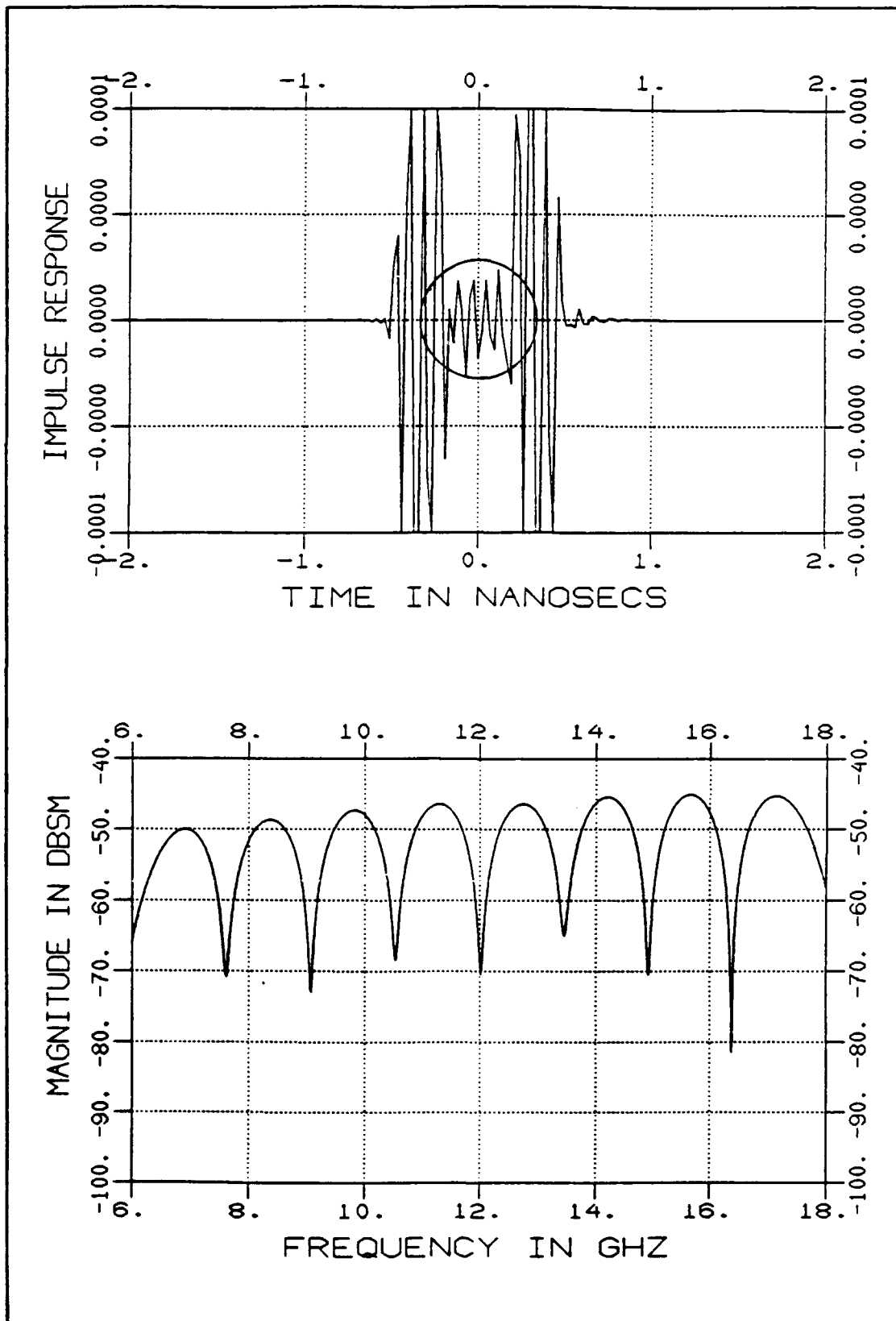


Figure 4.4. Impulse Response and Frequency Response for ROC, V-Pol

Figure 4.5 shows the azimuth scan plot for the 10 degree sloped cylinder. The plot is no longer smooth as in Figure 4.3. The RCS has reached a small enough level so that the noise floor interferes with the measurement. This same problem is apparent with the other two sloped columns (see plots in Appendix C).

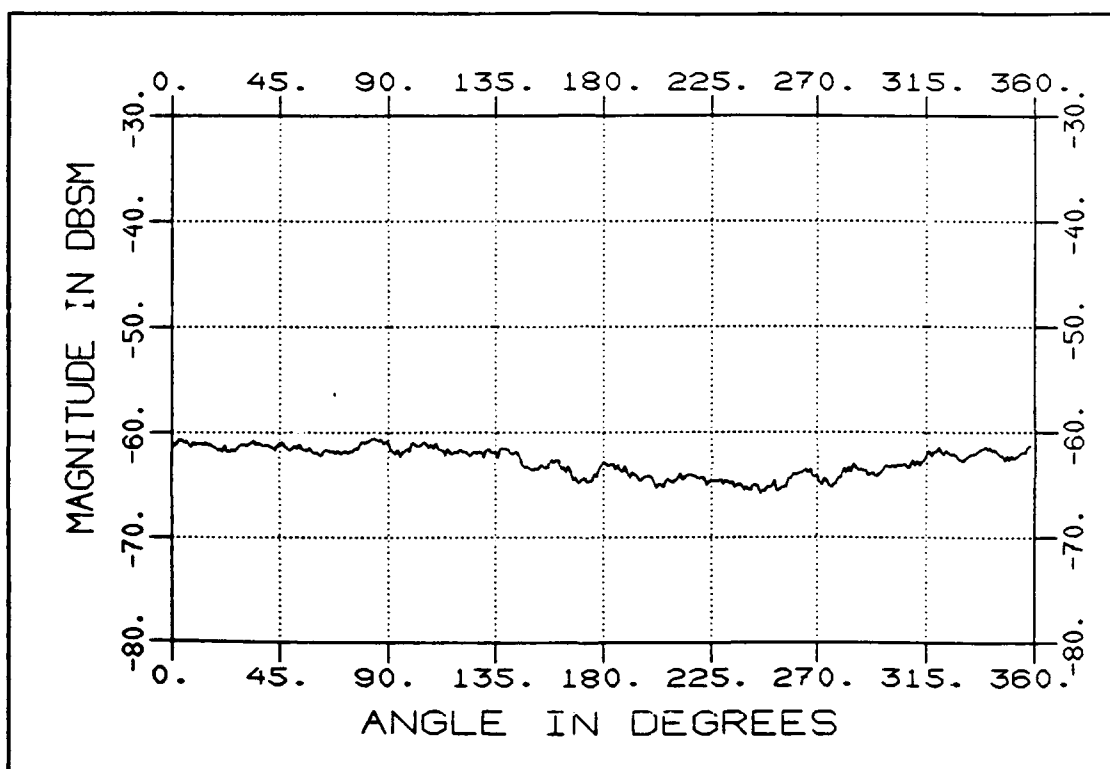


Figure 4.5. Azimuth Scan of 10 Degree Sloped Cylinder, Vertical Polarization, F = 7 GHz

A noise floor measurement made on the same day as the azimuth scans is shown in Figure 4.6. Noise floor measurements varied daily. Since the level of the plots is at the same level of the noise, the true return is masked.

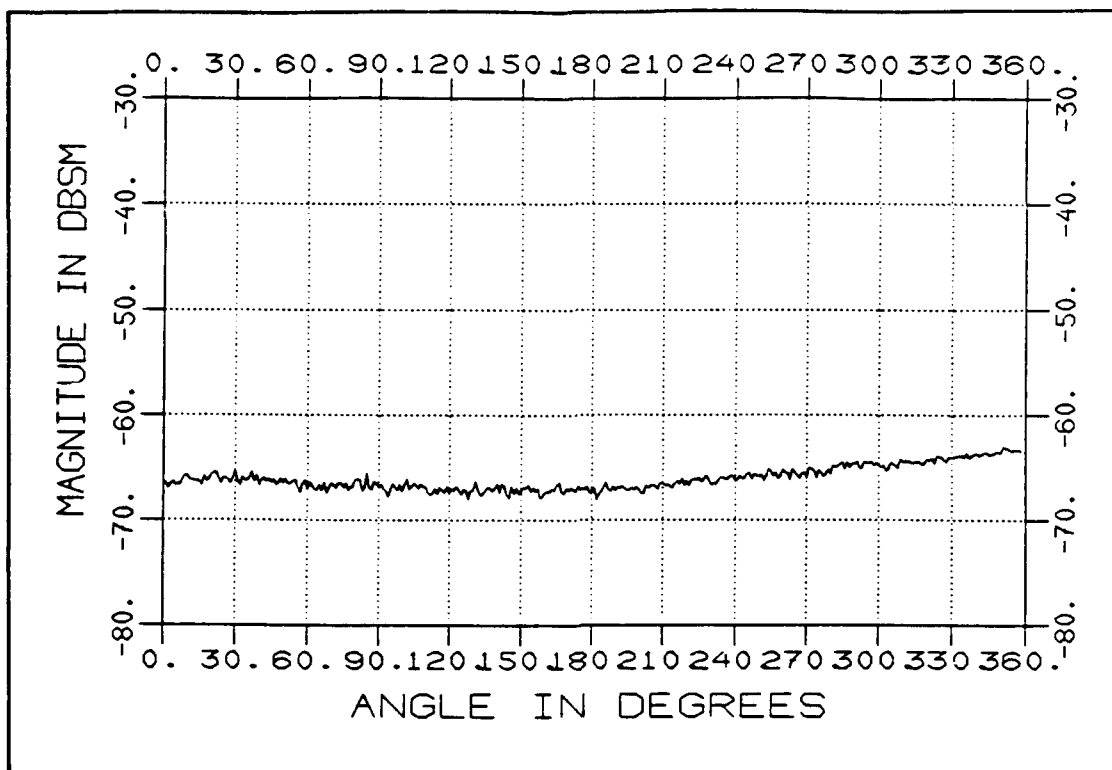


Figure 4.6. Noise Floor Measurement

Frequency scans of the columns provide useful information. Time domain and frequency response data is presented in Figure 4.7, Figure 4.8, and Figure 4.9 for the 10 degree, 20 degree, and 30 degree slopes, respectively. Similar plots for horizontal polarization are displayed in Appendix C.

The difference between the sloped column and the RCC is dramatic. The RCC peaks between -50 and -45 dBsm. For the 10 degree slope, the RCS is reduced to at least -67 dBsm across the entire frequency band. The impulse response shows that there is no dominant scattering mechanism. There are contributions from the bottom and top bases. Diffractions are expected here because of the abrupt change in the surface.

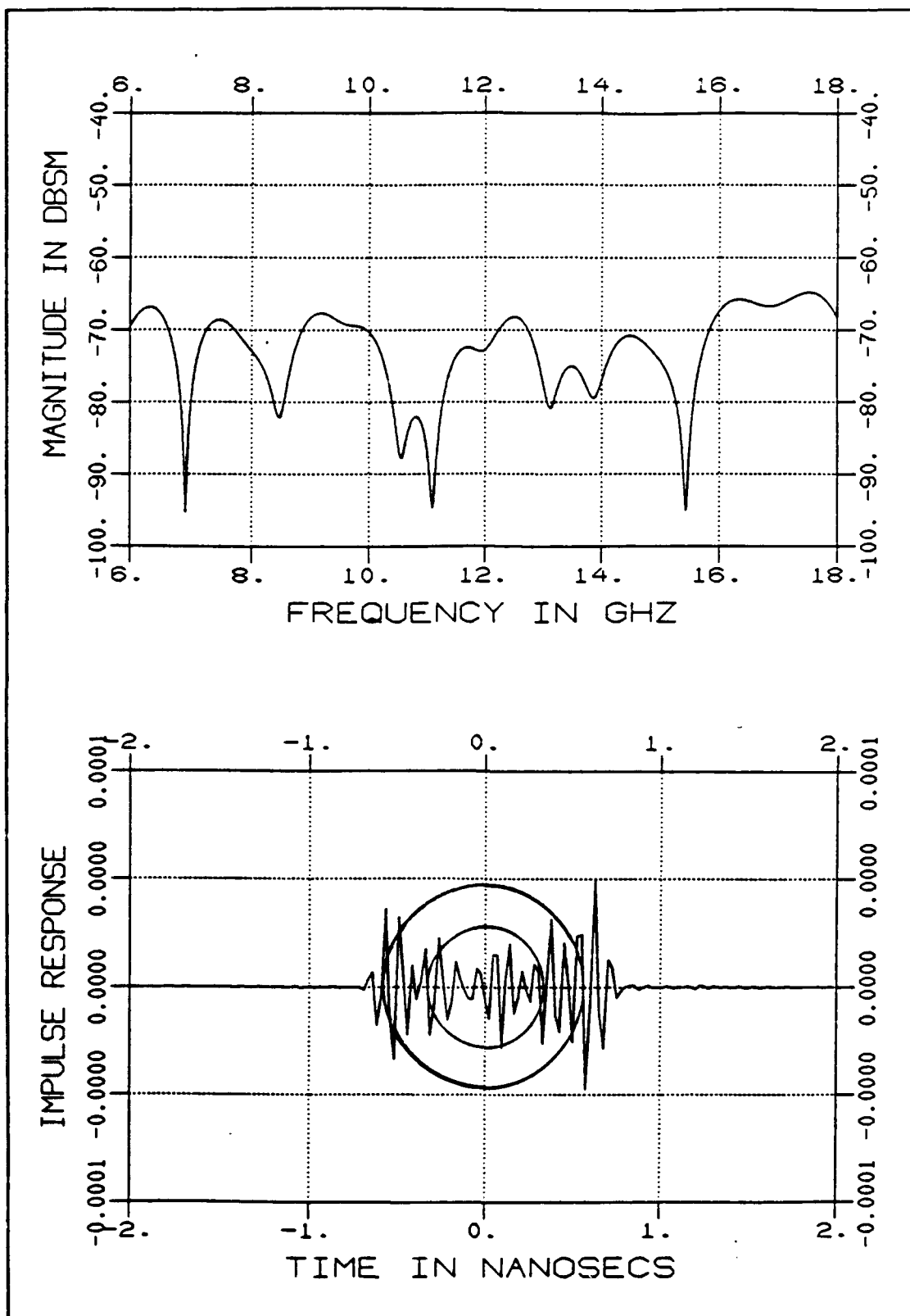


Figure 4.7. Frequency/Impulse Response of the 10 Degree Sloped Cylinder, Vertical Polarization

The difference between the 20 degree column (Figure 4.8) and the 10 degree column is not as apparent. At the lower frequencies, up to 10 GHz, the 20 degree cylinder is about 5 dB lower than the 10 degree cylinder. At the higher frequencies, the two perform nearly the same. The same trend is seen for the horizontal polarization.

The 30 degree cylinder (Figure 4.9) measured either the same as or slightly higher than the 20 degree cylinder. No advantage is realized by going to this high of a slope angle. The same holds true for horizontal polarization.

In the sloped cylinder measurements, it must be realized that the levels are low enough that they are approaching the frequency scan noise floor. While the following figures clearly show the relative RCS of the different cylinders, the smaller measured values may not be absolute.

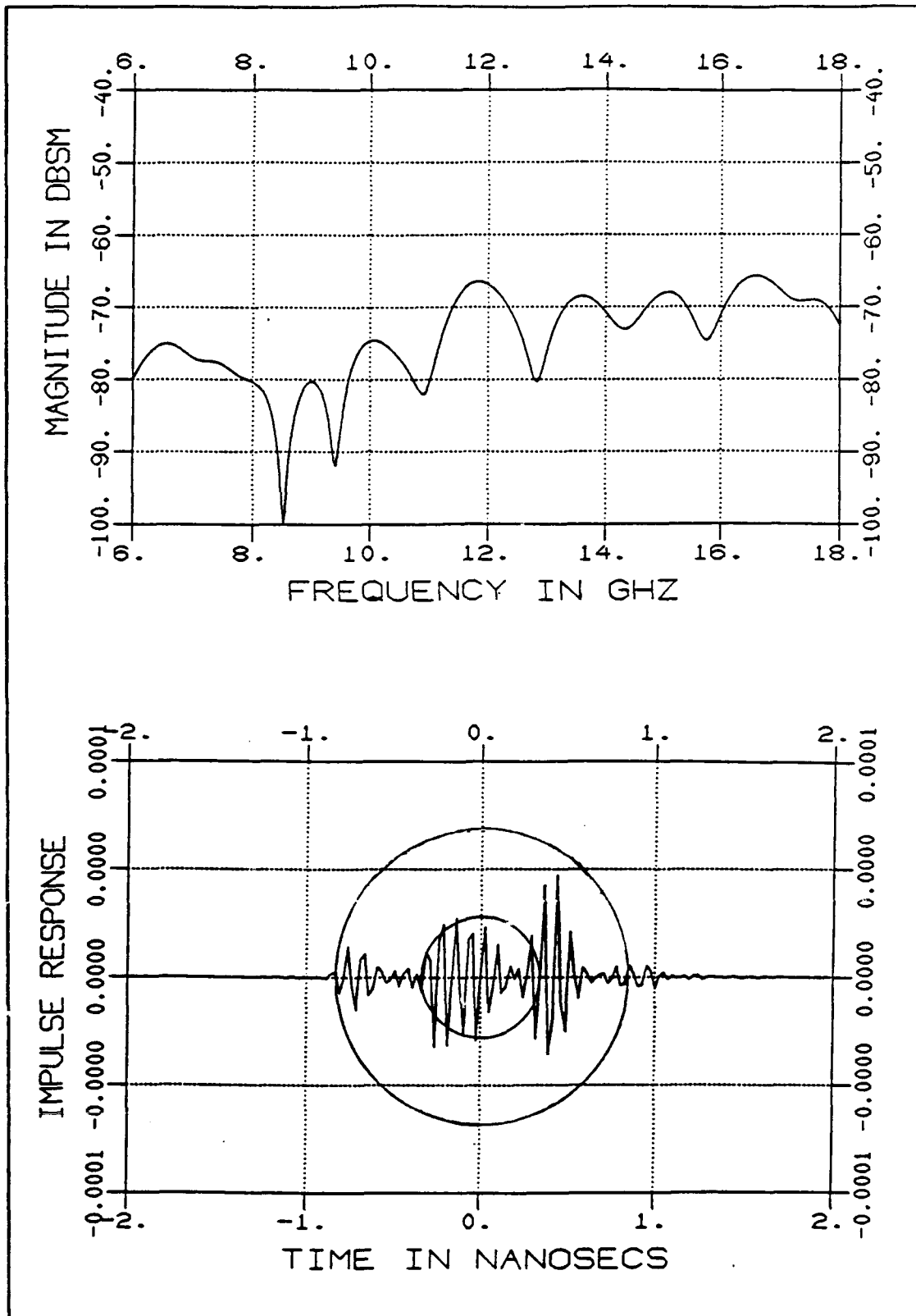


Figure 4.8 Frequency/Impulse Response of the 20 Degree Sloped Cylinder, Vertical Polarization

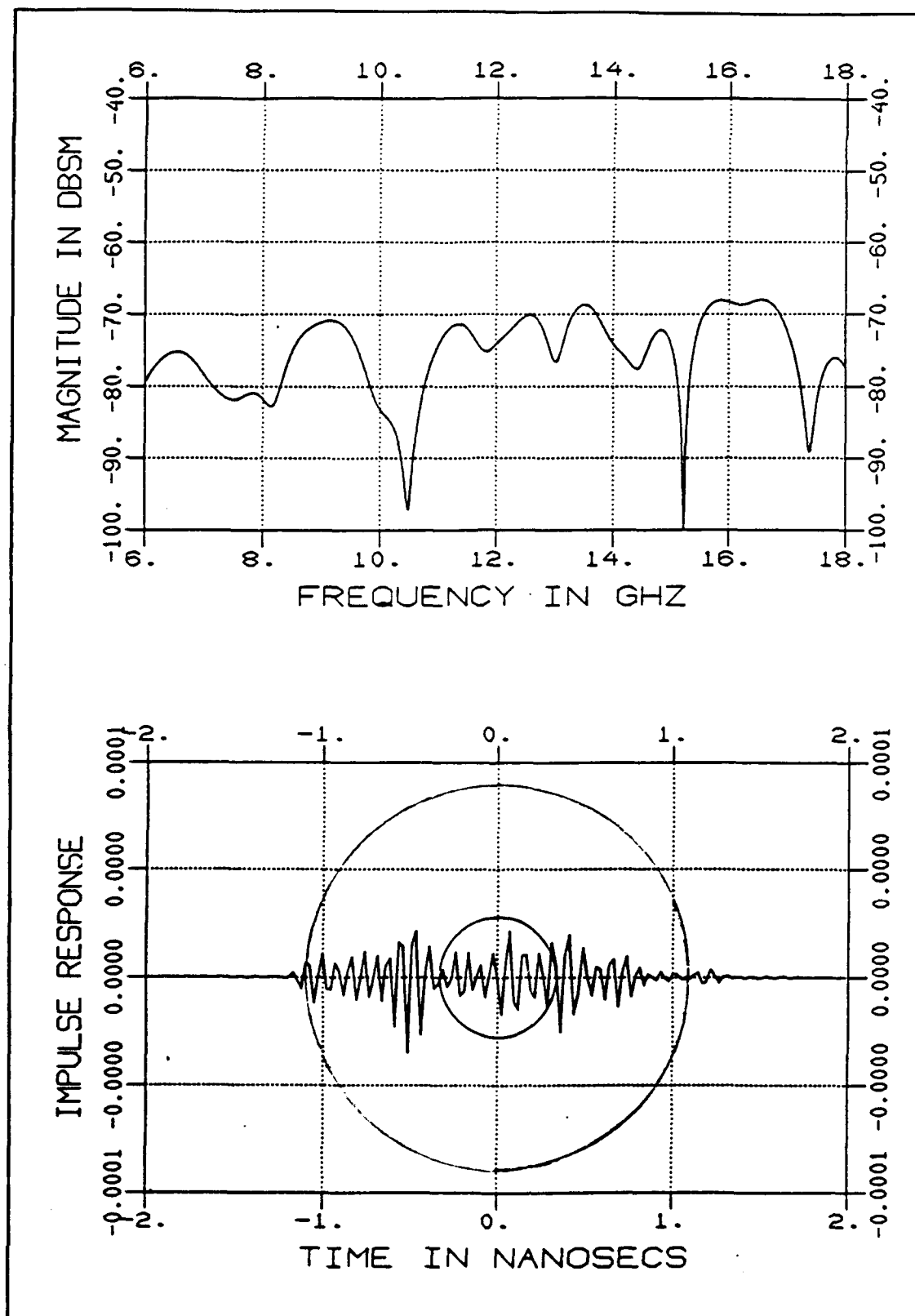


Figure 4.9. Frequency/Impulse Response of the 30 Degree Sloped Cylinder, Vertical Polarization

Front Sector Azimuth Scans

When only a particular sector of a target must be measured, the support designer has more leeway in reducing the column RCS. Shapes which have a low RCS in a particular direction can be incorporated into the support column. RATSCAT had suggested using a wedge-ogive-wedge design for front sector scans [15]. This shape became one of three experimental columns. The top view of each is shown in Figure 4.10.

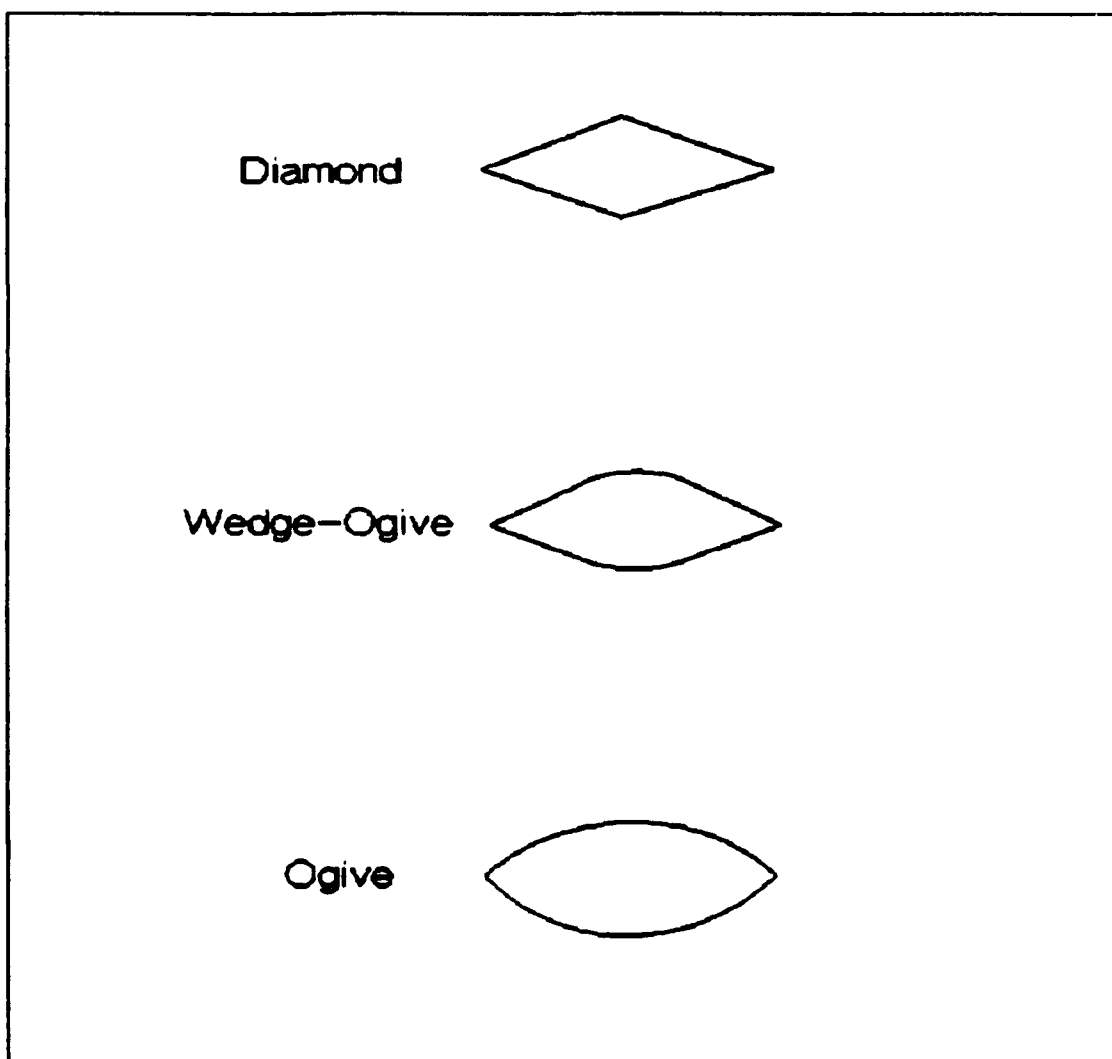


Figure 4.10. Top View of the Three Shaped Columns

To maintain consistency with the prior experiment, each column was made of one pound per cubic foot density EPS. Each was 8 inches in height, as were the sloped cylinders. The size of each was such that a 4 inch diameter circle could be inscribed into the top of each, to simulate the same minimum weight bearing capacity of the sloped cylinders. The angle of the wedge in each shape is about 21 degrees. This angle controls the location of the reflection from the sides. Sloping was not introduced at this stage, so that the differences caused by shaping alone could be isolated.

Limitation The goal of this thesis was to design columns that produce low radar cross sections. Ultimately, this same subject caused problems with the measurements. These shaped columns, as well as the sloped cylinders, have such low cross sections that the room and the supports used in the AFIT Chamber return more energy than the columns. These effects can not currently be negated for azimuth scans.

Azimuth Data The experiment began with an azimuth scan of each of the three columns. Each of the targets was measured at 10 GHz, with both horizontal and vertical polarization. Plots of vertical polarization are located in Appendix D. Plots of the azimuth scan of the Wedge-Ogive taken on separate days are shown in Figure 4.11. In the areas where the RCS is large, near broadside, the plots agree very well. This is not the case for the angles of interest.

The region of interest for these shapes is +/- 45 degrees off the tip. This sector is best seen on the plots between 135 and 225 degrees. In Figure 4.11, the Wedge-Ogive has a fairly constant RCS level of about -50 dBsm in this front sector in the top figure. However, the bottom

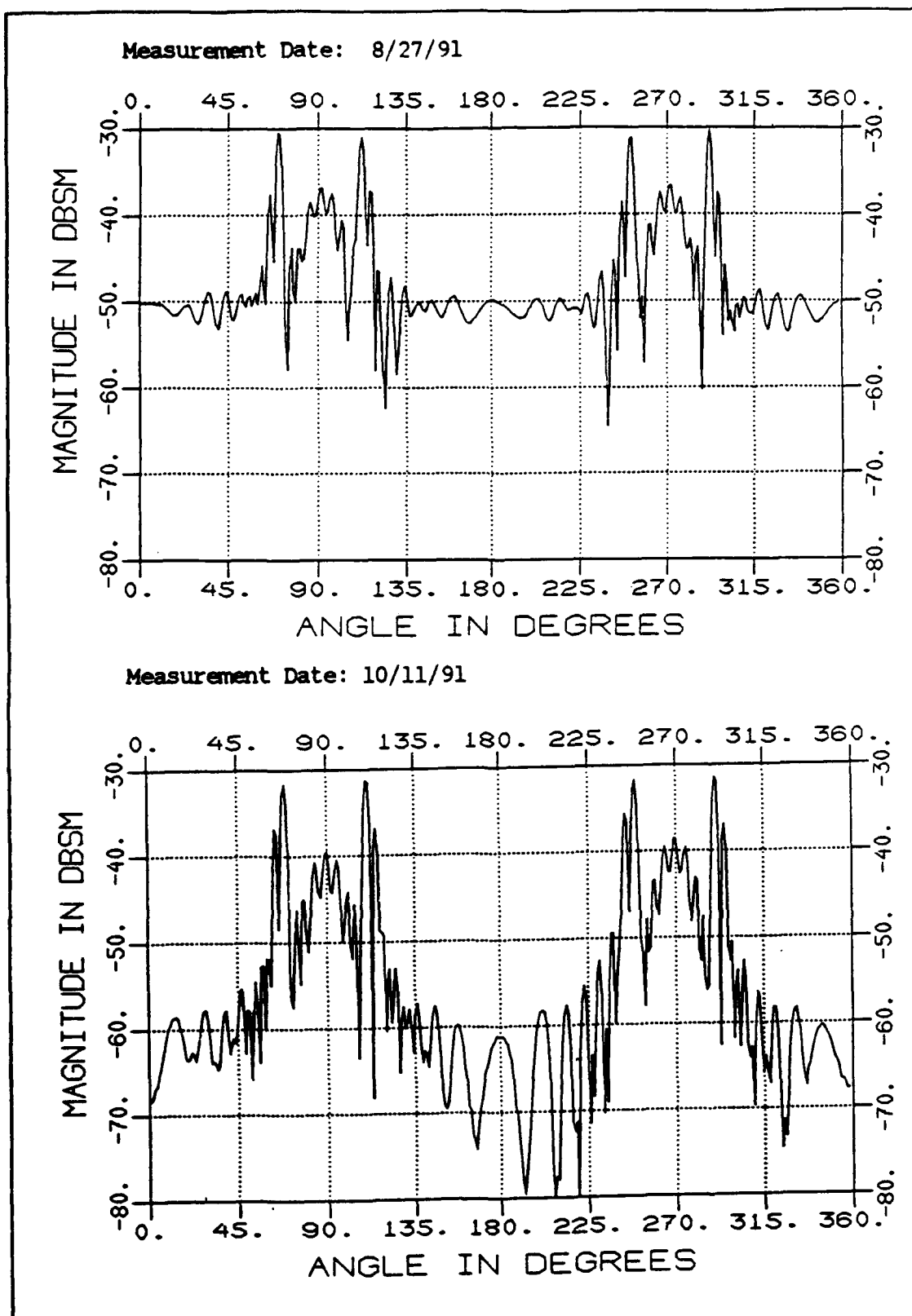


Figure 4.11. Azimuth Scan of Wedge-Ogive, Taken Different Days, Horizontal Polarization, $F = 10$ GHz

plot was made on a day where the noise floor was much lower. The problem is that neither plot can be considered accurate. In this low RCS front sector, the levels could still be lower than those shown in the bottom plot.

A similar set of data for the Ogive is shown in Figure 4.12. Again the higher levels match very well, but near the lower end there is no agreement between the two plots, although these are more similar than the two plots of Figure 4.11.

For completeness, an azimuth scan of the Diamond is presented in Figure 4.13. This plot was made on the same day as the top plot of Figures 4.11 and 4.12. Although the noise floor caused problems, some useful information can be gathered from these plots.

The peaks of each plot occurs near about 69 degrees off the tip, since 21 degrees was chosen for the wedge angle. This implies that the peaks could be moved closer to 90 degrees to widen the front sector if necessary. The Wedge-Ogive and the Ogive also peak at broadside, because of the curved face. The Diamond only peaks at the reflections from the flat faces.

The important information is that each of these shapes provide very low RCS in the area of interest. Each shape was measured below -55 dBsm in the front sector, although how much lower cannot be assessed from the azimuth scans.

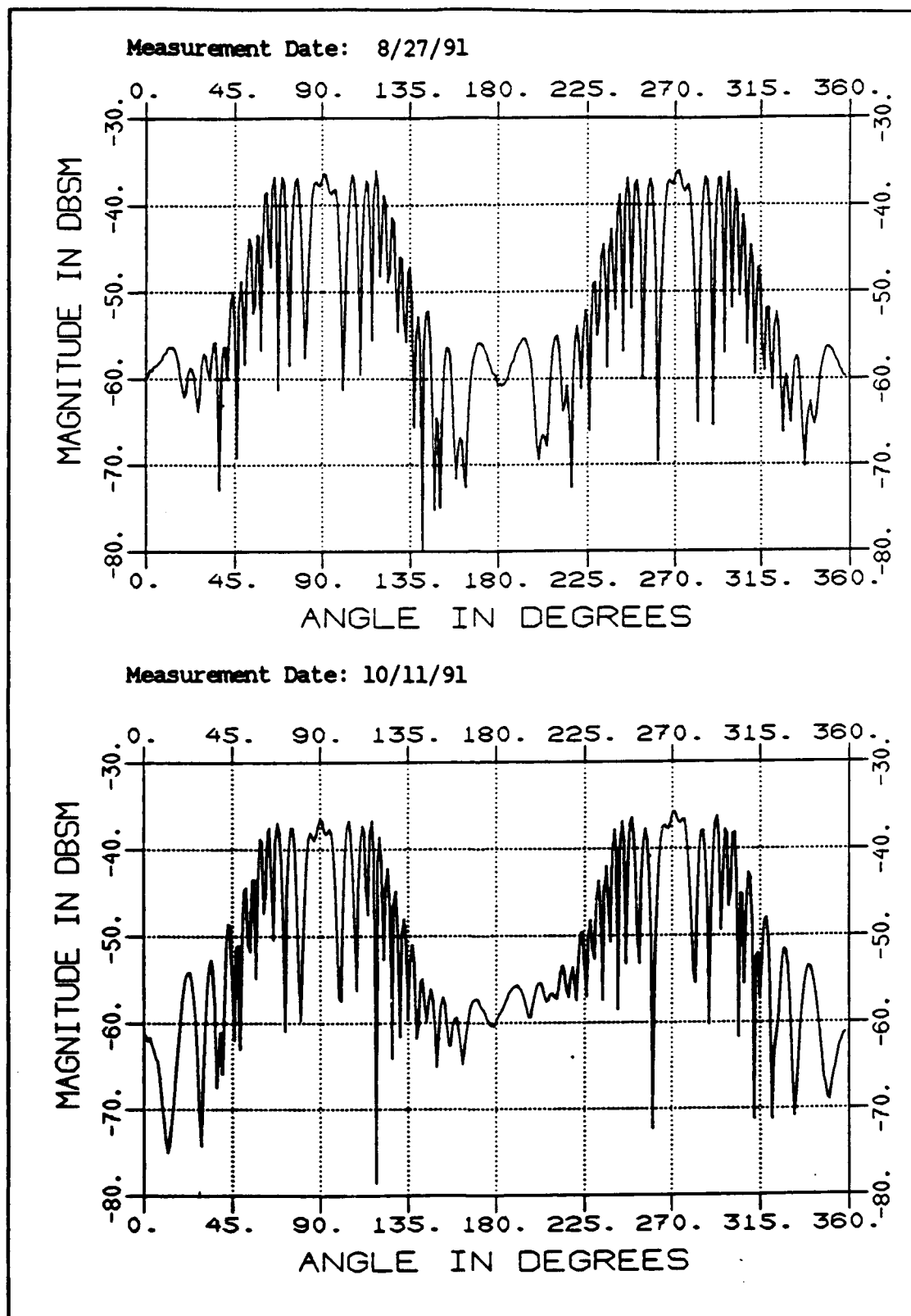


Figure 4.12. Azimuth Scan of Ogive, Taken Different Days, Horizontal Polarization, $F = 10$ GHz

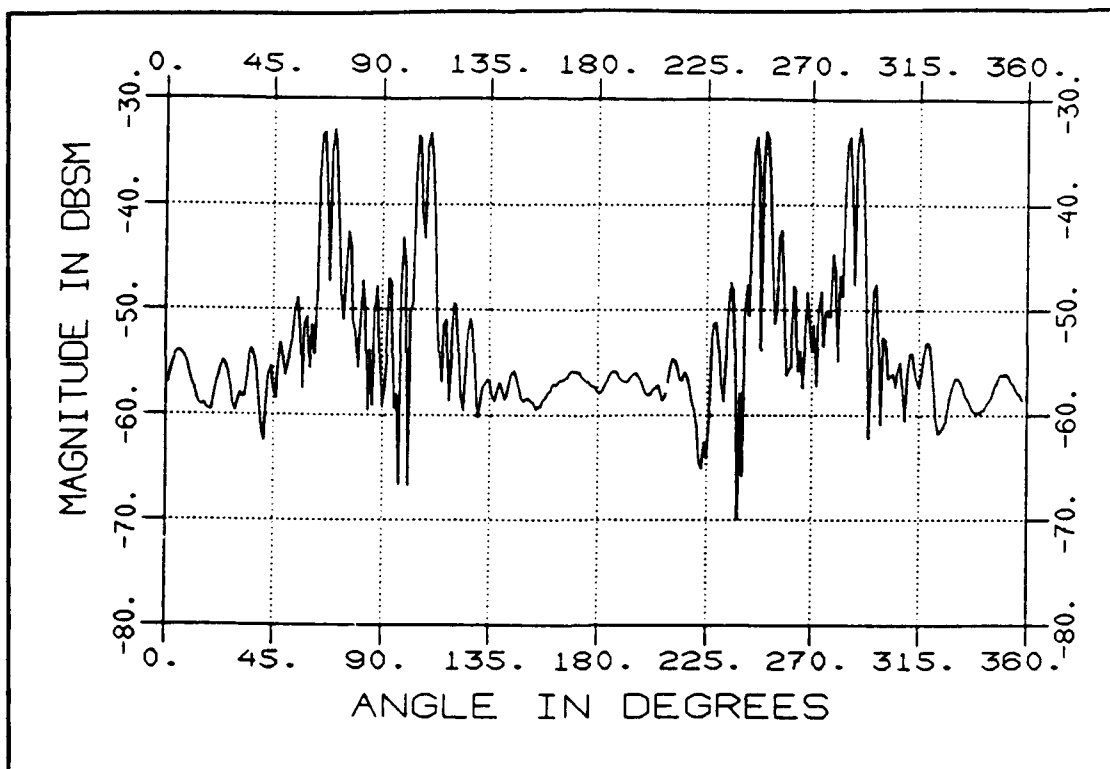


Figure 4.13. Azimuth Scan of Diamond, Horizontal Pol, $F = 10$ GHz

Frequency Data Azimuth scans are useful in visualizing the shape of the plot. However, the AFIT Chamber has the capability to post-process data taken with frequency scans. As mentioned, frequency data is transformed to the time domain. A time gate is used to eliminate returns that are not associated with the target, such as diffractions from the absorber on the rear wall. The "clean" data is then transformed back to the frequency domain.

Frequency scans of the shaped columns were made for tip-on and 45 degrees off the tip. These angles show the areas in the front sector where the comparative minimum and maximum RCS occurs.

Figure 4.14 shows the frequency/impulse response for the Wedge-Ogive, where one of the tips is facing the radar. A scaled outline of

the column is overlaid on the impulse response. This shows that the two largest contributors to the scattering are the front and back tips. This same fact can be seen in Figure 4.15, where the column has been rotated by 45 degrees.

In the tip-on plot, the RCS as shown in the frequency plot is extremely low across the entire band. Note that at 10 GHz, the frequency of the azimuth scans, the RCS is about -73 dBsm. The azimuth scan did not measure this low level, confirming the fact that the noise affected the azimuth measurement. The plots for the Ogive and Diamond at the two angles are presented in Figures 4.16 through 4.19. A comparison of the data shows that over most of the frequency band, the Wedge-Ogive maintains the lowest overall RCS. The Wedge-Ogive stays below -65 dBsm at all frequencies for both angles. The Diamond is at or below -60 dBsm, and the Ogive is generally around -58 dBsm.

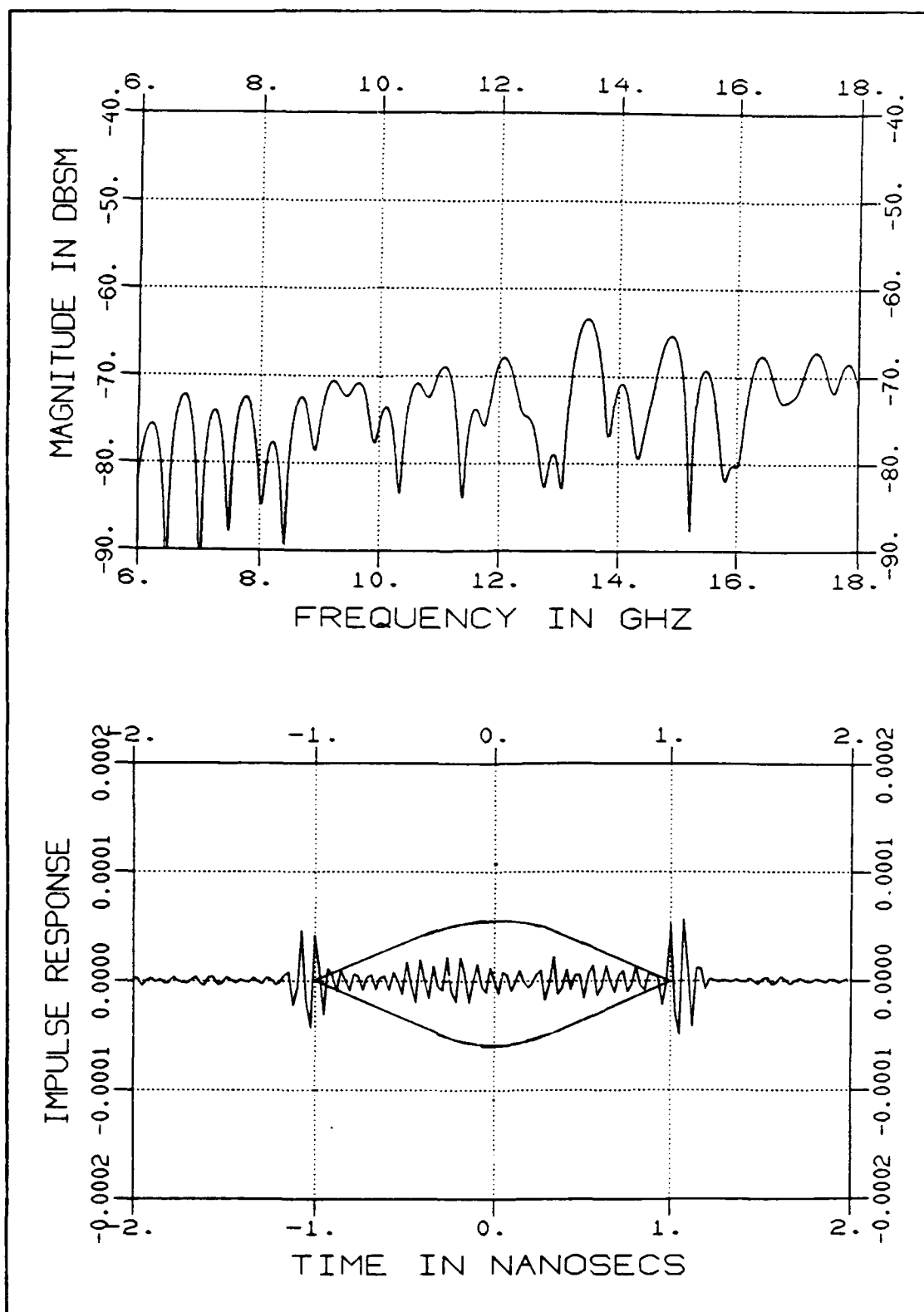


Figure 4.14. Frequency/Impulse Response of the Wedge-Ogive, Tip-On, Horizontal Polarization

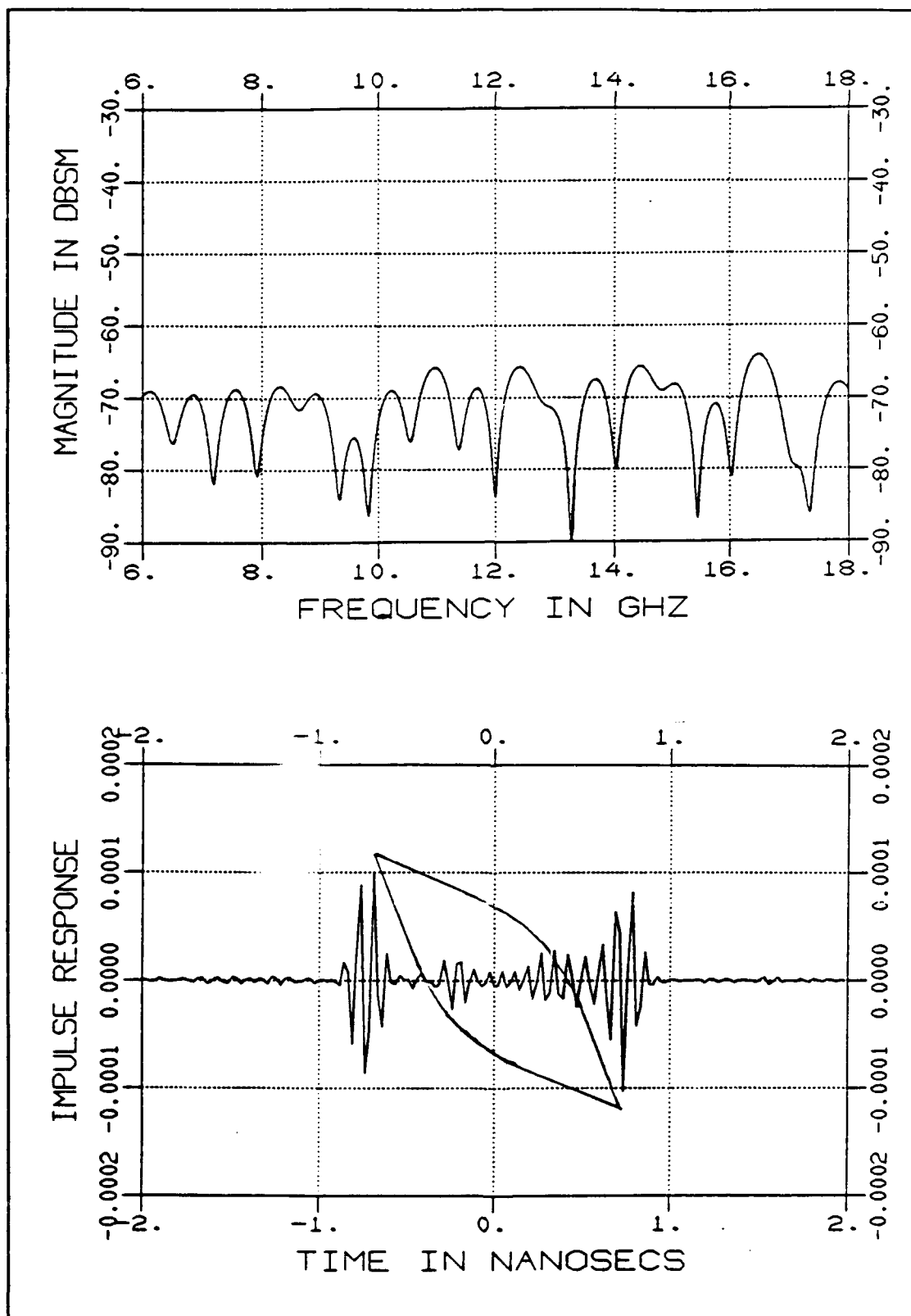


Figure 4.15. Frequency/Impulse Response of Wedge-Ogive, 45° off Tip, Horizontal Polarization

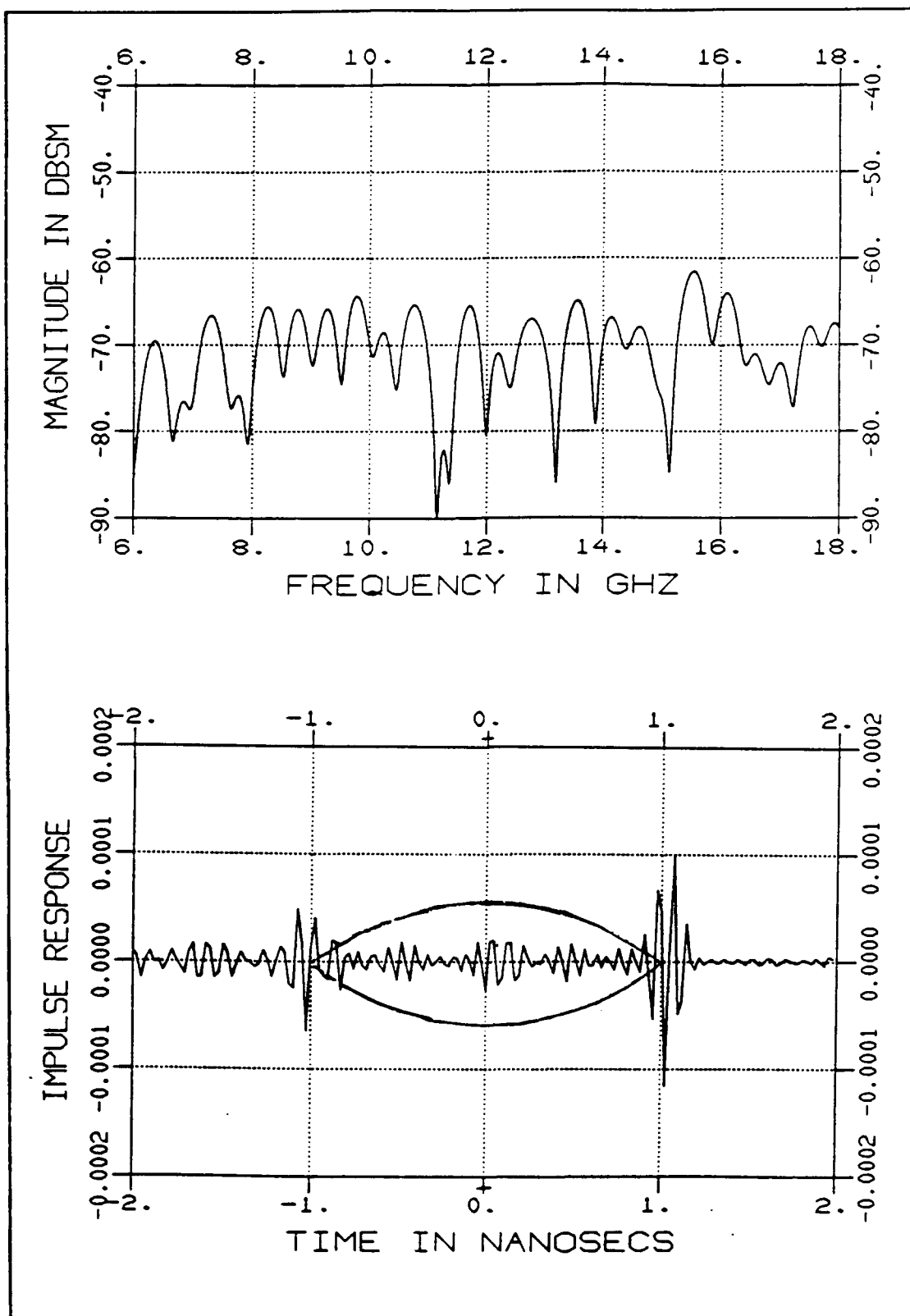


Figure 4.16. Frequency/Impulse Response of the Ogive, Tip-On, Horizontal Polarization

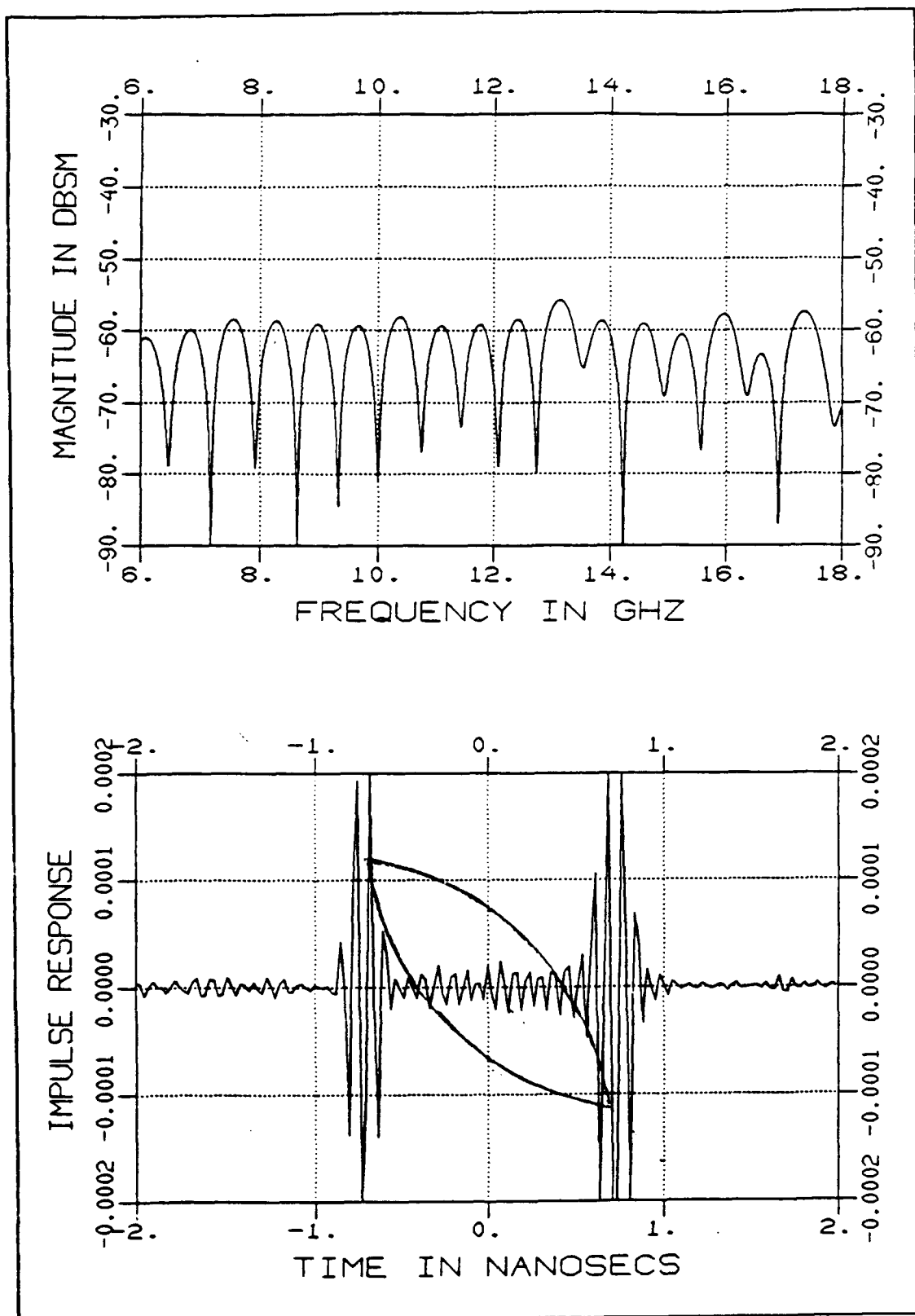


Figure 4.17. Frequency/Impulse Response of the Ogive, 45° off Tip, Horizontal Polarization

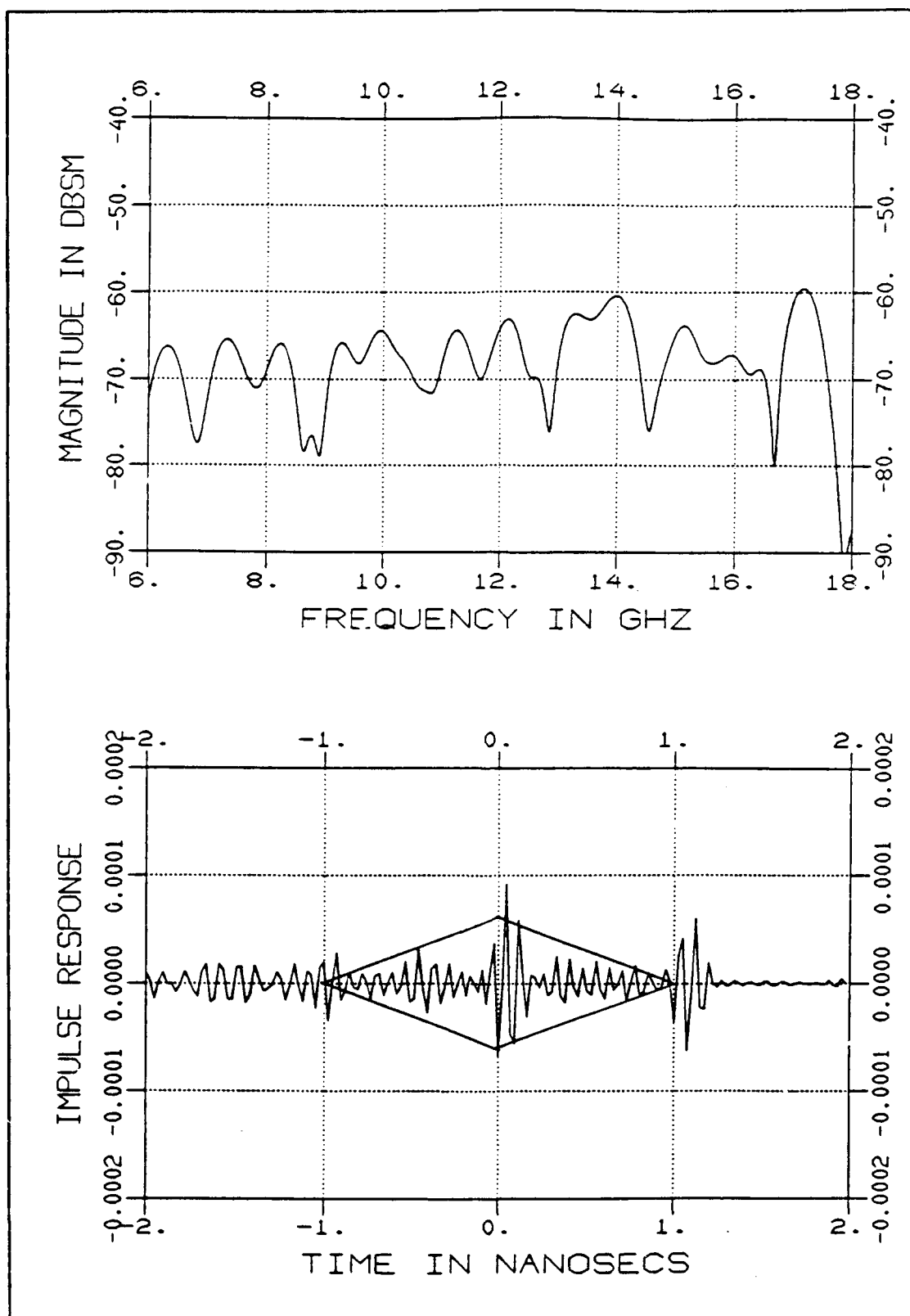


Figure 4.18. Frequency/Impulse Response of the Diamond, Tip-On, Horizontal Polarization

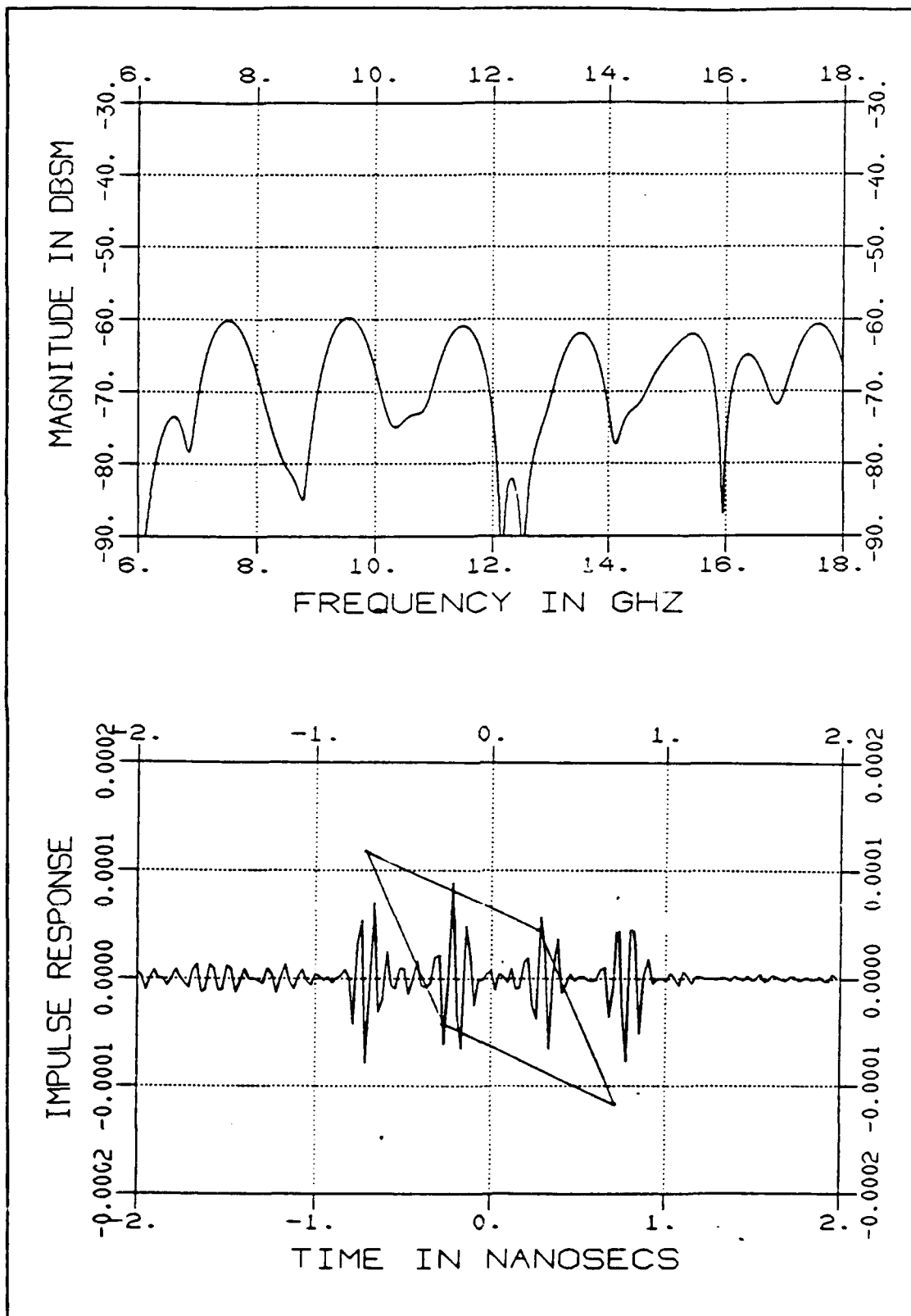


Figure 4.19. Frequency/Impulse Response of the Diamond, 45° off Tip, Horizontal Polarization

Sloped Cylinders The low front sector RCS of these shapes is impressive, but they should be compared against the frequency scans of the sloped cylinders. The measurement of the 20 degree sloped cylinder is shown again in Figure 4.20. When compared against the special shapes, the cylinder proves to be lower than the tip-on RCS for all three shapes.

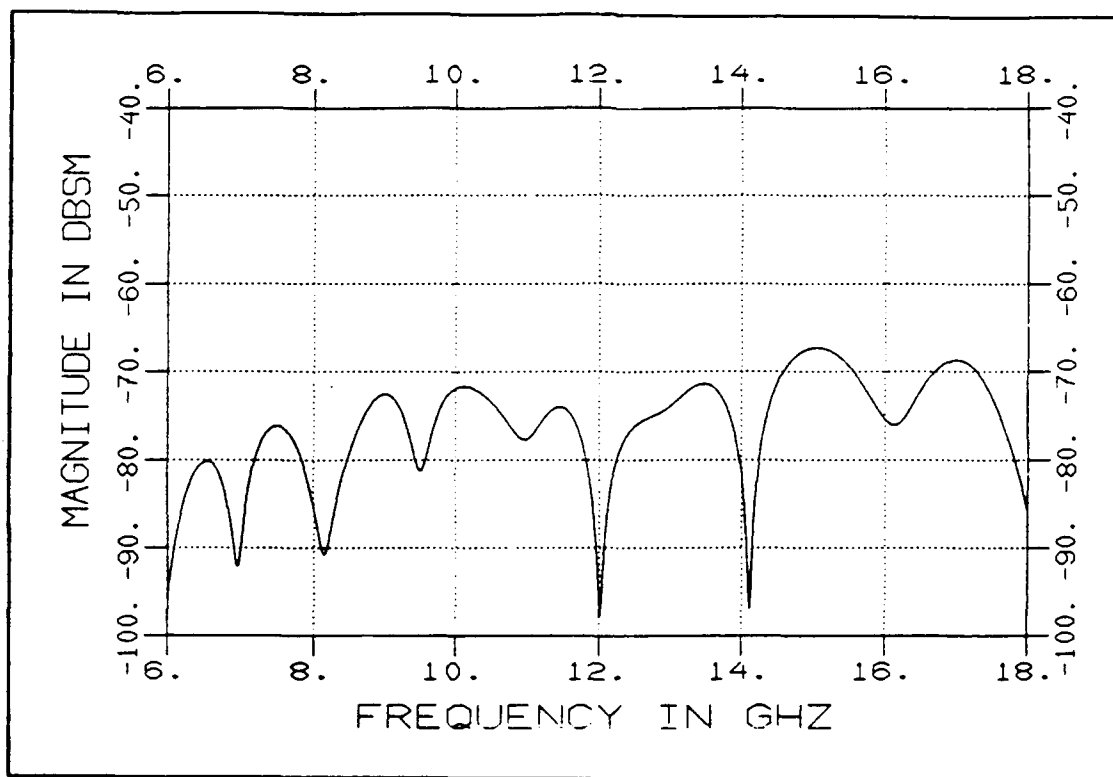


Figure 4.20. Frequency Response of the 20 Degree Sloped Cylinder, Horizontal Polarization

Considering the effectiveness of sloping the cylinders, the next item of study was the effect of sloping on the special shapes. The Diamond was chosen, and a new column was constructed with 10 degrees of slope. The top of the diamond was kept the same size as the original.

Again the first measurement was an azimuth scan, and as with previous measurements, the noise floor hid the actual RCS in the front

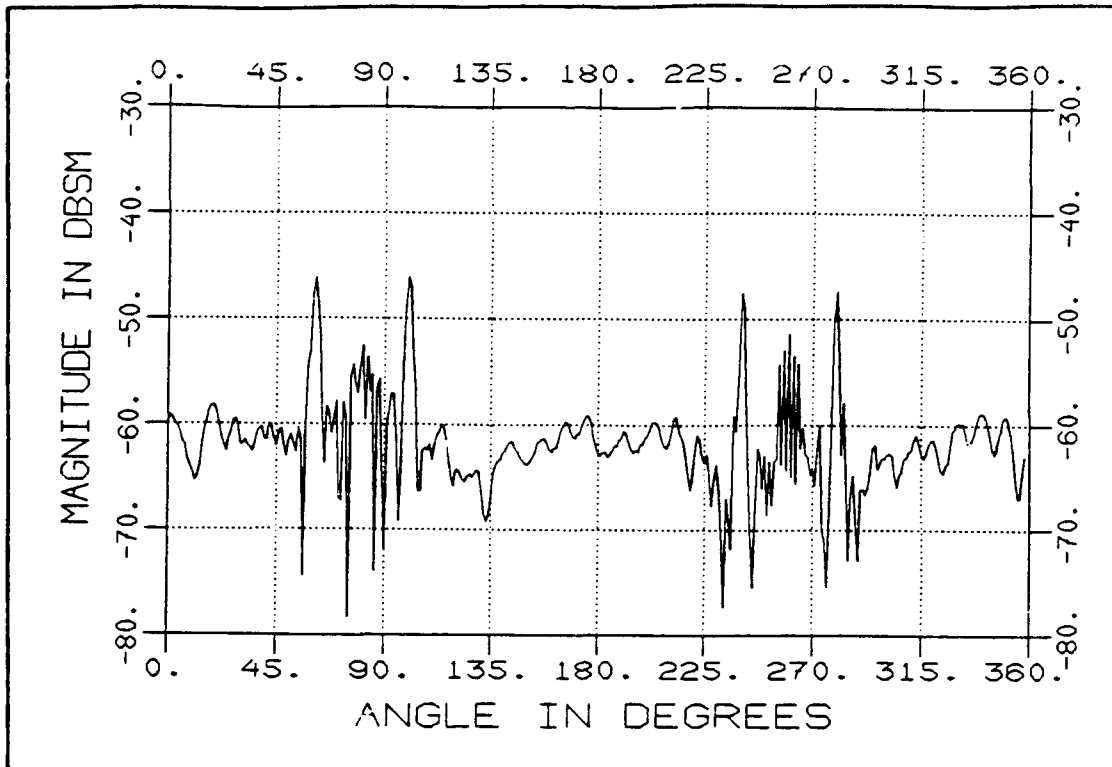


Figure 4.21. Azimuth Scan of Sloped Diamond, V-Pol, $F = 10$ GHz

sector. The plot is shown in Figure 4.21. The frequency was 10 GHz, and the polarization was vertical. The RCS in the angles near broadside has been greatly reduced over the Diamond.

A frequency response plot is given in Figure 4.22 for the case where the tip is pointing toward the radar. The plot shows that the RCS as a function of angle for the Sloped Diamond is no better than that of the Diamond, and is certainly higher than the sloped cylinder. Time domain plots measured at different incident angles are displayed in Appendix E. The time domain plots show that the return from the sloped vertical edges of the Sloped Diamond are nearly the same strength as those from the vertical edges of the Diamond, therefore the same RCS (away from the reflection from the faces of the Diamond).

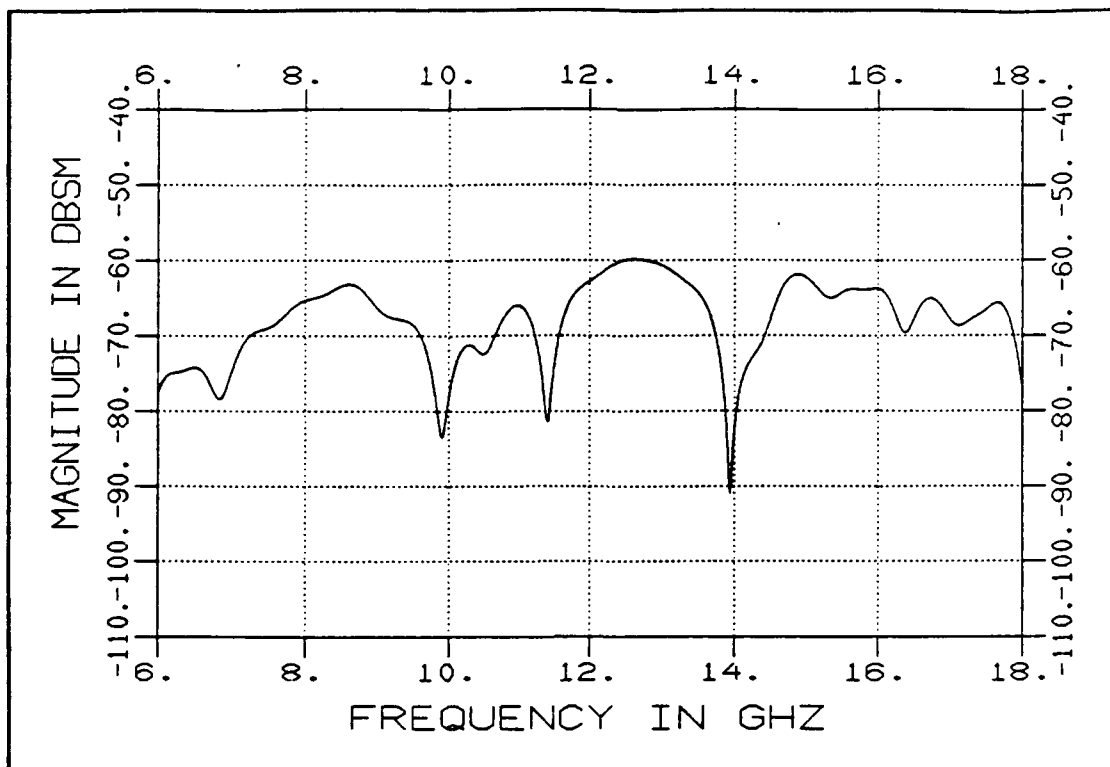


Figure 4.22. Frequency Response of the Sloped Diamond, H-Pol

Incoherent Scattering

According to [5], the incoherent RCS from a 110 cubic inch (approximately) Pelaspan ogive was -70.2 dBsm. This implies that the incoherent RCS is about -58.2 dBsm per cubic foot. Eq. (2.4), from [2], predicts the incoherent RCS at about -57 dBsm per cubic foot of styrofoam at 10 GHz. Eq. (2.8), which modifies Eq. (2.4) for EPS predicts the incoherent RCS at about -45 dBsm per cubic foot at 10 GHz.

The special shapes, the Diamond, Ogive and Wedge-Ogive are all approximately 300 cubic inches, or .174 cubic feet. Scaling the above predictions indicates that the incoherent RCS should be at either -65.8 dBsm, -64.6 dBsm or -52.6 dBsm respectively at 10 GHz. Theoretically, the incoherent scattering sets the "minimum" RCS. However, as can be

seen in the frequency domain plots (Figure 4.14, 4.17, 4.19), the RCS goes well below -70 dBsm near 10 GHz for all three shapes.

The Sloped Diamond is physically larger than the other three shapes, but as seen in Figure 4.22, its RCS near 10 GHz is about -80 dBsm. The 30 degree sloped cylinder is nearly a cubic foot in volume, but measurements (Figure 4.9) show levels below -80 dBsm near 10 GHz. This data indicates that the incoherent scattering is below the accepted predicted levels.

Prediction Model

One other set of measurements were required for this project. In the course of deriving the prediction model, some knowledge of the main scattering mechanisms for the partial cylinder was required. Figure 4.23 shows two of the time domain plots made in the study.

The two plots consider the incidence angles $\theta = 0^\circ$ (top) and $\theta = 60^\circ$ (bottom). At $\theta = 0^\circ$, the flat surface looks like a flat plate, hence the strong return. The diffraction terms associated with the reflection shadow boundaries are responsible for most of the scattering for normal incidence on a flat plate. The reflection from the front convex surface is a fairly strong term also.

At $\theta = 60^\circ$, the incidence angle is at the reference angle ψ , so the reflection from the convex surface has ceased. The diffractions from the forward corner must smooth out the scattering void left by loss of the reflection term. The strength of the diffraction is nearly as strong as the one seen for the reflection at $\theta = 0^\circ$. Since the curved surface is nearly perpendicular to the incident rays, the diffraction can be associated with the RSB from this corner.

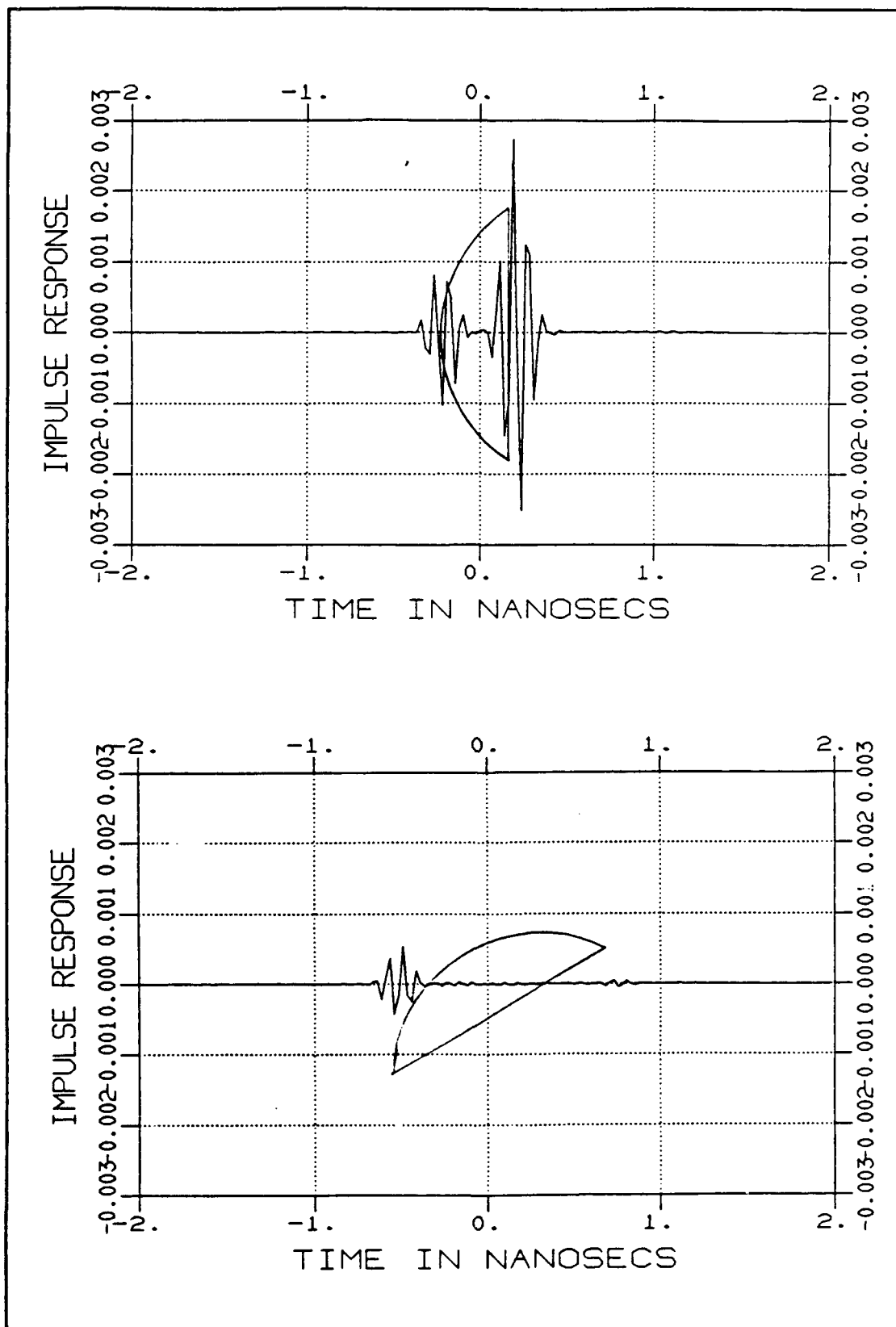


Figure 4.23. Impulse Response of the Partial Cylinder, H-Pol

Appendix F shows the series of measurements made, with a brief description of the scattering. The results of the measurements were that the total scattered field can be attributed to the reflections from the curved surface and the diffraction terms associated with the reflection shadow boundaries.

V. Conclusions and Recommendations

Summary

This thesis investigated the scattering from foamed plastic target supports. In particular, two areas were studied. The first involved the derivation of an RCS prediction model for a given two dimensional column. The second area was the design and measurement of low RCS foamed plastic support columns.

The derivation used a modified version of the Uniform Theory of Diffraction to calculate the backscatter from a expanded bead polystyrene column. This prediction model summed the various scattering contributions from the target. The contributions arose from reflections from curved dielectric surfaces and diffractions from curved and flat dielectric edges. Each term was scaled by combinations of reflection and transmission coefficients which partially determined its relative strength. The RCS model accurately predicted the RCS from two variations of the selected target at both horizontal and vertical polarization.

The design and measurement area examined the effects of shaping on the coherent return from foamed plastic target supports. Sloping was introduced on a right circular cylinder to drastically reduce its RCS. Other columns were measured with the intent of finding a shape that would produce a very low RCS over a 90 degree sector. Two shaped columns were identified which returned only -70 dBsm across most of the frequency band from 6 to 18 Gigahertz.

Conclusions

The conclusions found in the process of this research are:

1. The formulas often used to calculate the incoherent scattering from polystyrene based materials do not correctly predict the levels of the backscattered signal. No incoherent effects were noted during the measurements of the various EPS targets. That is, none exceeded the noise floor of the AFIT RCS Chamber. Several targets with a predicted incoherent RCS of -65 dBsm measured well below -80 dBsm.

One particular assumption that is made for these formulas is that the scattering of the individual particles are independent of nearby particles. For this assumption to hold, spherical scattering particles must be separated by at least 3 times their diameter [2]. However, with expanded bead polystyrene, the beads are very tightly packed, and this requirement is not met.

2. The Uniform Theory of Diffraction is a very accurate tool for calculating the backscatter from foamed plastic two dimensional targets. Often, physical optics or surface integrals are used to predict the RCS of support columns [2] [15]. These techniques can be quite cumbersome, and UTD is a relatively simple alternative method for achieving accurate RCS predictions.

3. Shaping is critical in the design of foamed plastic target supports. Although the reflection coefficient is very low, around .004, presenting a flat surface to the receive antenna results in a large RCS. Sloping the outer surfaces of cylindrical columns reduced their RCS by up to 25 dBsm.

4. Low RCS shapes such as wedges and ogives can be used in designing low RCS columns. This study measured three shaped two dimensional columns, which were less than -60 dBsm or less across the frequency band from 6 - 18 GHz in a 90 degree sector of angles. Even though the RCS was low, the RCS from the sloped circular cylinders was even lower, at nearly -70 dBsm. Additionally, the sloped cylinders have the advantage of being useful at all incidence angles.

Recommendations

This project introduced an effective means to calculate the RCS of foamed plastic target supports and showed that simple shaping can drastically reduce the RCS of the commonly used cylindrical target support. Further research could follow several avenues.

First, the UTD method could be used to predict the RCS of other two dimensional columns. Since the noise floor of the AFIT Chamber inhibited measurements of the shaped columns, predictions could be accomplished on these columns to determine how low the RCS is in the front sector.

Second, the AFIT Chamber is being upgraded with a hardware gating device and a new transmit amplifier. These additions should lower the noise floor, allowing for better low RCS measurements. If so, further measurements could be done on combinations of sloping and shaping. This would include measurements to determine which slope angle provides the minimum return, for both cylinders and shaped columns.

Finally, the issue of incoherent scattering should be addressed in more detail. RATSCAT engineers claim that the incoherent scattering is a problem when the physical size of the target support is large [15].

Since large target supports can not be measured in the laboratory, perhaps RATSCAT could provide range time for further research to measure large columns with low coherent RCS shapes. In addition, the incoherent scattering model could be modified to account for the effects of particles whose scattering is dependent on neighboring particles.

APPENDIX A

Fortran Prediction Code

This appendix lists the fortran code that was used to generate the RCS of the partial cylinder. This program was compiled and run on the AFIT VAX computer.

```

*                               Thesis Project
*                               RCS From a Partial Circular Cylinder
*
*****
* Fortran program (cyl.for) to calculate RCS of partial      *
* cylinder. This program works for either horizontal (hard)  *
* polarization or vertical (soft) polarization. For hard,    *
* set the variable polz to 1; for soft, set the variable     *
* polz to -1.                                                *
*****

* Define variable types for main program
  integer i,ii
  real a,d,pi,lambd,k,n, R, psi, rho, rhop, air, sty
  real rho1,rho2,phi1,phi2,theta(0:360),thetad(0:360)
  real L1,L2,Lro1, Lro2, Lro3, Lro4, polz, deg, freq
  real sigma(0:360), l, REF, TRN, zero, rca, rcs, tca, tcs

  complex j, UR, U1TI,U1TR, U2TI, U2TR, U1TC, U2TC1, U2TC2
  complex DSHI, DSHR, Utot(0:360)
  complex URP, U2BI,U2BR,U1BI,U1BR,U1BC1,U1BC2, U2BC
  complex phasel, phase2

* Variable Initialization: determined and filled in by user.

  air = 1.0006          ! Relative permittivity of air.
  sty = 1.021           ! Relative permittivity of styrofoam.
  polz = -1.            ! +1 for Hard -1 for soft.
  freq=10.*10.**9.      ! frequency determined by user.
  lambda=3.*10.**8./freq ! wavelength.
  a=5.0*.0254           ! Radius of cylinder in meters.
  d=8.625 *.0254        ! distance across the flat face in meters.
  R=10000. * lambda     ! Far field distance to source.
  l=.254                ! Length of cylinder in meters

* Set up constants.

  pi=3.141592654
  k=2.0*pi/lambda       ! wave number.
  j=(0.0,1.0)
  deg=180./pi           ! radian to degrees conversion factor.
  zero = 0.0

* Define some of the working variables.

  rho= R - a            ! Distance: Source to outer shell.
  rhop=R+a              ! Distance: Source to inner shell.
  psi= asin(d/(2.*a))   ! Angle from theta=0 to corner.
  gamma=pi/2. - psi     ! Angle of tangent line at corner.
  n=2                   ! needed for diffraction coefficient

```

```

*   Choose theta as index, increase by one degree increments.

      do 100 i=0,180
        thetad(i)=float(i)

*   Move angles slightly to avoid singularities at 180, 90, 0 degrees.

        if ( thetad(i) .eq. 180.) then
          thetad(i) = 179.8
        endif
        if ( thetad(i) .eq. 0.0) then
          thetad(i)=.2
        endif
        if ( thetad(i) .eq. 90.) then
          thetad(i) = 89.8
        endif

        theta(i)=thetad(i)/deg
        rho1=R-a*cos(psi-theta(i))      ! Distance: source to corner 1.

        rho2=R-a* sin(gamma - theta(i)) ! Distance: source to corner 2.

        phasel = cexp(-2. * j * k * rho1) ! 2-way phase shift.
        phase2 = cexp(-2. * j * k * rho2) ! 2-way phase shift.

*   The L terms are distances for the diffraction coefficients. L is
*   used for the straight edges, while Lro is used for the curved edges.

        L1 = rho1/2.      ! Corner 1.
        L2 = rho2/2.      ! Corner 2.
        Lro1=(rho1 * .5 * a) / (.5 * a + rho1) ! Convex corner 1.
        Lro2=(rho2 * .5 * a) / (.5 * a + rho2) ! Convex corner 2.
        Lro3=(rho2 * -.5 * a) / (-.5 * a + rho2) ! Concave corner 2.
        Lro4=(rho1 * -.5 * a) / (-.5 * a + rho1) ! Concave corner 1.

*   Solve for the reflection and transmission coefficients using
*   subroutines: functions of (incident angle, polz, epl, ep2).

        rca = REF(polz,air,sty) ! refl coef from air-sty
        tca = TRN(polz,air,sty) ! tran coef from air-sty
        rcs = REF(polz,sty,air) ! refl coef from sty-air
        tcs = TRN(polz,sty,air) ! tran coef from sty-air

*   Solve for the various mechanisms, which have been scaled the amount
*   of the singularity at its corresponding shadow boundary.
*   ULTI means top corner 1 ISB, etc.
*   DSHI and DSHR are subroutines to calculate the diffraction
*   coefficients due to the incident and reflection shadow boundaries.

        ULTI = phasel * (1.-(tca*tcs)) * DSHI(k,n,b3,L1)
        ULTR = phasel * (tca*rcs*tcs)* DSHR(polz,k,n,b3,L1)
        U2TI = phase2 * (1.-(tca*tcs)) * DSHI(k,n,b4,L2)

```



```

U2TR = phase2 * (tca*rca*tcs) * DSHR(polz,k,n,b4,L2)
U1TC = phase1 * (rca) * DSHR(polz,k,n,b5,Lro1)
U2TC1 = phase2 * (rca) * DSHR(polz,k,n,b6,Lro2)
U2TC2 = phase2 * (tca*rca*tcs)*DSHR(polz,k,n,b6,Lro3)
UR=(cexp(-2. *j*k*rho))*sqrt((rho*a/2.)/((a/2.)+rho))*rca

```

* Continue steps for theta > 90.

```

U1BR = phase1 * rca *DSHR(polz,k,n,c4,L1)
U1BI = phase1 * (1.-(tca*tcs)) * DSHI(k,n,c4,L1)
U2BR = phase2 * rca *DSHR(polz,k,n,c3,L2)
U2BI = phase2 * (1.-(tca*tcs)) * DSHI(k,n,c3,L2)
U1BC1 = phase1 * rca *DSHR(polz,k,n,c5,Lro1)
U1BC2 = phase1 * (tca*rca*tcs)*DSHR(polz,k,n,c7,Lro4)
U2BC = phase2 * (tca*rca*tcs)*DSHR(polz,k,n,c10,Lro3)
URP= (cexp(-2.*j*k*rhop))*sqrt((rhop*a/2.)/((a/-2.)+rhop))
URP = URP*rca*tca*tcs*cexp(j*pi/2.)

```

* Sum up all the mechanisms needed for each angle.

```

if (theta(i) .lt. gamma) then
  Utot(i)=U1TI+U1TR + U2TI+U2TR + U1TC + U2TC1 + UR
elseif (theta(i) .lt. psi) then
  Utot(i)= U1TI+U1TR + U2TR + U1TC + U2TC2 + UR
elseif (theta(i) .le. pi/2.) then
  Utot(i)= U1TI+U1TR +U2TR + U1TC + U2TC2
elseif (theta(i) .lt. (pi/2.+gamma)) then
  Utot(i)=U1BR+ U2BI+U2BR + U1BC1 + U2BC
elseif (theta(i) .lt. (pi-gamma)) then
  Utot(i)=U1BR + U2BI+U2BR +U1BC1 + U2BC + URP
else
  Utot(i)=U1BI+U1BR + U2BI+U2BR + U1BC2 + U2BC + URP
endif

```

* Calculating RCS. Use approximation for 2D to 3D RCS.

```

sigma(i)=10.*alog10(2.*1*1/lambda*2.*pi*(cabs(Utot(i))))**2)

```

* Fill in from 180 to 360 by making symmetric.

```

ii=360-i
sigma(ii)=sigma(i)
thetad(ii)=360.-float(i)
theta(ii)=2*pi-float(i)/deg

```

100 continue

* Print out results. If radians needed, use theta(i)

```
do 200 i=0,360
  write(*,300)thetad(i), sigma(i)
300 format(3x,2(1p13.4))
200 continue
stop
end
```

* Function to calculate Reflection Coefficient

*

REAL FUNCTION REF(polz,ep1, ep2)

c Input: polz=-1 for electric line source, +1 for magnetic line source

c ep1= incident ep2= boundary

c Output: REF

c

c

real ep1, ep2, polz, templ

templ= sqrt ((ep2/ep1))

if (polz .eq. 1.) then

REF=(ep2/ep1 -templ)/(templ+ep2/ep1)

elseif (polz .eq. -1.) then

REF=(1.-templ) / (1.+templ)

endif

return

end

* Function to calculate Transmission coefficient

REAL FUNCTION TRN(polz,ep1,ep2)

real ep1, ep2, polz, R, REF

R = REF(polz,ep1,ep2)

TRN = 1. + R

* Function to calculate Diffraction Coefficient for ISB

COMPLEX FUNCTION DSHI(k,n,phi,L)

c This is the second term of the four term diffraction coefficient for
c wedges, written by Capt Joseph. Its been modified to work
c on the single diffr term... for the ISB.

c Input: L=(rho*rho_pr)/(rho+rho_pr) in terms of wavelength
c Output: Dshi

c
c

real pi, n, phi, phi_pr, L, k
real N_2, a_2
real kLa_2, cot_2
complex j, F_2

pi = 3.141592654
j = (0.,1.)
phi_pr = phi

N_2 = real(nint((-pi+(phi-phi_pr)) / (2.*pi*n)))

a_2 = 2. * (cos((2.*n*pi*N_2-(phi-phi_pr)) / 2.))**2

kLa_2 = k * L * a_2

call fctx(1, F_2, kLa_2)

cot_2 = 1. / (tan((pi-(phi-phi_pr)) / (2.*n)))

DSHI = -cexp(-j*pi/4.) / (2.*n*sqrt(k*2.*pi))* (cot_2*F_2)
return
end

c

* Function to calculate Diffraction Coefficient for RSB

COMPLEX FUNCTION DSHR(polz,k,n,phi,Lro)

c This is the fourth term of the four term diffraction coefficient, for
c wedges, written by Capt Joseph. Its been modified to work
c on the single diffraction term...RSB of a curved edge. By
c adding Lro for the curved face.

c Input: polz=-1 for electric line source, +1 for magnetic line source
c Output: Dshr

c
c

real pi, n, phi, phi_pr, L, polz,k,Lro
real N_4, a_4
real kLa_4, cot_4
complex j, F_4

```

pi = 3.141592654
j = (0.,1.)
phi_pr = phi

N_4 = real( nint( (-pi+(phi+phi_pr)) / (2.*pi*n) ) )

a_4 = 2. * (cos( (2.*n*pi*N_4-(phi+phi_pr)) / 2. ) )**2

kLa_4 = k * Lro * a_4

call fctx(1, F_4, kLa_4)

cot_4 = 1. / (tan( (pi-(phi+phi_pr)) / (2.*n) ))

DSHR = -cexp( -j*pi/4. ) / (2.*n*sqrt(k*2.*pi))*cot_4*F_4
return
end

```

c This subroutine, also written by Capt Joseph, is used by the
c diffraction coefficient functions to calculate to fresnel integral.

```

subroutine fctx(id,fct,x)
complex fxx(8),fx(8),cj,fct
dimension xx(8)
data pi,tpi,sml/3.14159265,6.28318531,0.001/
data xx/.3,.5,.7,1.,1.5,2.3,4.,5.5/
data cj/(0.,1.)/
data fx/(0.5729,0.2677),(0.6768,0.2682),(0.7439,0.2549),
+(0.8095,0.2322),(0.873,0.1982),(0.9240,0.1577),(0.9658,0.1073),
+(0.9797,0.0828)/
data fxx/(0.,0.),(0.5195,0.0025),(0.3355,-0.0665),
+(0.2187,-0.0757),(0.127,-0.068),(0.0638,-0.0506),
+(0.0246,-0.0296),(0.0093,-0.0163)/

if (x.lt.0.0) k=-1
x=abs(x)
if(x.gt.5.5)go to 1
if(x.gt.0.3)go to 10
fct=((1.253,1.253)*sqrt(x)-(0.,2.)*x-0.6667*x*x)*cexp(cj*x)
c   if(id.eq.2) fct=2.*cj*x*(1.,-fct)
return
10 do 11 n=2,7
11 if(x.lt.xx(n))go to 12
12 fct=fxx(n)*(x-xx(n))+fx(n)
c   if(id.eq.2) fct=2.*cj*x*(1.,-fct)
return
1 if(id.eq.1) fct=1.+cmplx(-0.75/x,0.5)/x
if(id.eq.2) fct=1.+cmplx(-3.75/x,1.5)/x
if(k.eq.-1) fct=conj(fct)
return
end

```

APPENDIX B

Noise Floor Measurements of the AFIT RCS Chamber

This appendix contains noise floor measurements taken on various days. The plots are given to show the variations of the noise floor, and are for information only. For each measurement, each data point was averaged over 256 samples. In the azimuth scans, the data was taken every 1 degree. In the frequency scan, the data was taken every .01 GHz.

This plot shows a measurement of a low noise floor.
 The measured target was the empty room.
 The polarization was vertical. Freq = 7 GHz.

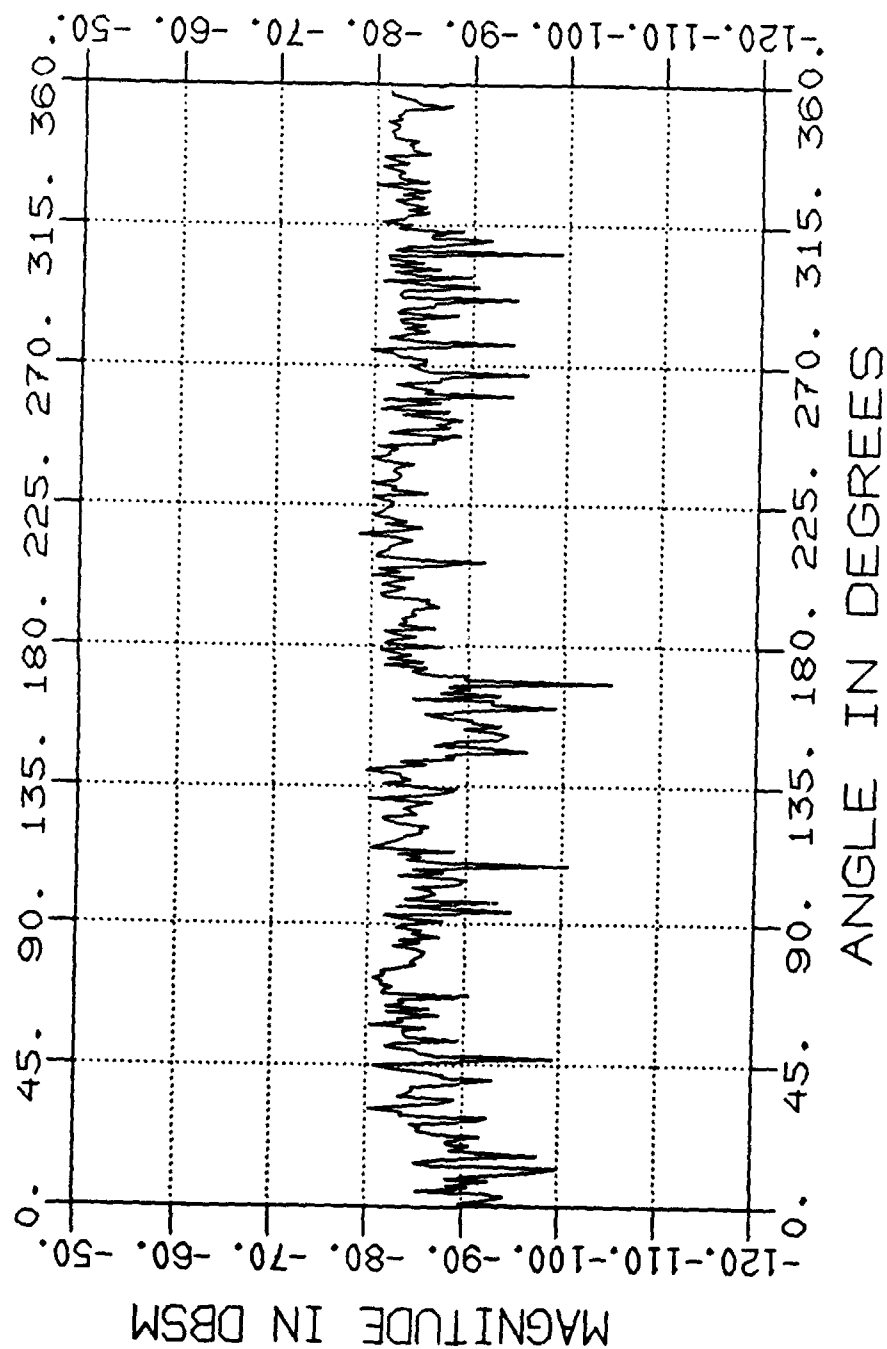


Figure B.1. Noise Floor Measurement, Azimuth Scan

This measurement included a 3 inch styrofoam mount, that serves as a target support. That is, the mount was included in both the background and target measurement. The polarization was vertical. Freq = 15 GHz.

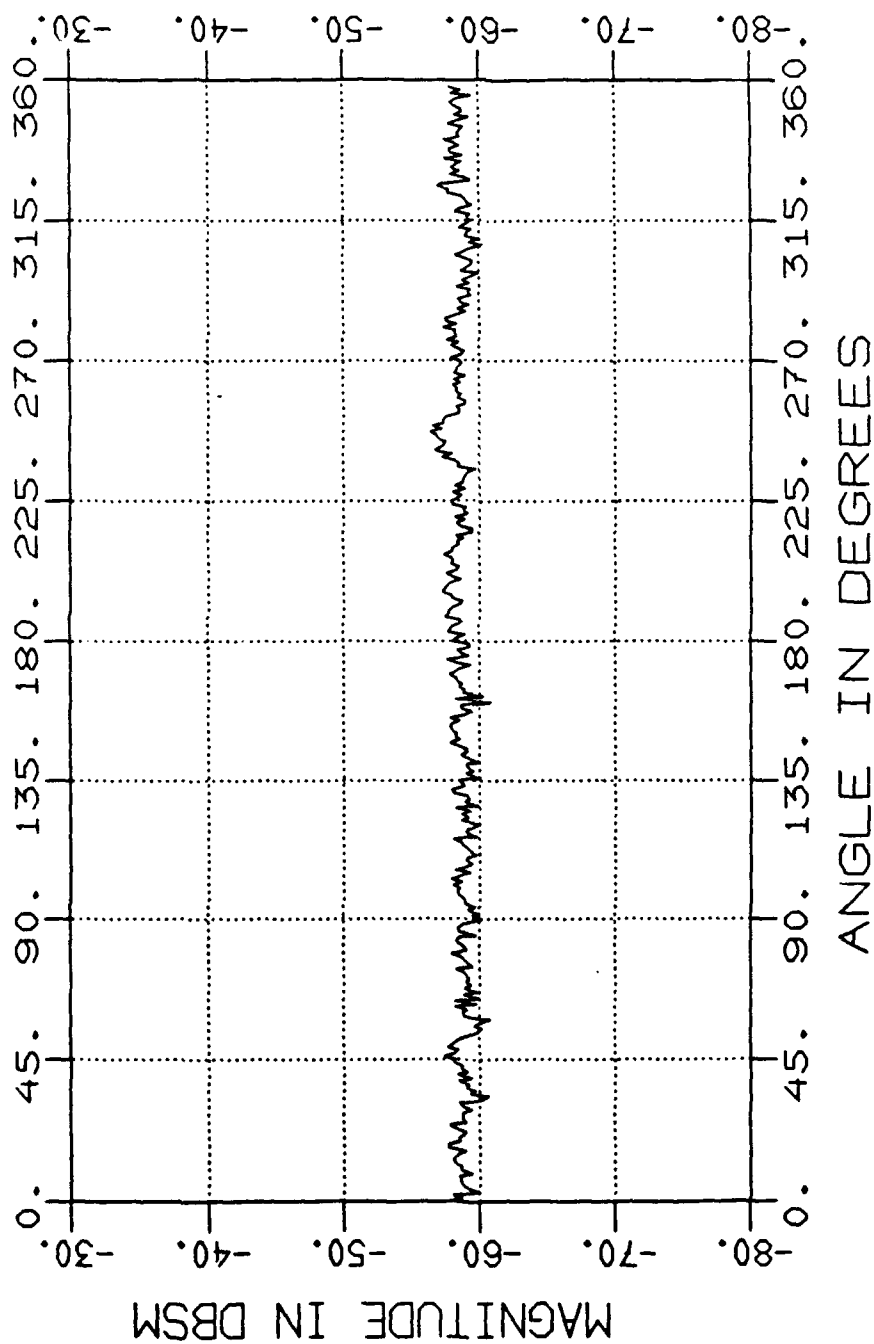


Figure B.2. Noise Floor Measurement, Azimuth Scan

This plot shows the noise floor of a frequency scan. Gating was not used in this case, however it commonly reduces the noise by 20 dB. The polarization was horizontal.

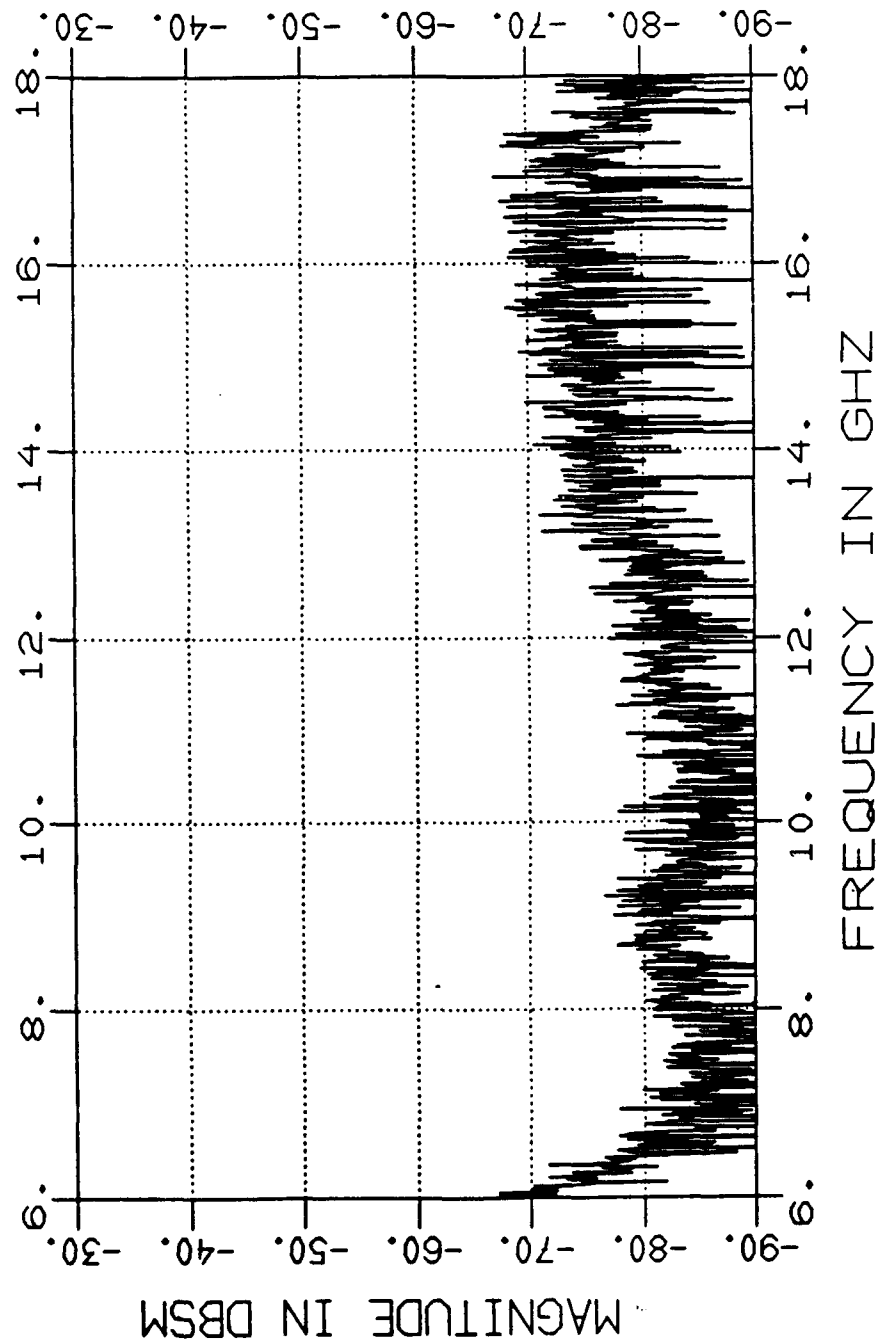


Figure B.3. Noise Floor Measurement, Frequency Scan

APPENDIX C

RCS Measurements of the Sloped Cylinders

This Appendix contains additional measurements for the various sloped cylinders discussed in Section IV.

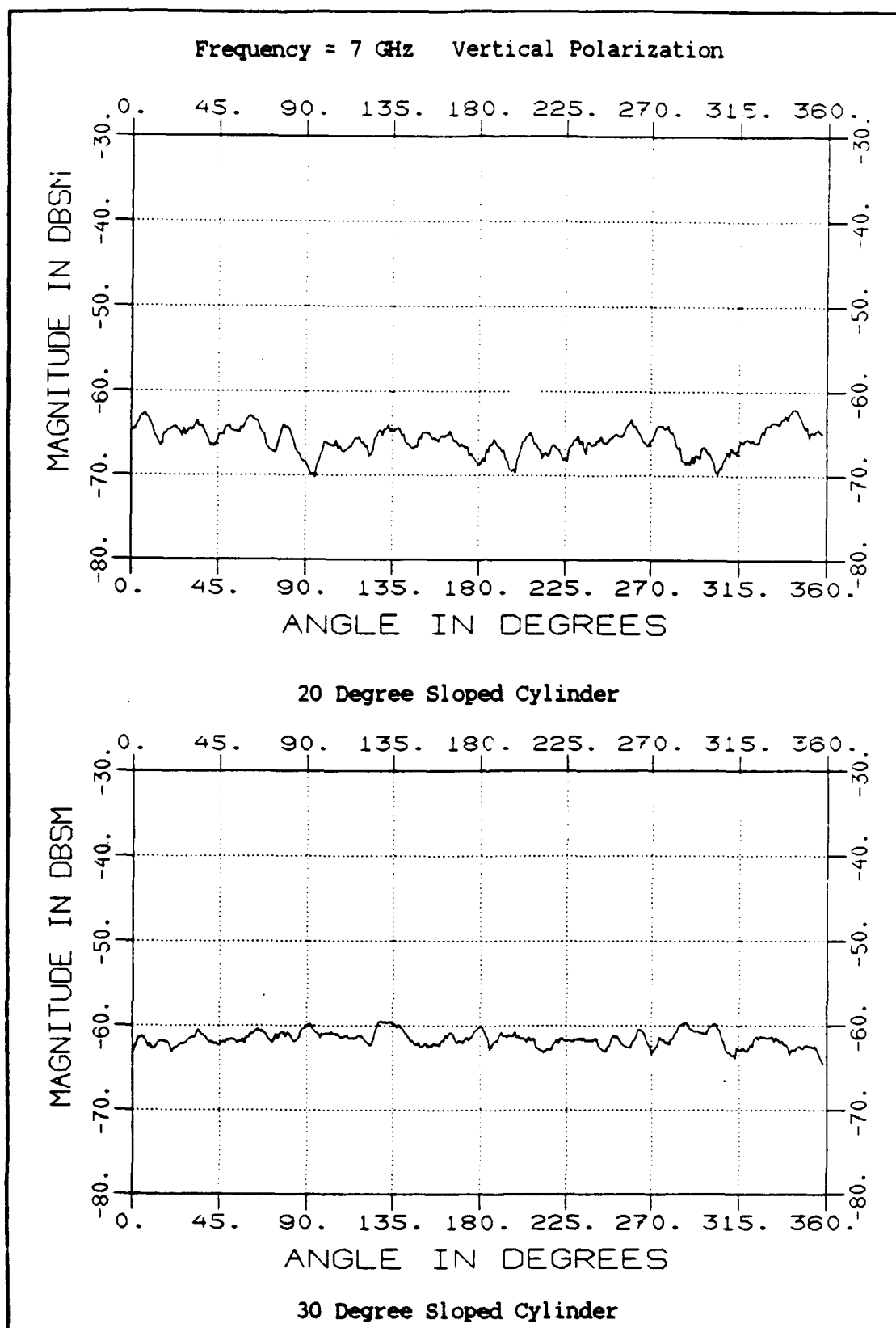


Figure C.1. Azimuth Scan of the 20° and 30° Sloped Cylinders

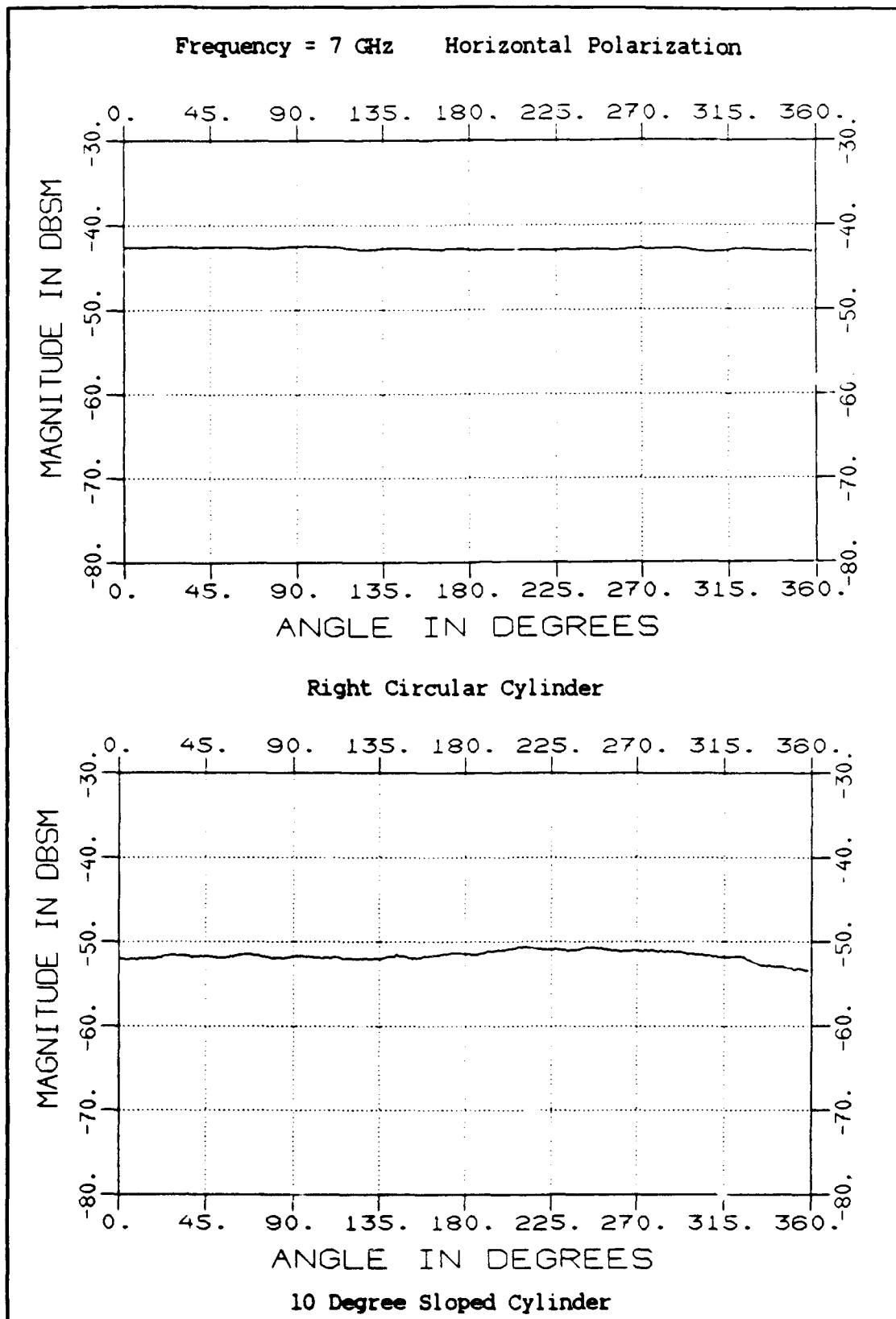


Figure C.2. Azimuth Scans of the RCC and the 10° Sloped Cylinder

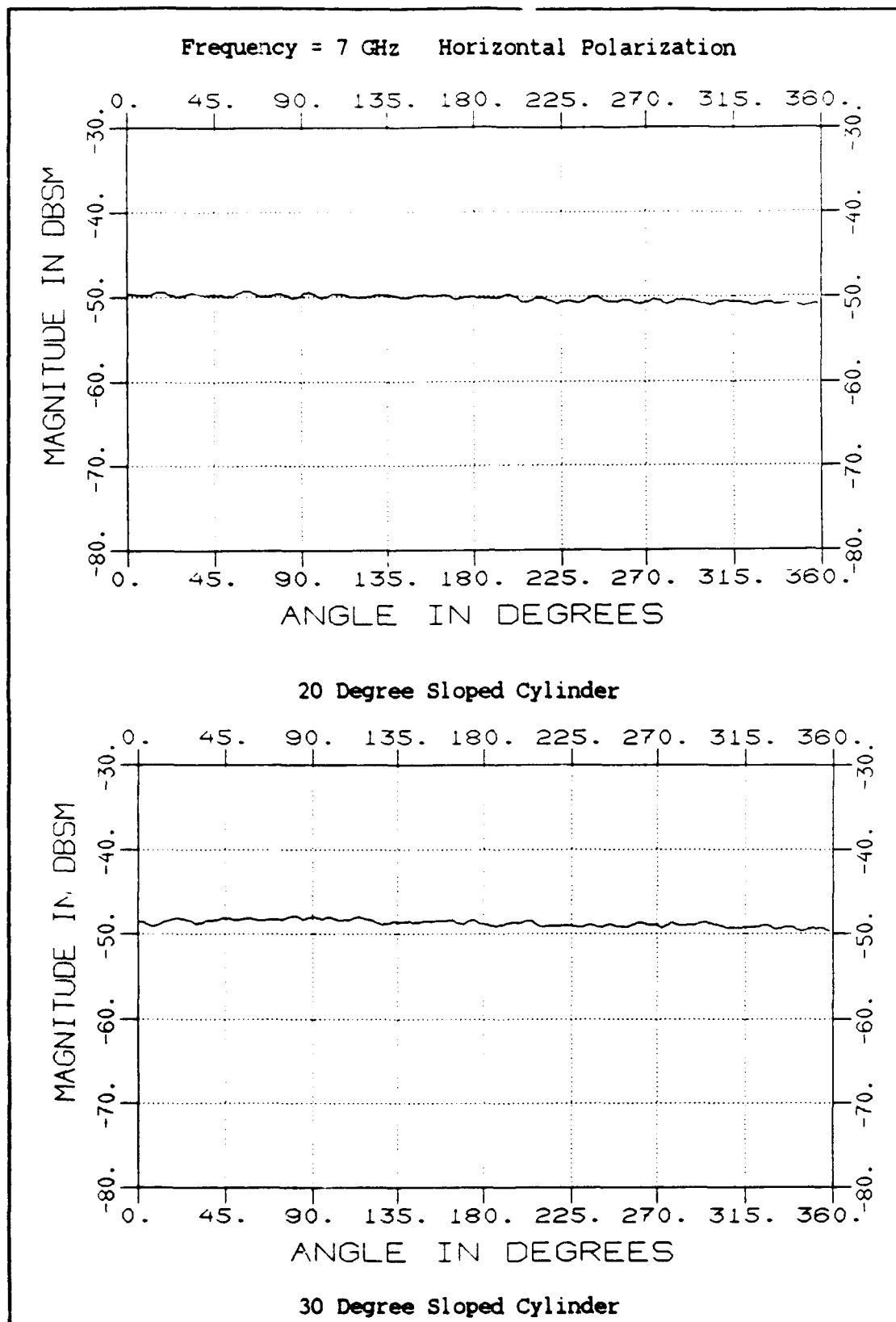


Figure C.3. Azimuth Scans of the 20° and 30° Sloped Cylinders

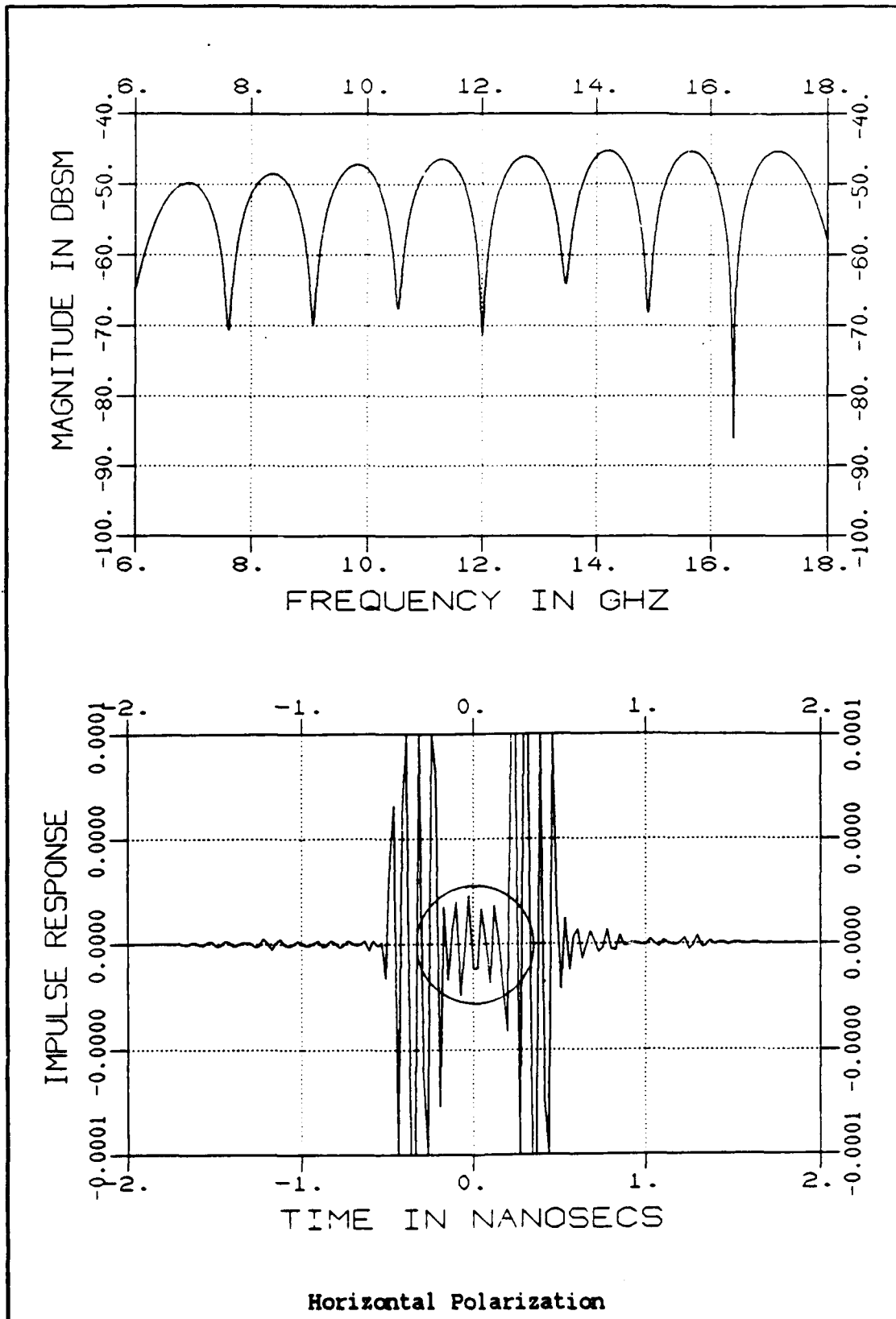


Figure C.4. Frequency/Time Domain Plot of the ROC

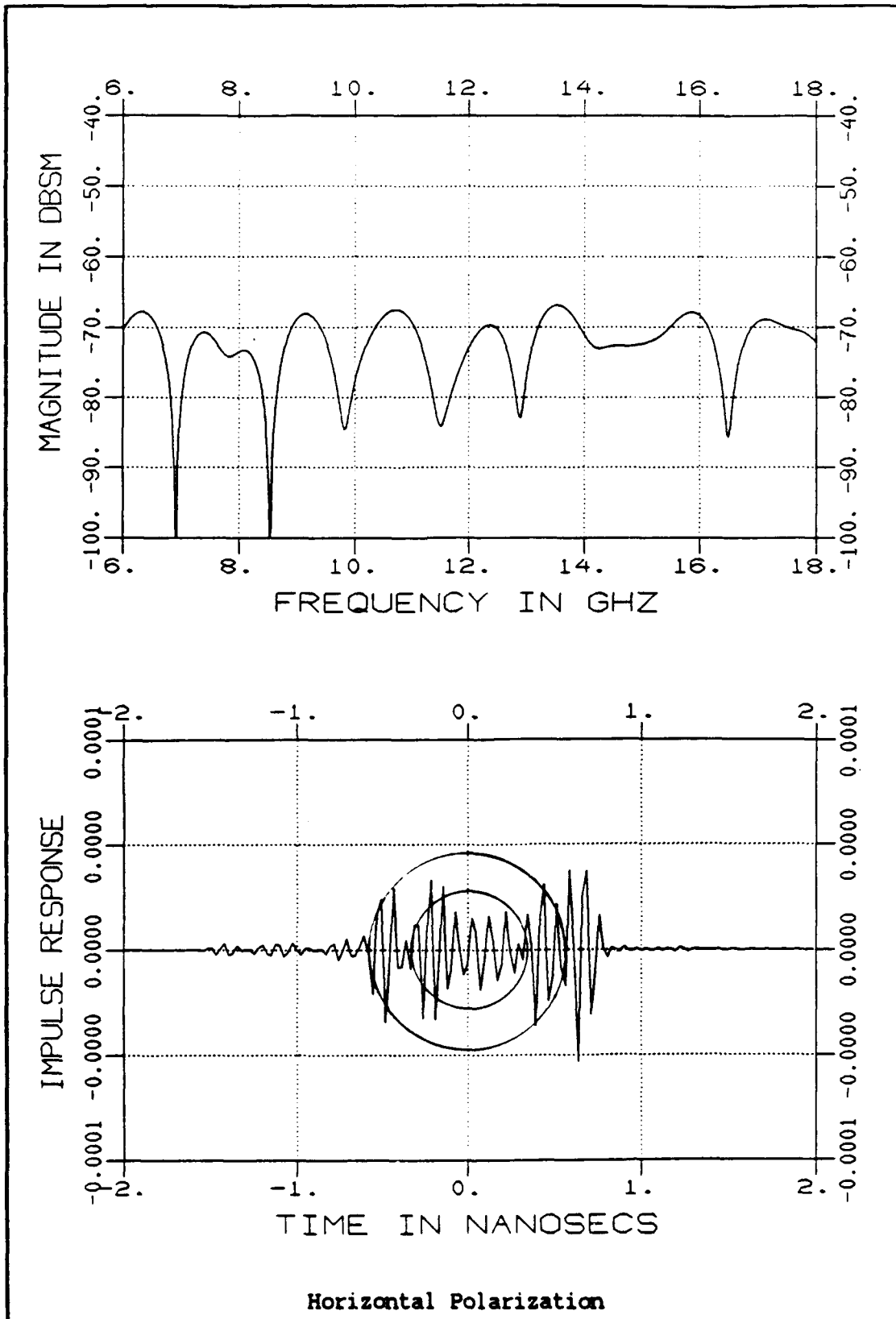


Figure C.5. Frequency/Time Domain Plot of the 10° Sloped Cylinder

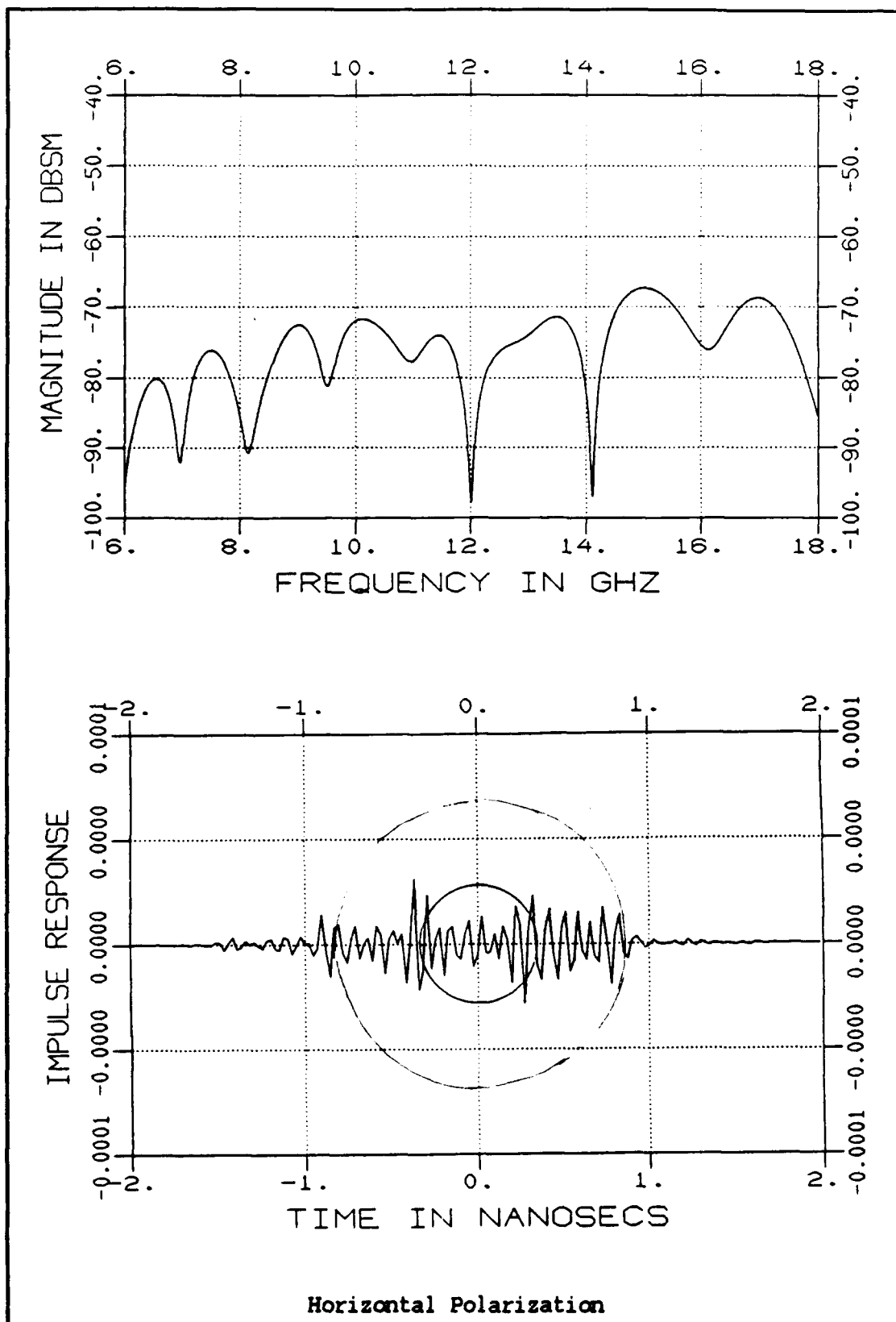


Figure C.6. Frequency/Time Domain Plot of the 20° Sloped Cylinder

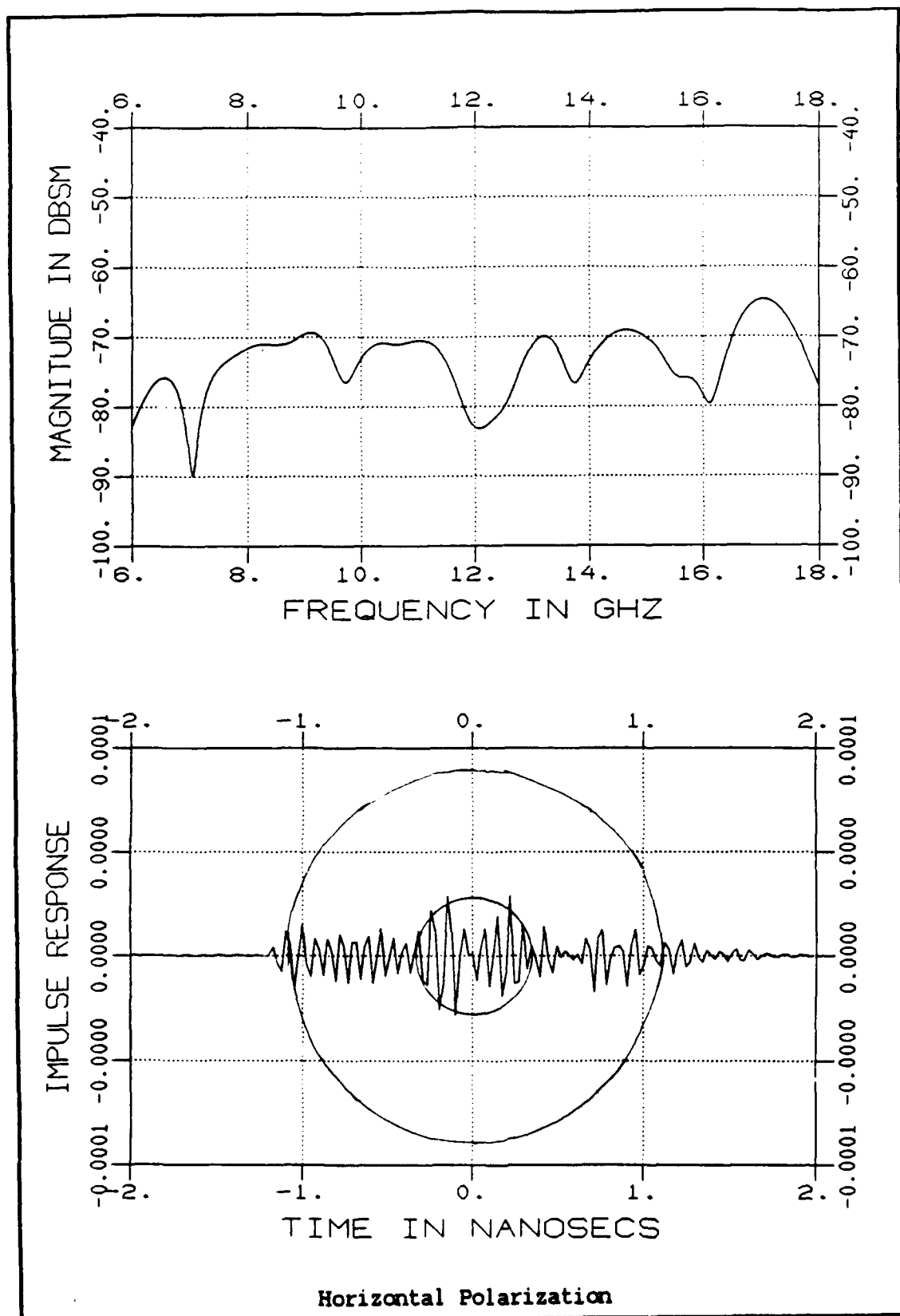


Figure C.7. Frequency/Time Domain Plot of the 30° Sloped Cylinder

APPENDIX D

RCS Measurements of the Shaped Columns

This appendix contains additional measurements for the Diamond, the Wedge-Ogive, and the Ogive. All were made at 10 GHz with vertical polarization. Each figure shows two measurements of the column.

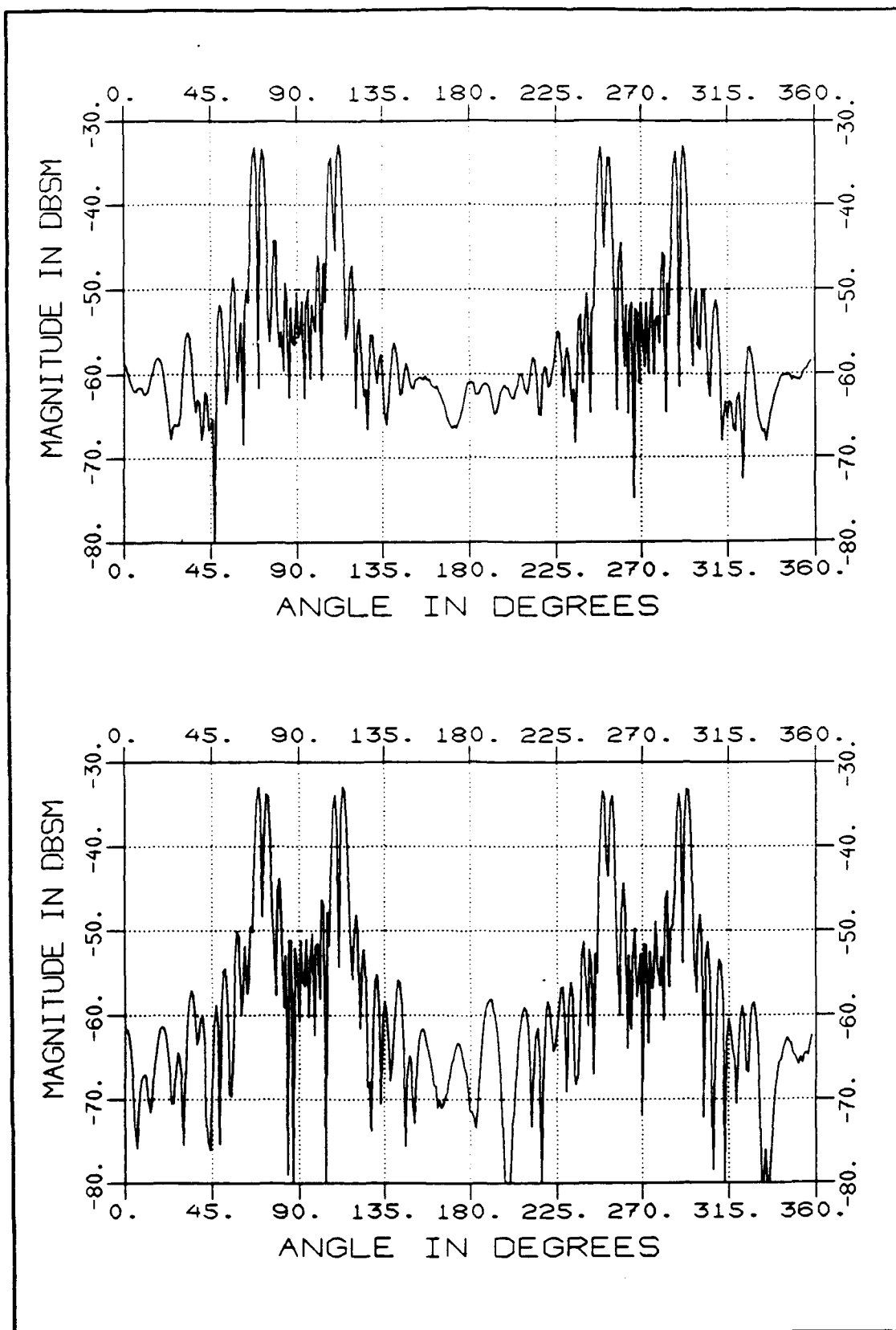


Figure D.1. Azimuth Scans of the Diamond

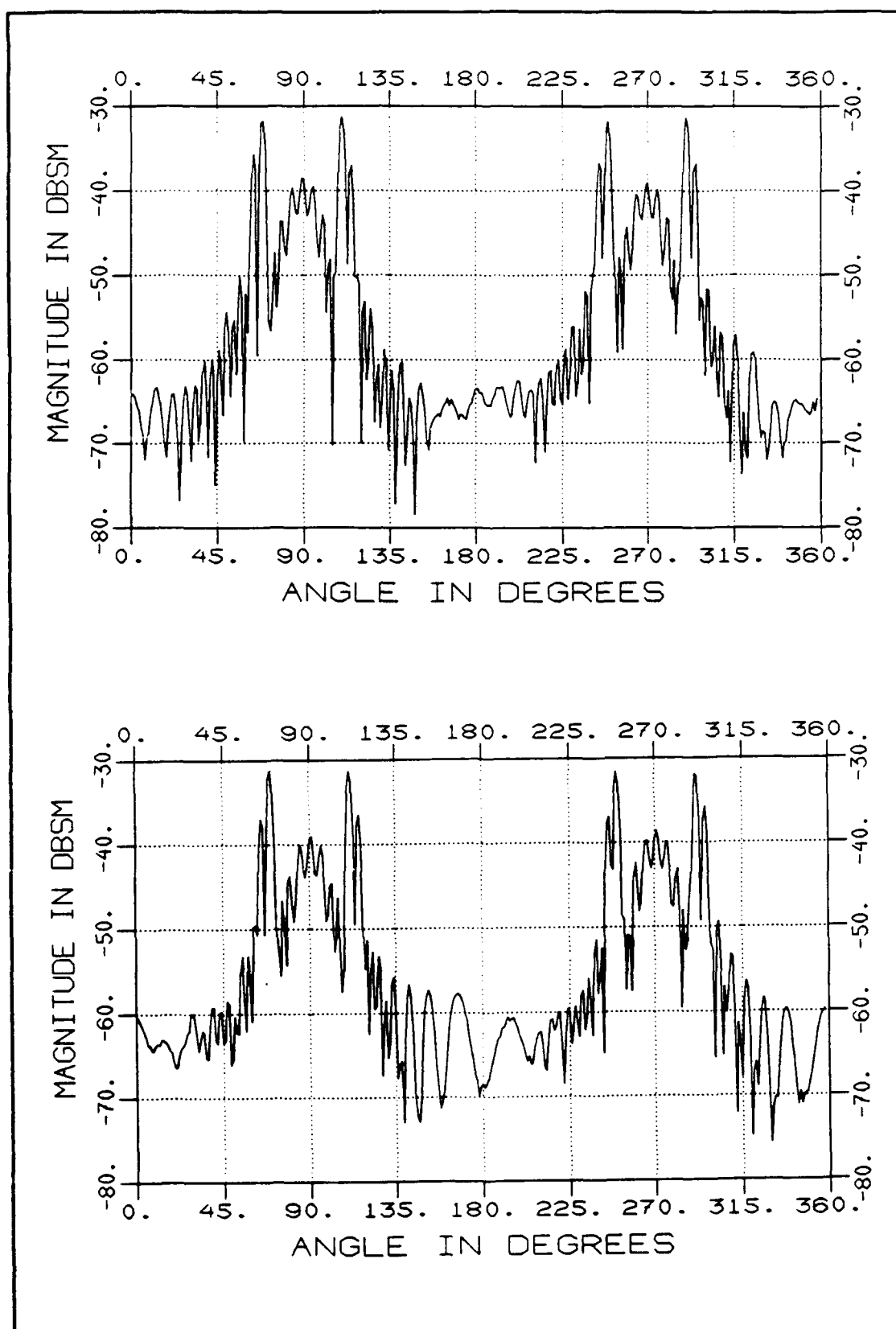


Figure D.2. Azimuth Scans of the Wedge-Ogive

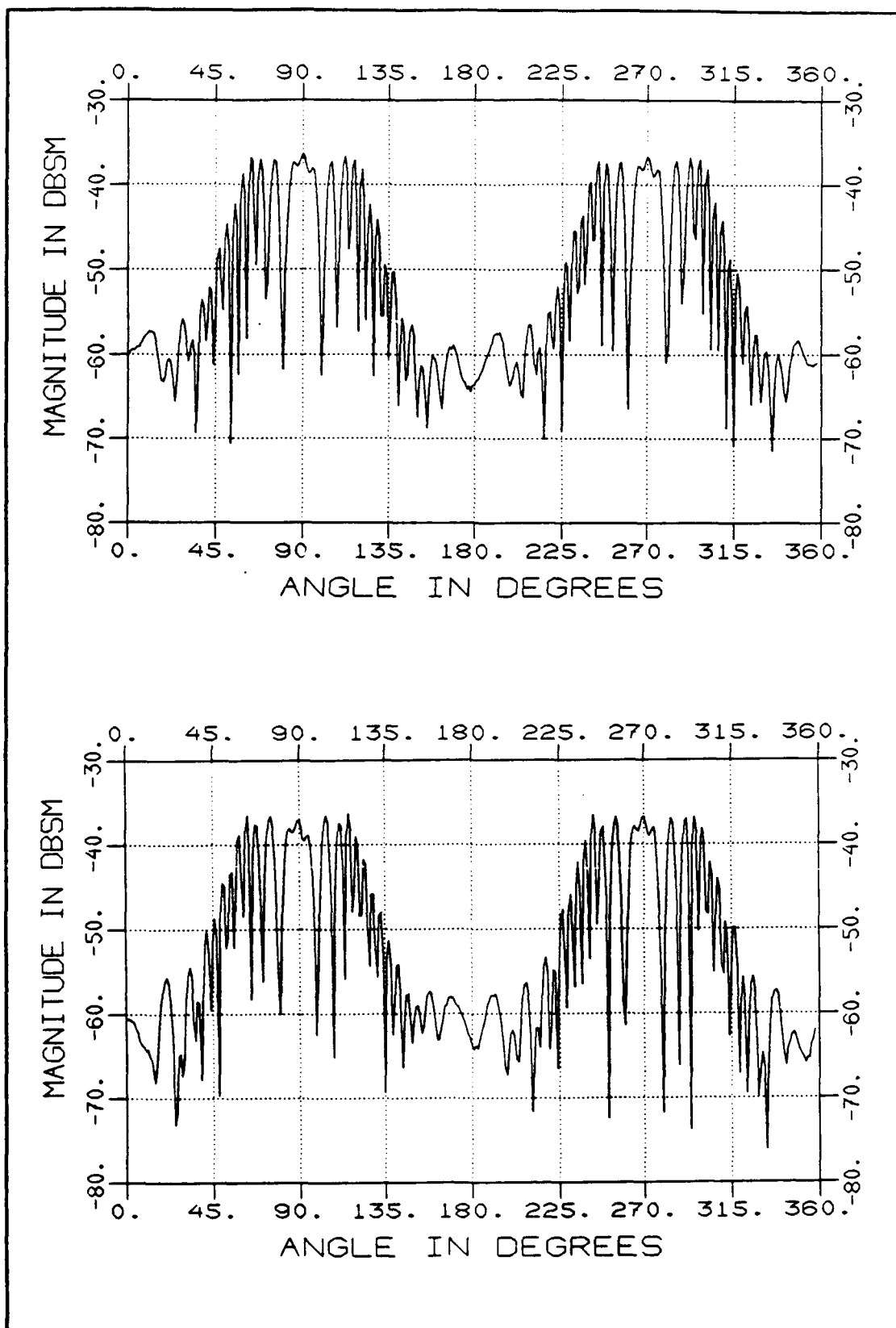


Figure D.3. Azimuth Scans of the Ogive

APPENDIX E

RCS Measurements of the Sloped Diamond

This appendix contains additional measurements made for the sloped Diamond column. In some figures, a comparison against the Diamond is shown. All measurements used vertical polarization.

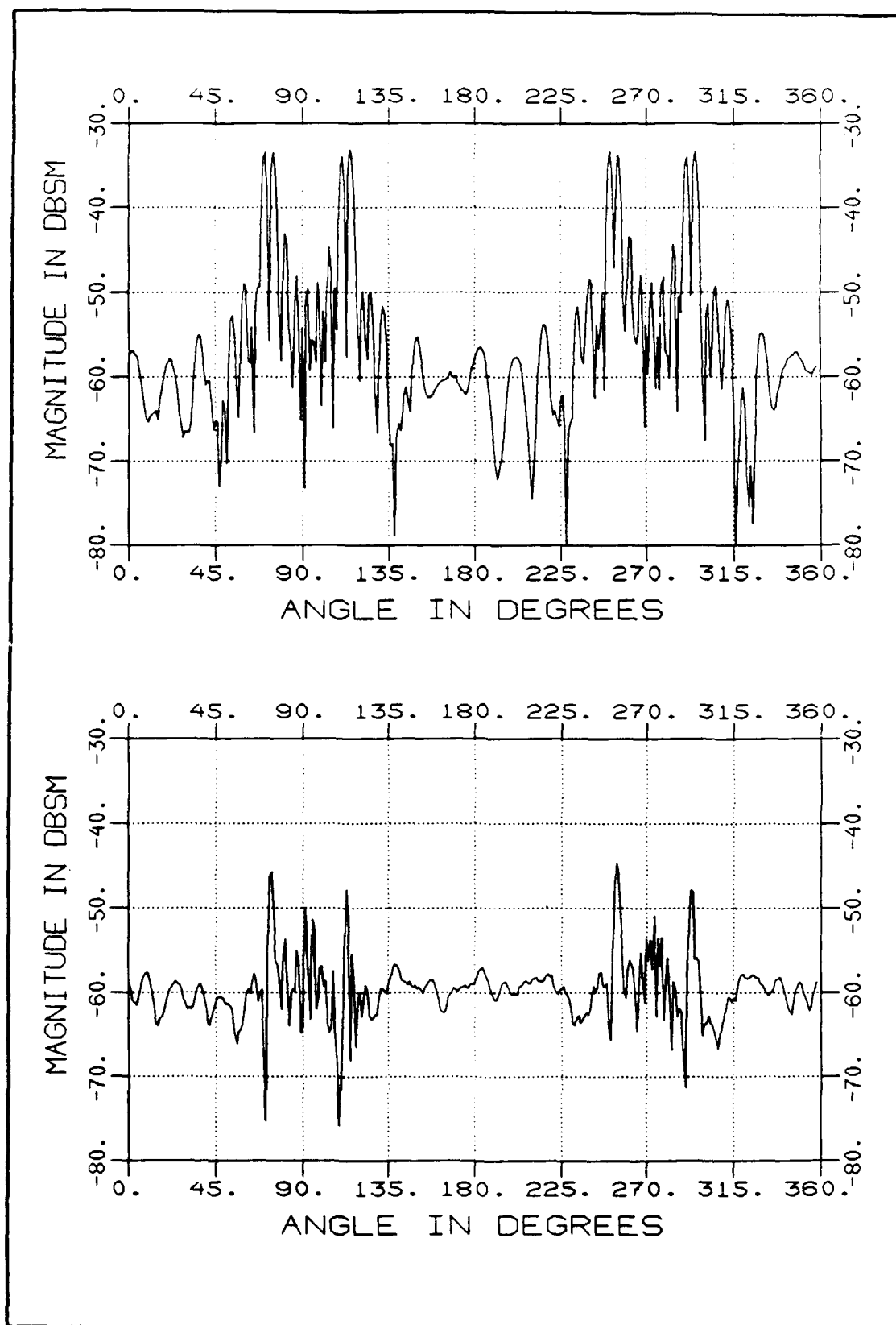


Figure E.1. Comparison of Diamond and Sloped Diamond at F=10 GHz

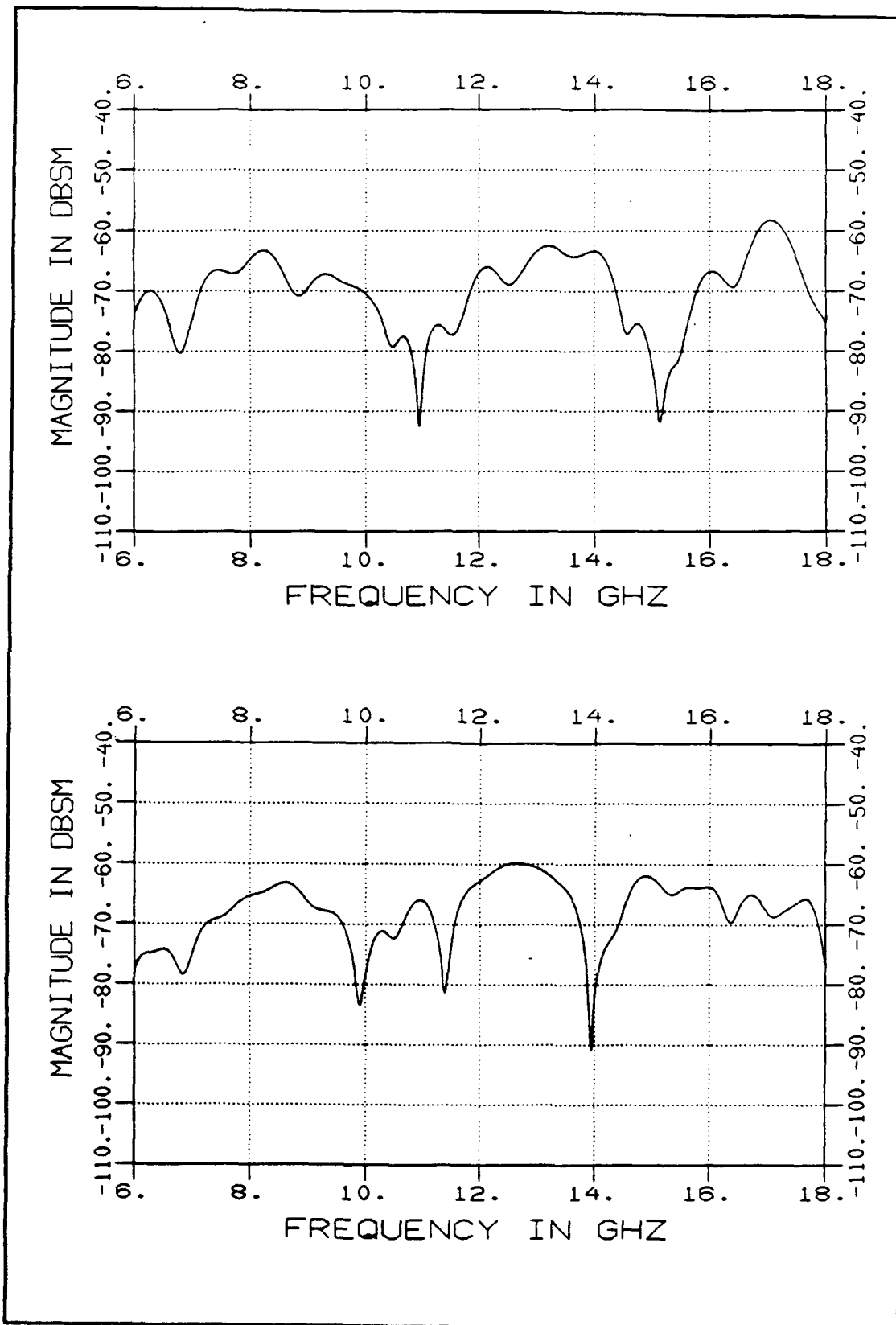


Figure E.2. Comparison of Tip-On Frequency Response

These plots show that the edge connecting the sloped sides causes most of the return. This suggests that some type of rounding may help to lower the RCS.

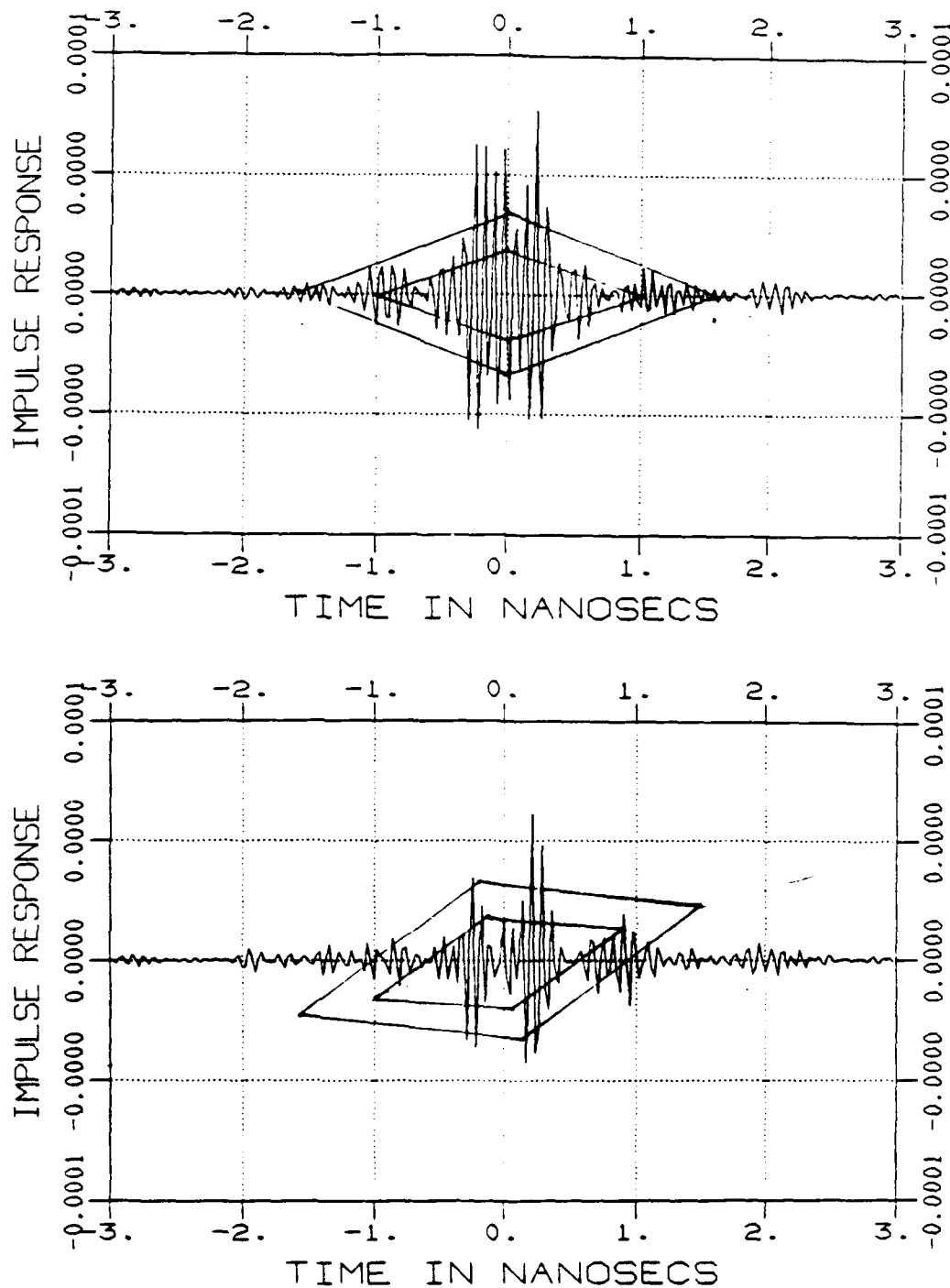


Figure E.3. Impulse Response of the Diamond at 0° and 15°

APPENDIX F

Impulse Response Plots of the Partial Cylinder

This appendix contains a series of measurements used to determine the dominant scattering mechanisms for the partial cylinder. Each plot represents a particular incident angle θ .

Figure F.1 shows the high return associated with the reflection from the flat face, and the rapid fall-off as θ changes slightly. Figure F.2 shows that as θ gets larger, the reflection from the curved face dominates. In Figure F.3, θ is approaching and reaching the angle ϕ , where the reflection ends. At $\theta = \phi = 60^\circ$ the forward corner diffraction is high enough to smooth the return. The return from this corner decrease with angle, as seen in Figure F.4. At $\theta=90^\circ$, the only mechanisms are from the two curved edge, and these are very weak.

At $\theta > 120^\circ$ the reflection from the concave surface begins. Figure F.5 shows the response before and after the reflection occurs. Figure F.6 displays the final plots. At $\theta=165^\circ$ the forward corner diffraction grows stronger, and at $\theta=180^\circ$, the flat plate again dominates.

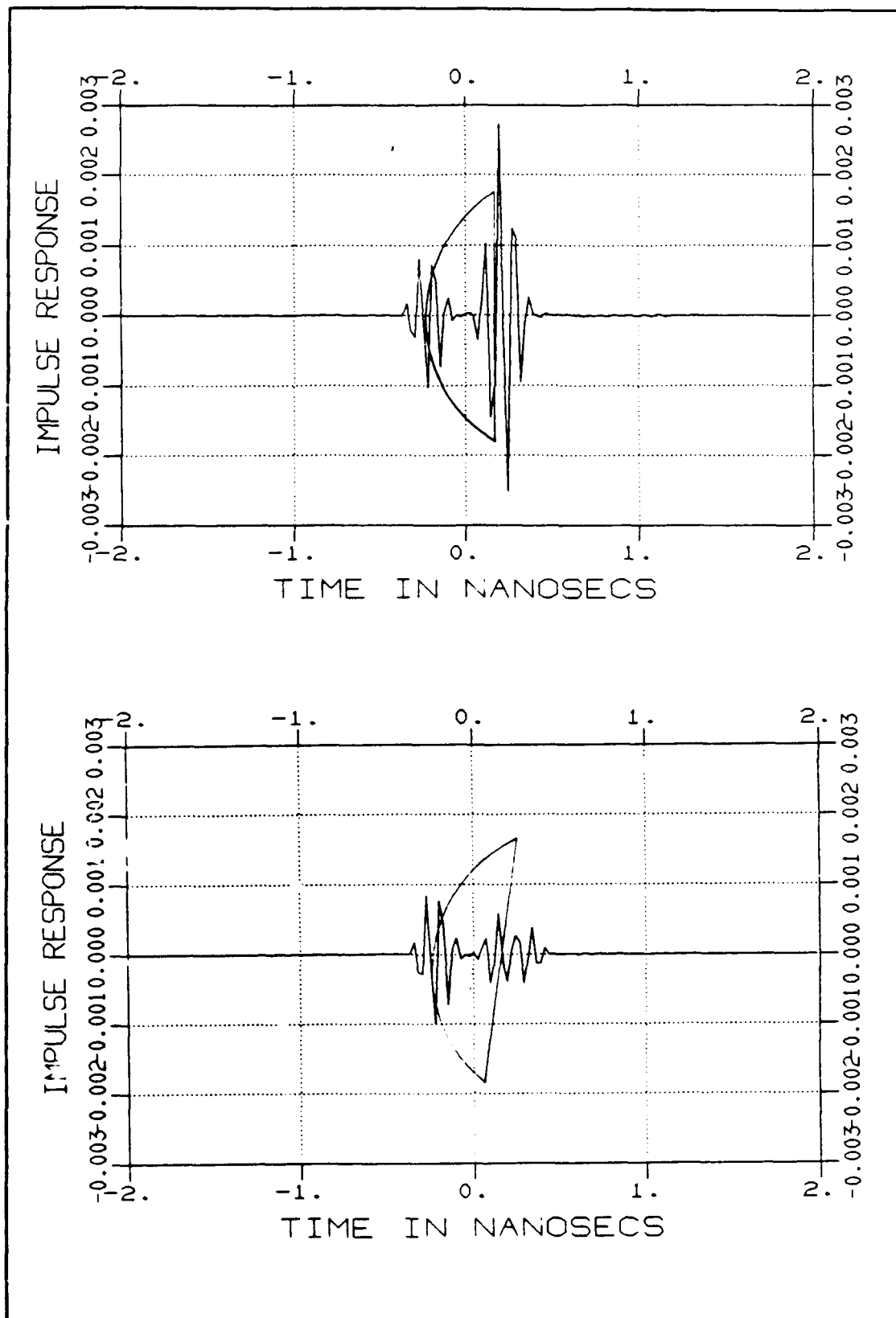


Figure F.1. Impulse Response at $\theta = 0^\circ$ and $\theta = 5^\circ$

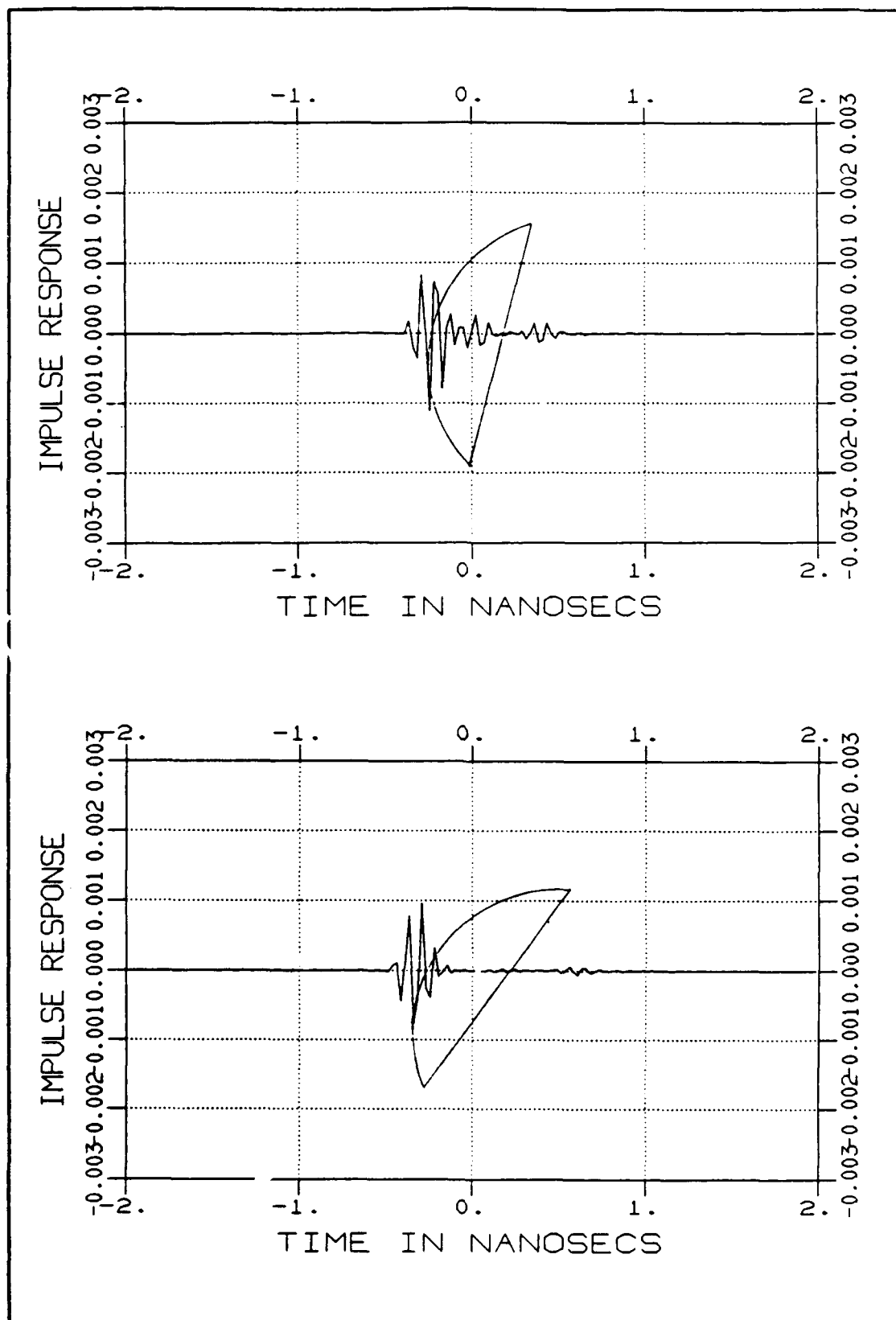


Figure F.2. Impulse Response at $\theta = 15^\circ$ and $\theta = 35^\circ$

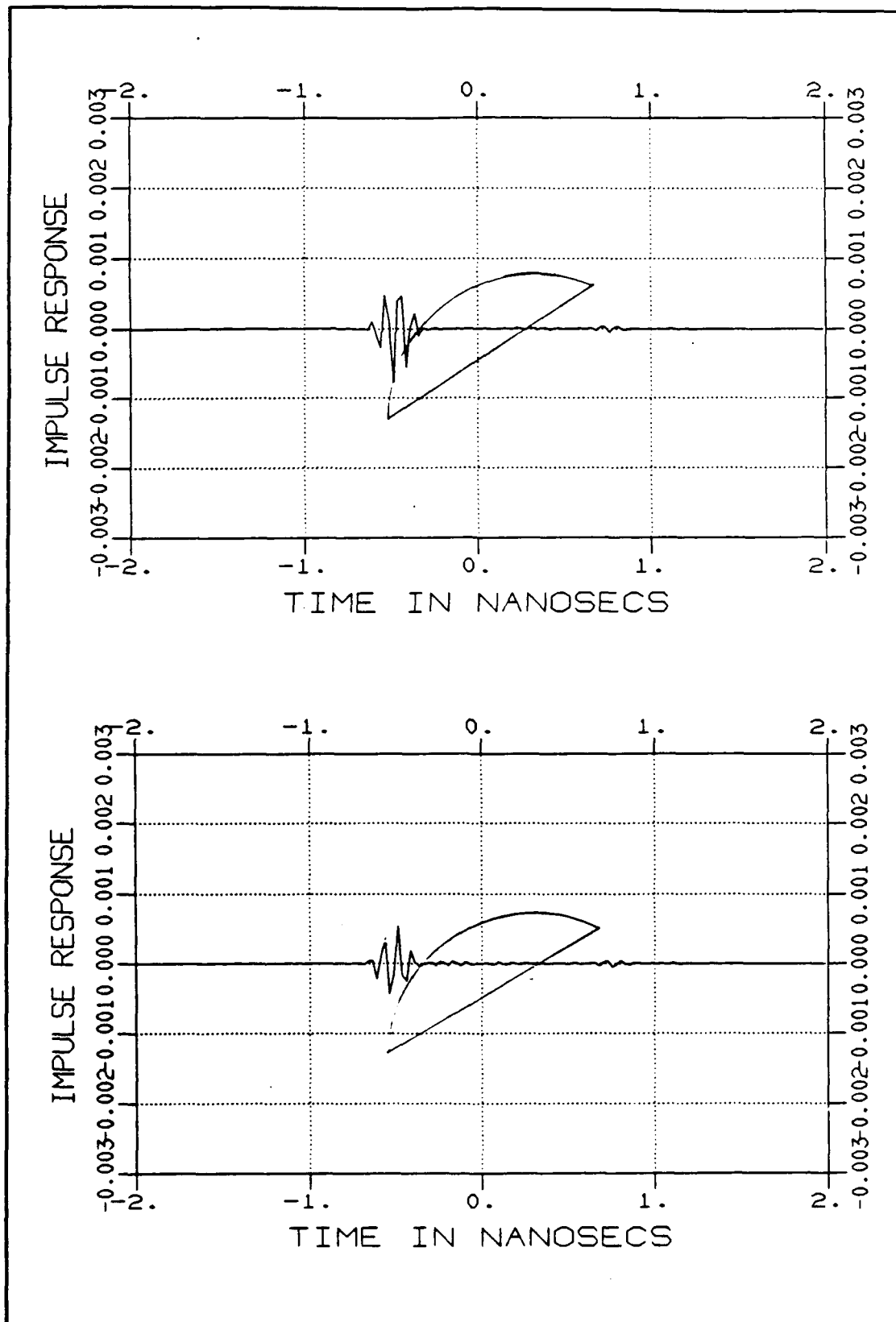


Figure F.3. Impulse Response at $\theta = 55^\circ$ and $\theta = 60^\circ$

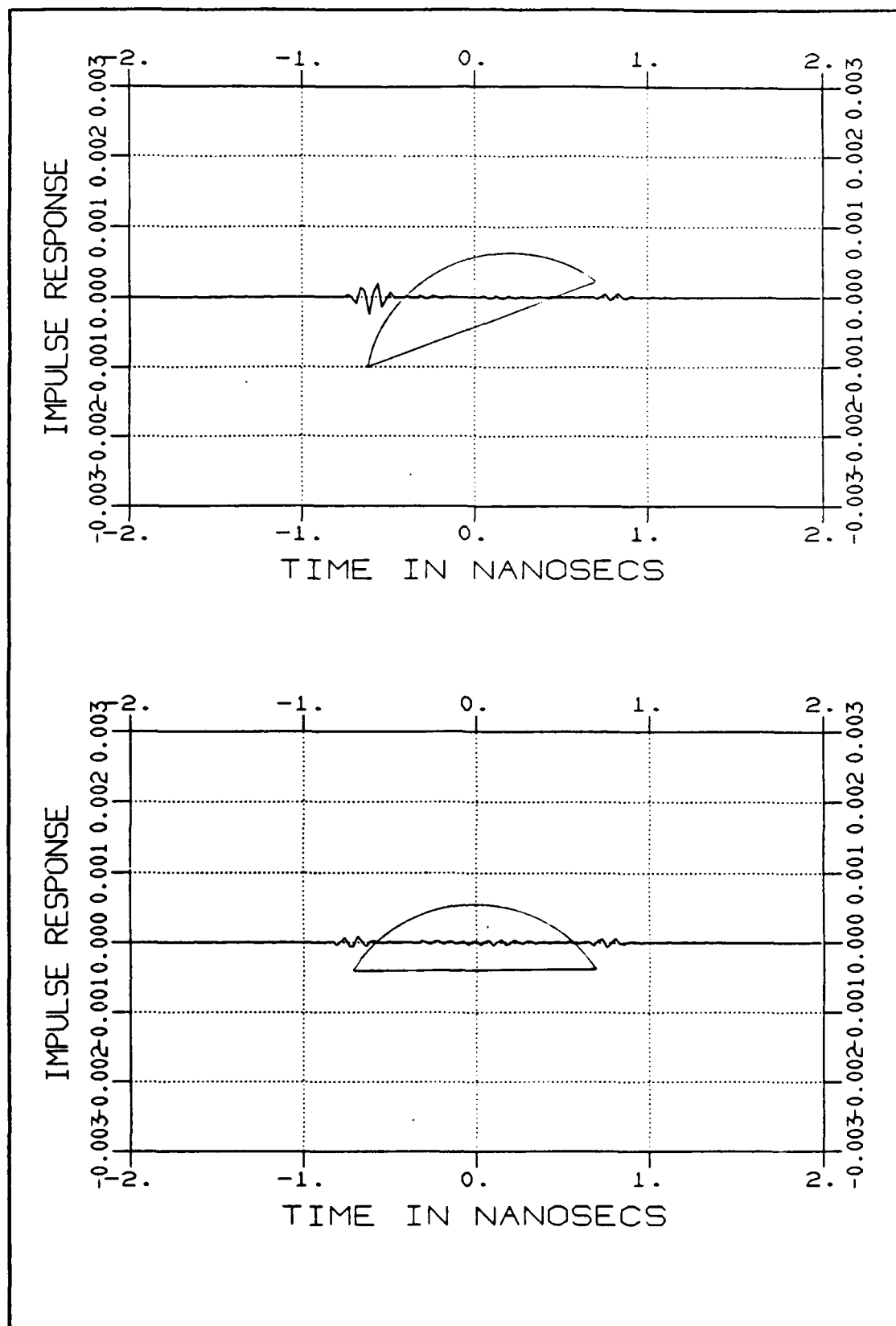


Figure F.4. Impulse Response at $\theta = 70^\circ$ and $\theta = 90^\circ$

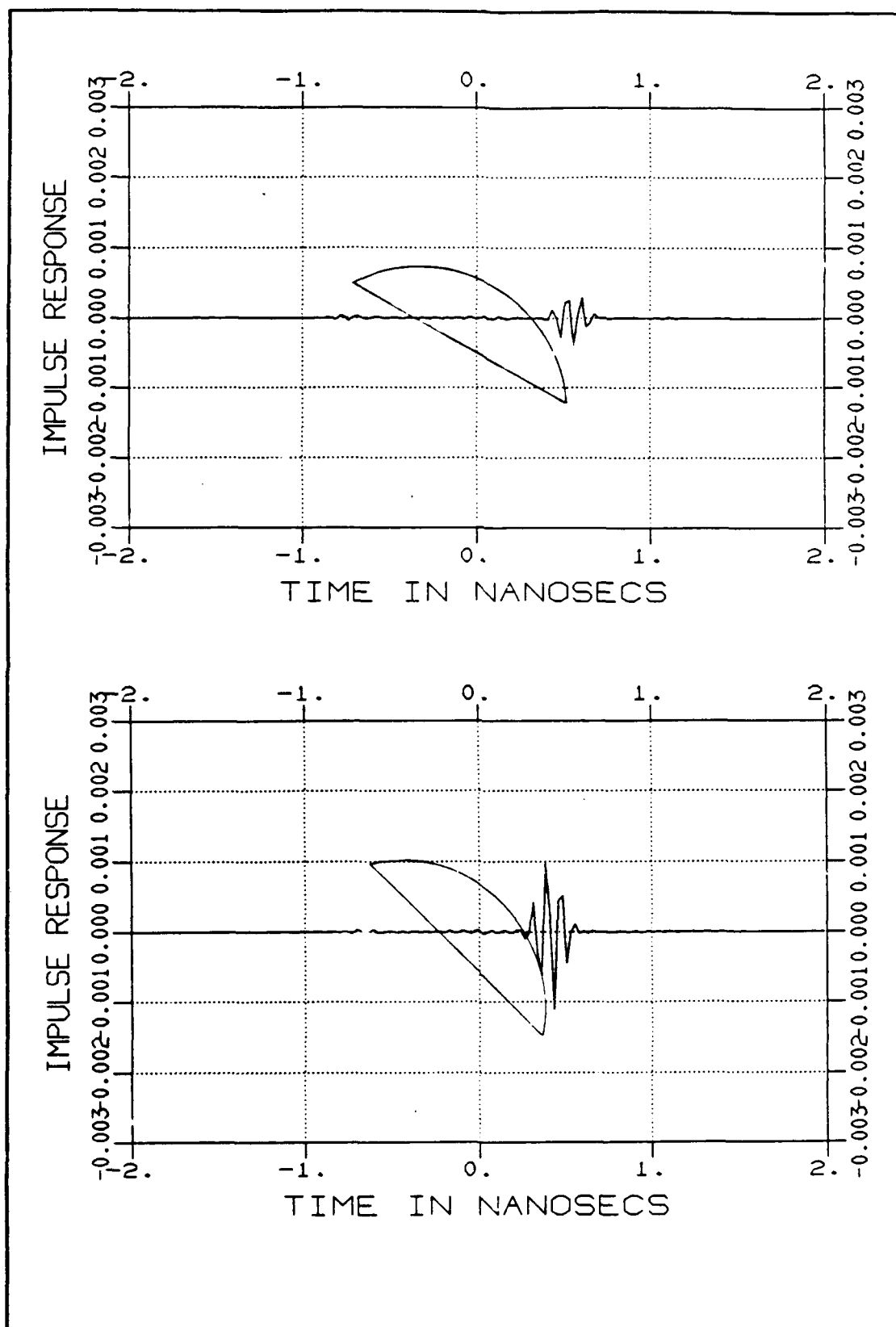


Figure F.5. Impulse Response at $\theta = 120^\circ$ and $\theta = 135^\circ$

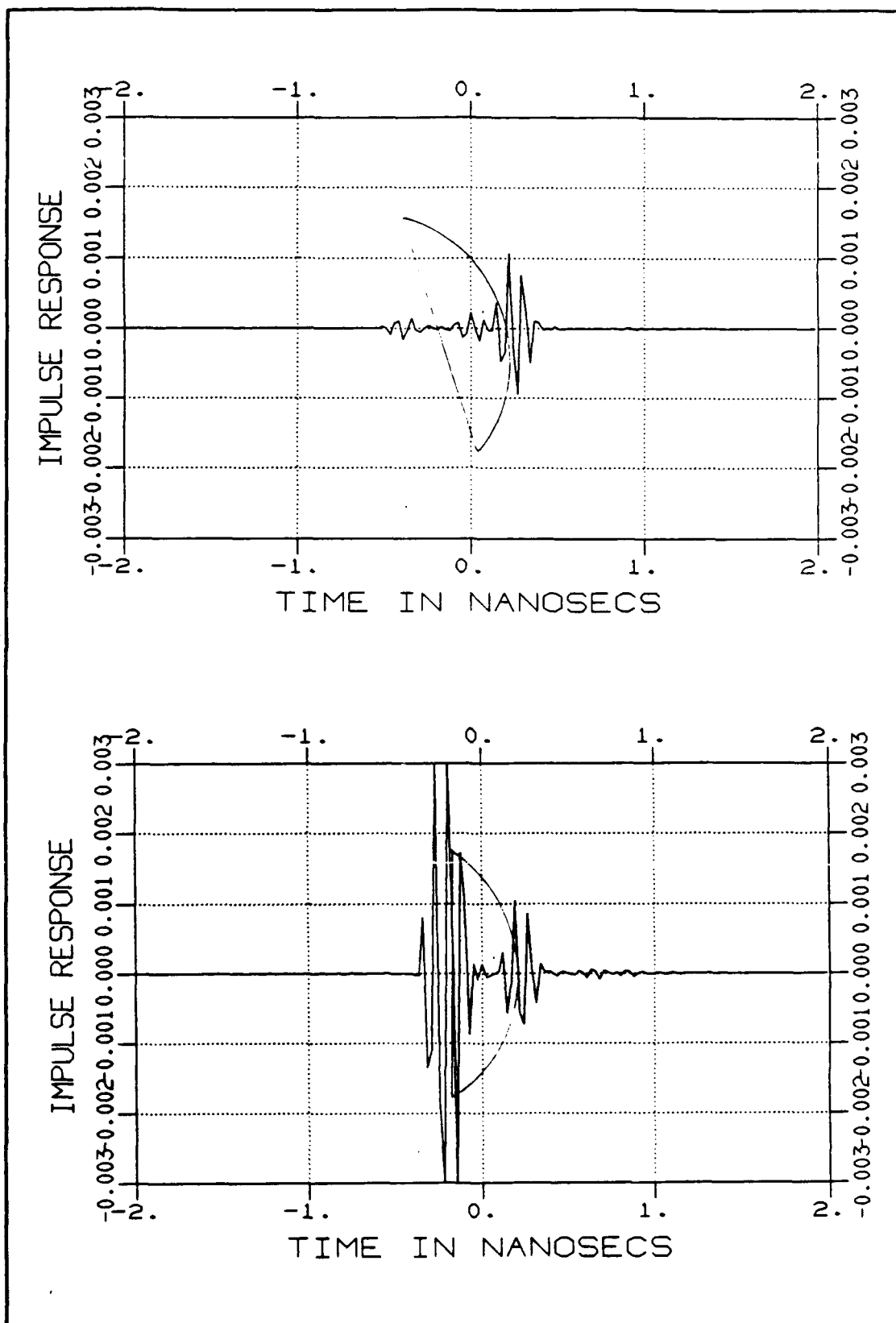


Figure F.6. Impulse Response at $\theta = 165^\circ$ and $\theta = 180^\circ$

Bibliography

1. Knott, Eugene F. and others. Radar Cross Section. Norwood, Ma: Artec House, Inc., 1985.
2. Plonus, M.A. Theoretical Investigations of Scattering From Plastic Foams. The University of Michigan, Department of Electrical Engineering, Radiation Laboratory. September 1963 (AD-437900).
3. Plonus, M.A. "Theoretical Investigations of Scattering From Plastic Foams," IEEE Transactions on Antennas and Propagation, 13: 88-93 (January 1965).
4. Kerr, Donald E. Propagation of Short Radio Waves. New York, NY: McGraw-Hill Book Company, Inc., 1951.
5. Senior, T.B.A. and others. Radar Cross Section of Target Supports - Plastic Materials. RADC Contract No. 64-381, June 1964 (AD-608252).
6. Senior, T.B.A. and others. "Designing Foamed-Plastic Target Supports," Microwaves, 3: 38-41 (December 1964).
7. Plonus, M.A. and others. "A Truncated Cone Model Support for Anechoic Chambers," IEEE Transactions on Antennas and Propagation, 16: 256-258 (March 1968).
8. Keller, J.B. "Geometrical Theory of Diffraction," Journal of the Optical Society of America, 52: 116-130 (February 1962).
9. Kouyoumjian, Robert G. and others. "A Uniform Geometrical Theory of Diffraction from an Edge in a Perfectly Conducting Surface," Proceedings of the IEEE, 62: 1448-1461 (November 1974).
10. Joseph, Philip J., Capt, USAF. A UTD Scattering Analysis of Pyramidal Absorber for Design of Compact Rang Chambers, PhD Dissertation. Ohio State University, Columbus OH, 1988.
11. Burnside, Walter D. and others. "High Frequency Scattering by a Thin Lossless Dielectric Slab," IEEE Transactions on Antennas and Propagation, 31: 104-110 (January 1983).
12. Weeks, W.L. Electromagnetic Theory for Engineering Applications. New York: John Wiley & Sons, Inc., 1964.
13. Balanis, C.A. Advanced Engineering Electromagnetics. New York: John Wiley & Sons, Inc., 1989.

Bibliography

14. Makekau, Charles K., Capt, USAF. Implementation and Analysis of an ISAR Imaging in the AFIT Anechoic Chamber. MS Thesis, AFIT/GE/ENG. School Engineering, Air Force Institute of Technology (AU), Wright-Patterson AFB OH, December 1991 (To be published).
15. Salisbury, Amy. RCS Engineer, Personal Communication. EG&G Corp., Holloman AFB, NM.

Vita

Captain Michael W. Chambers was born on 23 May 1960 in Rensselaer, Indiana. He graduated from Twin Lakes High School in Monticello, Indiana in 1978. After one year of college, at Purdue University, he enlisted in the U.S. Air Force as a Wideband Radio Maintenance Technician. In 1984, he accepted into the Airman Education and Commissioning Program, and began attending Purdue University. He graduated with a Bachelor of Science in Electrical Engineering in December of 1986. In April 1987, he completed Officer Training School and was assigned as a Second Lieutenant to Eglin AFB. He served as an Electronic Warfare engineer until entering the Air Force Institute of Technology in May 1990.